

4-7-2015

Control Strategies of Power Electronic Converters to Improve the Reliability and Stability of Renewable Energy Systems

Tai-Sik Hwang

University of Connecticut - Storrs, taisik.hwang@gmail.com

Follow this and additional works at: <https://opencommons.uconn.edu/dissertations>

Recommended Citation

Hwang, Tai-Sik, "Control Strategies of Power Electronic Converters to Improve the Reliability and Stability of Renewable Energy Systems" (2015). *Doctoral Dissertations*. 699.

<https://opencommons.uconn.edu/dissertations/699>

Control Strategies of Power Electronic Converters to Improve the Reliability and Stability of Renewable Energy Systems

Tai-Sik Hwang, Ph.D

University of Connecticut, 2015

This dissertation discusses control strategies for power electronic converters that improve the reliability and stability of renewable energy systems. Three approaches are proposed to improve the control performance of a dc-dc converter and a distributed generation (DG) inverter under different operation modes and fault conditions.

First, a seamless control for the dc-dc converter with both discontinuous conduction mode (DCM) and continuous conduction mode (CCM) is proposed. The plant models in DCM and CCM are different in the frequency domain. Therefore, it is difficult to design a controller with stable operation and fast response in both modes. The proposed controller can make mode transitions between DCM and CCM seamlessly with a mode tracker, and then the boost converter can autonomously operate by selecting the appropriate control loop in both modes.

Second, a seamless control for the DG inverter with both a grid connected (GC) mode and a standalone (SA) mode is presented. With increasing renewable DGs, fast and stable mode transition technologies are necessary not only for sending the power to the grid in the GC mode, but also for protecting DGs from grid fault conditions in the SA mode. The proposed controller consists of a current controller and a feedforward voltage controller to minimize the grid overvoltage and improve the voltage response.

Tai-Sik Hwang – University of Connecticut, 2015

Third, a control strategy to suppress a dc power oscillation of the DG inverter under grid voltage unbalance is discussed. Due to voltage unbalance, the dc power oscillation is generated, which impacts the lifespan of the renewable energy sources. A modified synchronous reference frame based current control with improved current reference is proposed. With the proposed current loop, the dc power oscillation is reduced effectively.

The proposed control strategies reduce the impact of the renewable energy and the load under faults or disturbance conditions. And the stable operation of the power electronic converters will also enhance the stability and reliability of the renewable energy, the grid, and the load.

Control Strategies of Power Electronic Converters to Improve the Reliability and
Stability of Renewable Energy Systems

Tai-Sik Hwang

B.S., Yeungnam University, 2004

M.S., Yeungnam University, 2006

A Dissertation

Submitted in Partial Fulfillment of the
Requirements for the Degree of Doctor of Philosophy
at the University of Connecticut

2015

Copyright by

Tai-Sik Hwang

2015

APPROVAL PAGE

Doctor of Philosophy Dissertation

**Control Strategies of Power Electronic Converters to Improve the Reliability and Stability
of Renewable Energy Systems**

Presented by

Tai-Sik Hwang, B.S., M.S.

Major Advisor _____
Sung-Yeul Park

Associate Advisor _____
Krishna R. Pattipati

Associate Advisor _____
Ali M. Bazzi

Associate Advisor _____
Shalabh Gupta

University of Connecticut

2015

ACKNOWLEDGMENTS

I would never have been able to finish my dissertation without the guidance of my committee members. I would like to thank my advisor, Prof. Sung-Yeul Park for his patience, and supporting for my research. I would like to thank Prof. Krishna R. Pattipati, who helps and supports my job applications. I would like to thank my committee members, Prof. Ali M. Bazzi and Prof. Shalabh Gupta for their encouragement, insightful comments, and hard questions.

I would like to thank Sungmin Park, Ph.d and Yongduk Lee, Ph.d Candidate, who as my good lab members were always willing to help and give their best suggestions. I thank to Matthew Tarca and other members in the laboratory. My research would not have been possible without their helps.

I would also like to thank my mother, and two sisters. They were always supporting me and encouraging me with their best wishes.

TABLE OF CONTENTS

CHAPTER 1. INTRODUCTION	1
1.1 Overview	1
1.2 Problem Statement	2
1.2.1 Control of dc-dc converter with mode transition	2
1.2.2 Control of DG inverter with mode transition	3
1.2.3 Control of DG inverter under grid distortion	4
1.3 Dissertation Organization	5
CHAPTER 2. LITERATURE REVIEW	6
2.1 Control of dc-dc converter with mode transition	6
2.2.1 Dc-dc converter for fuel cell applications	6
2.1.2 Control of dc-dc converter with mode transition	8
2.2 Control of DG Inverter with mode transition	10
2.2.1 Current control in the GC mode	10
2.2.2 Voltage control in the SA mode	11
2.2.3 Mode transition approach	11
2.3 Control of DG inverter under grid voltage unbalance	14
CHAPTER 3. SEAMLESS CONTROL OF DC-DC CONVERTERS BETWEEN DCM AND CCM	17
3.1 Boost Converter Modeling In DCM and CCM	17
3.1.1 Small signal modeling in CCM and DCM	17
3.1.2 Mode Boundary [113]	19
3.1.3 Issues with Designing the Controller for both CCM and DCM	20
3.2 Proposed Controller Design in DCM and CCM	22
3.2.1 Current Control in CCM [114]	22
3.2. 2 Feedforward Current Control in DCM	23
3.2. 3 Voltage Control in both CCM and DCM	24
3.2. 4 Proposed Seamless Control System with Mode Tracker	26
3.2.5 Stability and Robustness of Seamless Mode Transition	27
3.2.6 Transient Response during the mode transition	31
3.3 Simulation Results	31
3.4 Experimental Results	34
3.5 Conclusion	37

CHAPTER 4. SEAMLESS CONTROL OF DG INVETERS FOR MODE TRANSITIONS UNDER GRID DISTURBANCE.....	39
4.1 Impact of DG Inverter in Overvoltage Conditions	39
4.1.1 Mode transitions of DG inverter in Overvoltage Conditions.....	39
4.1.2 Mode transition in the overvoltage due to PCC switch-off.....	40
4.1.3 Mode transition in the overvoltage due to grid voltage swell	41
4.1. 4 Requirements for Fast Mode transition of DG inverter in overvoltage conditions.....	42
4.2 Conventional DG Inverter Control with Operational Modes.....	43
4.2.1 DG inverter Modeling in GC mode and SA mode (Appendix A)	43
4.2.2 Current Control in GC mode.....	46
4.2.3 Voltage control in SA mode.....	48
4.2.4 Performance and Limitation of Voltage Control in the overvoltage conditions	48
4.3 Seamless Control Strategy in Overvoltage Conditions	52
4.3.1 Proposed controller configuration.....	52
4.3.2 Current Reference Calculation with respect to Operational Modes.....	53
4.3.3 Current Control with Feed forward Voltage loop.....	54
4.4 Simulation Results	57
4.5 Experimental Results	62
4.5.1 Hardware- In- the Loop Test using RTDS.....	62
4.5.2 Experimental Wave forms	63
4.6 Conclusion	66
CHAPTER 5. CONTROL OF LCL FILTER BASED DG INVERTERS TO SUPPRESS DC POWER OSCILLATION UNDER GRID VOLTAGE UNBALANCE	67
5.1 Control overview of LCL filter based DG inverter under grid voltage unbalance	67
5.2 Impact of DG Inverter under Grid Voltage Unbalance.....	69
5.1.1 DG inverter modeling under unbalanced grid voltage	69
5.1.2 Dc power oscillation due to oscillating ac power under grid voltage unbalance	71
5.2 Performance of Conventional Control Scheme.....	74
5.2.1 Conventional current reference calculations [98]	74
5.2.3 Conventional double synchronous reference frame current control [98].....	76
5.3 Proposed Control Scheme for Suppression of DC Power Oscillation	80
5.3.1 Improved current reference calculation	80
5.3.2 State Vector under Unbalance Operating Conditions	81
5.3.2 Modified transformation on the unbalanced rotation frame.....	85

5.3.3 Dynamic voltage equation on the unbalanced rotating frame.....	87
5.3.4 Unbalanced grid voltage compensation on the unbalanced rotating frame.....	90
5.3.5 Proposed control scheme	92
5.4 Simulation Results	93
5.5 Experimental Results	95
5.6 Conclusion	97
CHAPTER 6. SUMMARY AND FUTURE WORKS	98
APPENDIX A. MODELING OF THEREE PHASE <i>LCL</i> FILTER BASED DC-AC INVERTER.....	101
A.1 Dc-ac inverter modeling in the <i>abc</i> axis	101
A.2 α - β / <i>d-q</i> dc-ac inverter modeling using a vector notation	101
A.3 α - β / <i>d-q</i> dc-ac inverter modeling using a complex space vector notation.....	103
APPENDIX B. GENERAL COMPLEX SPACE VECTOR	106
APPENDIX C. SYMMETRICAL COORDINATE ANALYSIS	107
APPENDIX D. ROTATION OF AXES	109
REFERENCES	111

LIST OF TABLES

TABLE I. Ratings and Known Parameters of Boost Converter and Control System.....	32
TABLE II. Parameters with respect to power consumption of the critical load.....	46
TABLE III. Comparison of Controllers Performance for Mode Transition.....	61

LIST OF FIGURES

Fig. 1. The role of the power electronic converters in renewable energy systems.....	1
Fig. 2. Control scheme of the dc-dc converter.....	3
Fig. 3. Control scheme of the DG inverter with respect to operational modes.....	4
Fig. 4. Control scheme of the DG inverter under grid voltage unbalance and harmonics.	4
Fig. 5. V-I characteristics of the DBFC.....	6
Fig. 6. Block diagram of adaptive tuning algorithm for dc-dc converter.....	8
Fig. 7. Mixed-mode operation of boost switch-mode rectifier.....	9
Fig. 8. MCFC power plant.....	12
Fig. 9. DG inverter system configuration with mode transition.....	13
Fig. 10. Indirect current control for seamless transfer of three-phase utility interactive inverters.....	14
Fig. 11. Dual current control scheme in synchronous reference frame for PWM converter under unbalanced input voltage conditions.....	15
Fig. 12. New stationary frame control scheme for three-phase PWM rectifiers under unbalanced voltage dips conditions.....	15
Fig. 13. Boost converter configuration.....	18
Fig. 14. Frequency responses of the duty ratio-to-output voltage transfer function in CCM and DCM.....	21
Fig. 15. Loop gains of compensator according to DCM and CCM.....	21
Fig. 16. Block diagram of proposed current control with nonlinear feedforward in CCM.....	23
Fig. 17. Block diagram of feedforward current control in DCM.....	23
Fig. 18. Block diagram of voltage control in CCM.....	24
Fig. 19. Block diagram of voltage control in DCM.....	25
Fig. 20. Proposed control block diagram with a mode tracker.....	27
Fig. 21. Mixed control block diagram with respect to the operation mode and k_m	28
Fig. 22. Bode plot of $T_1(s)$ ($0.4 \leq k_m \leq 0.6$).....	30

Fig. 23. Bode plot of $T_2(s)$ ($0.4 \leq k_m \leq 0.6$).....	30
Fig. 24. Simplified control block diagram.....	31
Fig. 25. Simulation waveform of transient response ($10\Omega \rightarrow 25\Omega \rightarrow 10\Omega$).....	33
Fig. 26. Simulation waveform of transient response ($10\Omega \rightarrow 100\Omega \rightarrow 10\Omega$)	33
Fig. 27. Simulation waveform of transient response ($50\Omega \rightarrow 25\Omega \rightarrow 16.7\Omega \rightarrow 12.5\Omega$)	33
Fig. 28. DBFC and boost converter system.....	34
Fig. 29. Test waveform of transient response in proposed mixed controller (Input voltage: 6.0V, Load : 25 $\Omega \leftrightarrow 10\Omega$).....	35
Fig. 30. Test waveform of transient response (Input voltage: 4.5V, Load: $40\Omega \rightarrow 10\Omega$).....	36
Fig. 31. Test waveform of transient response (Input voltage: 4.5V, Load: $10\Omega \rightarrow 120\Omega$).....	37
Fig. 32. Occurrence of the critical load faults during conventional mode transition in the overvoltage.....	40
Fig. 33. Overvoltage due to PCC switch-off.....	41
Fig. 34. Overvoltage due to main grid voltage.....	42
Fig. 35. Control state during fast mode transition.....	43
Fig. 36. Circuit diagram of the DG inverter with the grid and the critical load.....	44
Fig. 37. Transfer function block diagram of the DG inverter.....	46
Fig. 38. Transfer function block diagram of DG inverter in GC mode.....	47
Fig. 39. Transfer function block diagram of DG inverter in SA mode.....	47
Fig. 40. Current control block diagram in GC mode.....	48
Fig. 41. Voltage control block diagram in SA mode.....	48
Fig. 42. Simplified voltage control loop with current loop in SA mode.....	49
Fig. 43. Responses of the voltage control with current loop according to the critical load type.....	50
Fig. 44. Simplified voltage control loop without the current control loop in SA mode.....	51
Fig. 45. Responses of the voltage control without current loop according to the critical load type.....	52
Fig. 46. Proposed overall control block diagram.....	52
Fig. 47. State flow diagram for operational mode decision in overvoltage conditions.....	54

Fig. 48. Block diagram of the simplified current control with feed forward voltage loop in SA mode.....	55
Fig. 49. Responses of the current control with feedforward voltage loop according to the critical load type.....	56
Fig. 50. Simulation results of the conventional mode transition from the current control to the voltage control with the current loop. PCC switch-off period with.....	57
Fig. 51. Simulation results of the conventional mode transition from the current control to the voltage control without the current loop.....	59
Fig. 52. Simulation results of the proposed mode transition in current control with feedforward voltage loop.....	60
Fig. 53. Experimental setup of hardware in the loop using RTDS.....	62
Fig. 54. Experimental waveform of current control in GC mode during PCC switch-off period with 3.3kW resistive load.....	63
Fig. 55. Experimental waveforms of conventional mode transition using the voltage control without current loop.....	64
Fig. 56. Experimental waveforms of the proposed mode transition using the current control with feedforward voltage loop.....	65
Fig. 57. Experimental waveforms of the proposed mode transition using the current control with feedforward voltage loop.....	65
Fig. 58. Control overview to suppress dc power oscillation under grid voltage unbalance.....	68
Fig. 59. Power flow of the LCL filter based DG inverter under unbalanced grid voltage.....	69
Fig. 60. Block diagram of the dc power ripple generation under unbalanced grid voltage.....	73
Fig. 61. Simulation waveforms of dc voltage and current oscillation suppression using conventional current reference.....	75
Fig. 62. Block diagram of conventional double d-q frame current control.....	76
Fig. 63. Simplified double d-q frame current control loop.....	79

Fig. 64. Step responses of conventional d-q frame current controllers of L and LC filters based inverter.....	79
Fig. 65. Positive- and negative-sequence synchronous reference frames.....	82
Fig. 66. Loci of positive- and negative-sequence state vectors and unbalanced state vector in the α - β axis.....	83
Fig. 67. Rotation of axes between general ellipse and standard ellipse.....	84
Fig. 68. Scaling between canonical ellipse and circle.....	84
Fig. 69. Comparison between the δ - γ transformation and the d-q transformation under unbalanced operating conditions.....	87
Fig. 70. Loci of unbalanced current and voltage vectors in the α - β axis.....	90
Fig. 71. Block diagram of current control loop in the δ - γ axis.....	90
Fig. 72. Bode plot of LCL filter with active damping.....	91
Fig. 73. Proposed control block diagram for dc power oscillation suppression.....	92
Fig. 74. Simulation waveforms of d-q axis output current, dc voltage, and dc current with conventional and proposed control schemes.....	93
Fig. 75. Simulation waveforms of the α - β axis current and the δ - γ axis current of proposed control scheme.....	94
Fig. 76. Simulation waveforms of three phase voltage, current, and dc power of proposed control scheme.....	94
Fig. 77. Experimental setup of hardware in the loop using RTDS and dSPACE.....	95
Fig. 78. Experimental waveforms of conventional current control under balanced grid voltage.....	96
Fig. 79. Experimental waveforms of conventional current control under unbalanced grid voltage.....	96
Fig. 80. Experimental waveforms of proposed current control under unbalanced grid voltage.....	96
Fig. 81 Circuit diagram of three phase LCL filter based dc-ac inverter.....	101
Fig. 82. Loci of space vectors in the α - β axis and their waveforms in time domain.....	106
Fig. 83. Rotation of axes.....	109

CHAPTER 1. INTRODUCTION

1.1 Overview

The importance of power electronic converters such as dc-dc converters and voltage source inverters is increasing due to increasing distribution-level penetration of renewable energy sources such as photovoltaic and fuel cell technologies. Fig. 1 shows the role of power electronic converters in renewable energy systems. Power electronic converters should send power by regulating dc - dc or dc - ac to the electrical load and the utility grid. Since they are interfaced with renewable sources and electrical loads or the grid, the performance of power electronic converters depends on interactions among sources, loads, and their state of operation. Power electronic converters should be operated with safety and stability under normal conditions, fault conditions, overloads, and different operation modes. However performance of conventional controllers of power electronics converters is limited to minimize impacts on disturbances due to fault conditions and to control different operation modes seamlessly. Therefore, enhanced control strategies of power electronic converters are important to improve the reliability of renewable energy sources and the stability of the grid and the load.

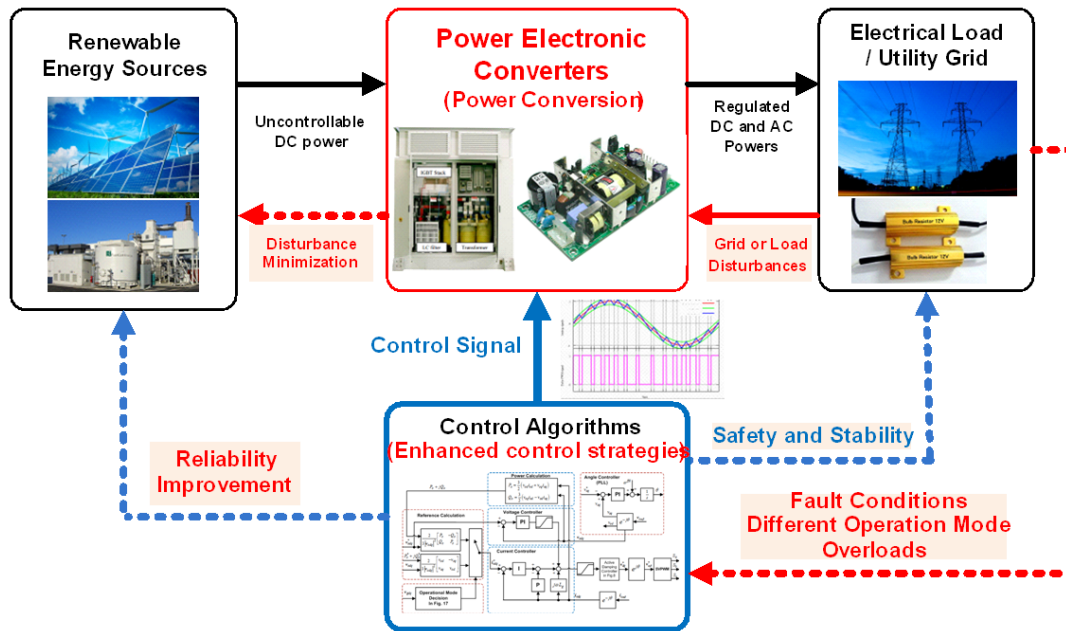


Fig. 1. The role of the power electronic converters in renewable energy systems

This dissertation discusses enhanced control strategies for power electronic converters that improve the reliability and stability of renewable energy systems. First, seamless control for the dc-dc converter with both discontinuous conduction mode (DCM) and continuous conduction mode (CCM) is discussed. Second, a seamless control strategy for the distributed generation (DG) inverter with both a grid connected (GC) mode and a standalone (SA) mode is presented. Third, control strategies for suppression of a dc power oscillation and an ac current distortion of the DG inverter under grid voltage unbalance is discussed. The proposed control strategies reduce the impact of the renewable energy and the load under faults or disturbance conditions. And the stable operation of the power electronic converters will also enhance the stability and reliability of the renewable energy, the grid, and the load.

1.2 Problem Statement

Three control problems are discussed to improve the control performance of the dc-dc converter and the DG inverter under different operation modes and fault conditions; 1) a control of the dc-dc converter with both DCM and CCM, 2) a control of the DG inverter with both the GC mode and the SA mode, and 3) a control to suppress a dc power oscillation of the DG inverter under grid voltage unbalance.

1.2.1 Control of dc-dc converter with mode transition

Fig. 2 shows a typical control scheme of the dc-dc converter. The dc-dc converter operates either in DCM or in CCM. The operation mode is determined by the duty ratio, load and parameters of the dc-dc converter. In particular, it is well known that different mode of the boost converter operation can result in very different dynamics between CCM and DCM plants. Therefore, it will be difficult to design a controller with stable operation and fast transient response for both modes. Moreover, if the dc-dc converter operates in CCM with the DCM control gain or vice versa, it will be unstable.

The CCM boost converter has limitation, which is the resonance point due to double poles and non-minimum phase due to a right half plane zero (RHPZ). Therefore, the CCM boost converter is difficult to design with a compensator of wide range operation. This problem has been solved by designing a conventional voltage-mode control at a low control bandwidth. However, the conventional voltage-mode

control is difficult to obtain fast response time of voltage regulation in both modes because of different dynamics. Therefore the boost converter for portable fuel cell applications is required to operate from very light load (DCM) to regular load (CCM) conditions with a fast and smooth response.

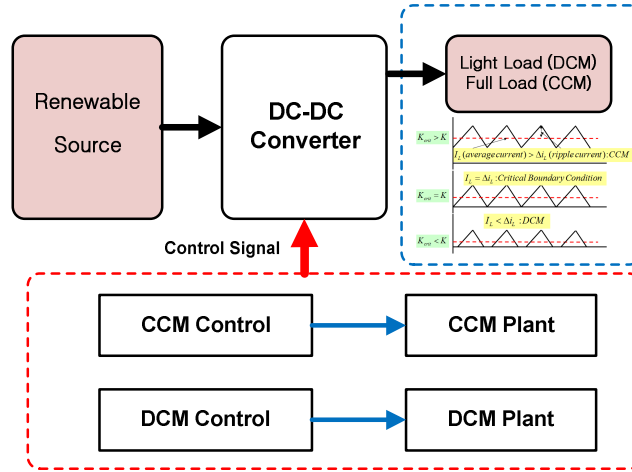


Fig. 2. Control scheme of the dc-dc converter

1.2.2 Control of DG inverter with mode transition

Fig. 3 shows a control scheme of the DG inverter with respect to operational modes. The response time of the voltage controller depends on the critical load variation. The fast mode transition can make unexpected control mode in the overvoltage condition due to the grid voltage swell. The voltage control of the DG inverter connected to the grid is not able to regulate the grid voltage. It will cause the voltage control instability in the worst case. Even though the DG inverter still operates with the voltage control loop for grid connection within short duration, it needs to be changed from the voltage control to the current control in the overvoltage condition due to the grid voltage swell. The voltage control is required to have a fast response time under critical load variation to order to make the fast mode transition in the overvoltage condition due to point common coupling (PCC) switch-off. Therefore, the voltage control is necessary to be designed with considering plants in GC and SA modes. It will satisfy a seamless control of the DG inverter with the critical load safety in overvoltage conditions.

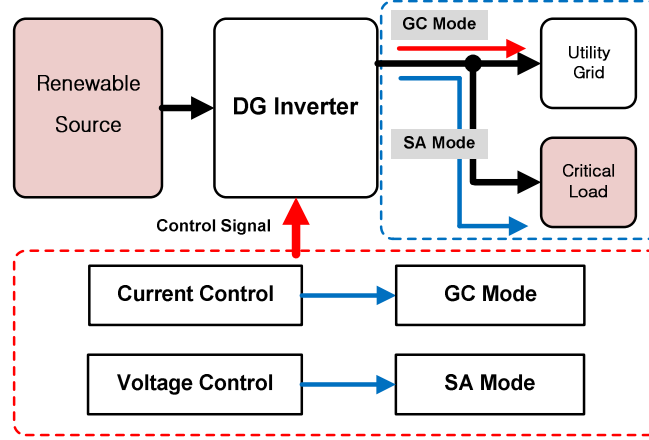


Fig. 3. Control scheme of the DG inverter with respect to operational modes.

1.2.3 Control of DG inverter under grid distortion

Fig. 4 shows a control scheme of the DG inverter under grid voltage unbalance. Conventionally, the double synchronous reference frame current controller is designed with the current reference calculation to suppress the dc voltage oscillation in the L filter based DG inverter. The LCL filter based DG inverter is limited to minimize both dc current and dc voltage oscillations by the conventional reference calculation. Additional current through the capacitor is generated in the LCL filter. However, the conventional current reference calculation is derived with considering the L filter based DG inverter, which assumes that the inverter current is equal to the output current. Therefore, the conventional current calculation is not able to suppress dc voltage and dc current oscillations in the LCL filter based DG inverter.

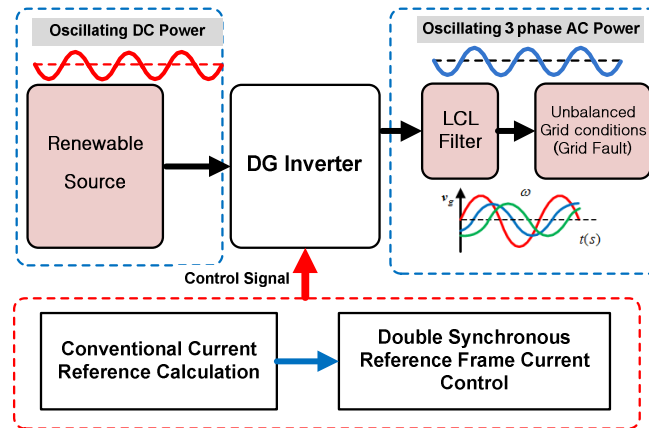


Fig. 4. Control scheme of the DG inverter under grid voltage unbalance and harmonics

1.3 Dissertation Organization

This dissertation is composed of six chapters. The first chapter introduces the importance of control of the power electronic converters in renewable systems and the issues on existing power electronic converter systems. The literature review of control strategies for power electronic converters is presented in chapter 2. Chapter 3 explains a seamless control scheme for the dc-dc converter with different operation modes for both DCM and CCM. Chapter 4 discusses a seamless control for the DG inverter under grid disturbances. Chapter 5 presents a control of *LCL* filter based DG inverters to suppress the dc power oscillation under unbalanced operating conditions is discussed. In chapter 6, this dissertation is summarized with future works.

CHAPTER 2. LITERATURE REVIEW

2.1 Control of dc-dc converter with mode transition

2.2.1 Dc-dc converter for fuel cell applications

The direct borohydride fuel cell (DBFC) is directly fed sodium borohydride as a fuel and hydrogen peroxide as the oxidant. It can be used as the power source for portable applications. Fig. 5 shows the V-I characteristics of the DBFC. It can be seen that if the initial non-linearity (activation polarization) and high current region (concentration polarization) are neglected, the DBFC works in a nearly linear region (ohmic polarization). Considering the linear region, the output voltage of the DBFC varies according to the output current, because of its typical V-I characteristic [1]. Therefore, a dc-dc converter is necessary to regulate the output voltage. In addition, ripple current reduction of the fuel cell is important to increase the life time of a fuel cell stack [2], [3].

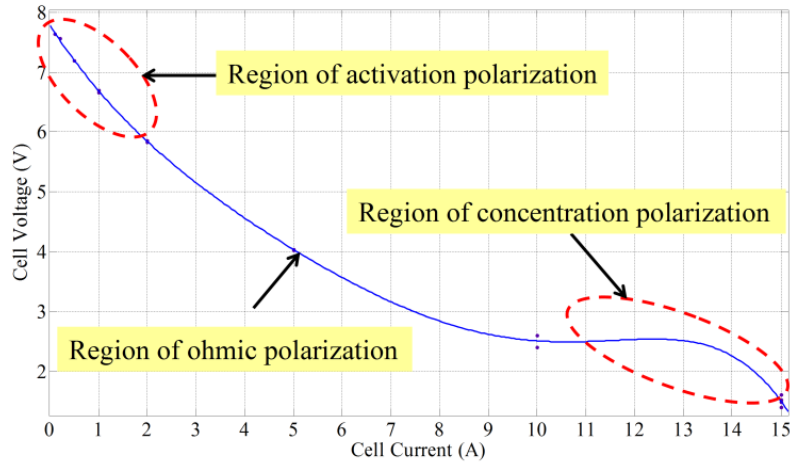


Fig. 5. V-I characteristics of the DBFC [19].

Most fuel cell power converters are expected to produce power on demand, also known as load following power sources. However, the response time of the fuel cells are typically known to be slower than those of other power sources such as batteries and diesel engines. This is because of the operation of the balance of plant (BOP) associated with mass and heat balances inside and outside the stack. In order

to improve the response time, many fuel cell systems are combined with a battery or capacitor to form a hybrid power generation system [4], [5].

A bidirectional dc–dc converter, which is used to interface an ultracapacitor as energy storage to a fuel cell, was presented in [6] and [7]. These papers have shown that the bidirectional converter with the ultracapacitor had better control response times for a fuel cell system during voltage transients. References [8] and [9] proposed a novel hybrid fuel cell power conditioning system. This system consists of the fuel cell, a battery, a unidirectional dc–dc converter, a bidirectional dc–dc converter, and a dc-ac inverter. A fuel cell and a battery are connected to the common dc bus for the unidirectional dc–dc converter and the bidirectional dc–dc converter.

References [10] and [11] reviewed some of the characteristics of fuel cell applications. A discussion of important considerations for fuel cell converter design is presented. The role of the fuel cell controller was briefly introduced. Reference [12] focused on the design of a dc–dc converter, control, and auxiliary energy storage system. A novel converter configuration, which improves utilization of the high frequency transformer and simplifies the overall system control, was proposed.

Stability analysis of fuel cell powered dc-dc converters was also discussed in [13]. An equivalent circuit model based on the chemical reactions inside of the fuel cell was presented. It showed that fuel cell internal impedance can significantly affect the dynamics of the dc-dc converter. Also, the behavior of the fuel cell during purging has been discussed. In order to overcome these problems, the supercapacitor connected in parallel with the fuel cell was proposed. An impedance analysis approach had been proposed in [14] and [15]. It showed the static response of the overall system with the fuel cell and the dc-dc converter. However, it did not clearly show the impact of the individual components.

In [16] and [17], the input impedance of the boost power factor correction converter for both the conventional current controller and the duty ratio feedforward controller were explained theoretically. Due to the nonlinearity and unstable zero dynamics of the boost converter, it has some limitations such as low bandwidth and poor dynamic response [18], [19]. In order to solve this drawback, a novel nonlinear control strategy based on input-output feedback linearization was proposed in [20] and [21].

2.1.2 Control of dc-dc converter with mode transition

The dc-dc converter can be operated in either continuous conduction mode (CCM) or discontinuous conduction mode (DCM). In particular, it is well known that different the boost converter operation modes can result in very different dynamics in the frequency domain. This problem can be solved by designing a conventional voltage-mode control at a low control bandwidth. This can make a stable operation at the critical boundary condition during the transition of the operation mode [22].

In the past two decades, many studies have been done to model dc-dc converters in DCM and CCM. An averaged modelling of dc-dc converters operating in DCM was studied in [23] and [24]. In DCM, these models are represented either as analytical equations or equivalent circuits, and fall into both reduced-order models and full-order models [23]. A method which includes generation, classification and analysis of dc-dc converters was presented in [25]. Three DCM modes of dc-dc converters considered in [26] are the discontinuous inductor current mode, the discontinuous capacitor voltage mode, and an unidentified mode called the discontinuous quasi-resonant mode. A circuit based approach to the analysis of dc-dc converters was presented in [27]. This method was focused on the identification of a three-terminal nonlinear device in the dc-dc converter. An exact small-signal discrete-time model for digitally controlled dc-dc converters operating in CCM was presents in [28]. The analysis of open-loop dynamics relevant to current-mode control for a boost converter operating in CCM was presents in [29]. An averaged state-space modelling of dc-dc converters in CCM and DCM have been developed in [30].

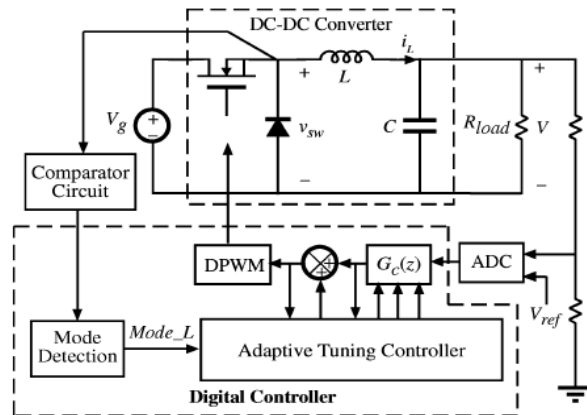


Fig. 6. Block diagram of adaptive tuning algorithm for dc-dc converter [22]

On the other hand, an adaptive tuning algorithm of digital voltage-mode controllers for dc-dc converter was presented to transfer from DCM to CCM [22]. This approach is able to maintain a high performance control without the stability issues by using additional hardware configuration to detect the operation mode. A new hybrid control method was introduced from the basic circuit theory and implemented for the output voltage regulation in the boost converter [31]. The proposed method was designed with analogue and digital circuits. A mixed-mode predictive current control at constant but two different switching frequencies for a single-phase boost power factor correction (PFC) converter has been proposed in [32]. The PFC converter showed the operation in either CCM or DCM depending on the load condition. A simple digital DCM control algorithm in [33] was proposed in order to achieve minimal changes to the average current control in CCM. The algorithm was mathematically and computationally simple. A control scheme for sensorless operation and detection of both CCM and DCM in the dc-dc converter was presented in [34]. The proposed controller utilized dual control loops and did not need the inductor current feedback. A generalization of the recently proposed nonlinear average current control scheme for DCM operation was described in [35]-[37]. The approach was to develop a nonlinear control method for DCM operation by using the same control principle then combining the control method with that for CCM operation.

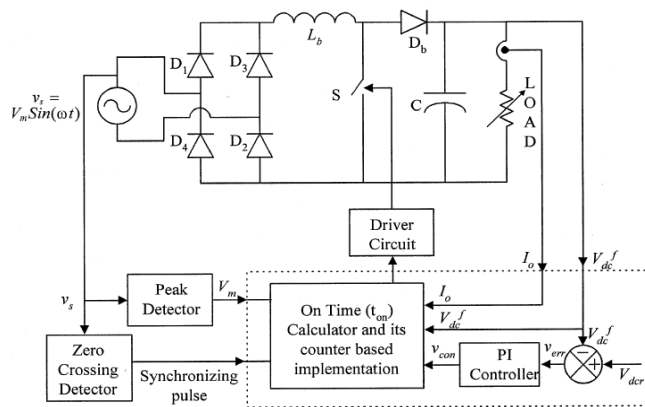


Fig. 7. Mixed-mode operation of boost switch-mode rectifier [32]

A time domain control method of boost converters at the critical boundary condition is proposed to achieve fast dynamic response time under load variations in [38]. Although it has the disadvantage of

requiring a sophisticated analogue circuit, the proposed method can provide fast transient response. Interleaving methods for the critical boundary condition between DCM and CCM of boost PFC converters with master and slave modes was thoroughly analyzed in [39]-[41]. With open and closed loops, the slave converter can be synchronized to the turn-on or to the turn-off instant of the master converter. In both modes, dc-dc converters can be operated by either current mode or voltage mode controls. A dual mode control scheme was proposed in [42] to control a boost PFC converter. The proposed method combined both CCM and the critical boundary condition and had the advantage of simple control and high efficiency under light-load conditions.

However, none of the literature explained clearly how to minimize the impact of the mode transition and implement fully digital control algorithms with a robust mode transition

2.2 Control of DG Inverter with mode transition

2.2.1 Current control in the GC mode

The use of the renewable energy is increasing rapidly at a growing rate. The growth in renewable generation is expected to 26 percent of the total generation growth from 2009 to 2035 in U.S.A [43]. Therefore, utility companies have already begun to take into account not only the conventional centralized power generation, transmission, and distribution, but also renewable energy based distributed generations.

Most distributed generations (DG) is connected to the grid by using the voltage source dc-ac inverter. The inverter controller stabilizes the dc-link voltage and supplies active and reactive powers to the grid by regulating ac current at a certain power factor. The control schemes for the DG inverter are implemented based on a synchronous reference frame control and a stationary reference frame control. The synchronous reference frame current control or $d-q$ current control regulates the $d-q$ axis current with the $d-q$ transformation and proportional-integral (PI) controller. [44], [45], [46]. Stationary reference frame control or the $\alpha-\beta$ current control regulates the $\alpha-\beta$ axis current from the $\alpha-\beta$ transformation and proportional-resonant (PR) controller [47]–[51]. As a kind of fast current controller, it is known that dead-

beat or predictive controllers provide the fastest response time. However, there could be the stability issue because of the delay time and parameter variations in the digital domain [52]–[62].

2.2.2 Voltage control in the SA mode

There are many approaches to regulate the ac output voltages of the inverter in ac power supplies or uninterruptible power supplies (UPS). The current control for over-current protection is used in an inner loop and the voltage control for output voltage regulation is implemented in the outer loop with either the synchronous reference frame or stationary reference frame. However, this method has issues about voltage distortion under nonlinear loads and response time under variable loads. It is important to develop robust control schemes [63]–[74]. Diverse high performance control methods have been developed, such as repetitive-based control [67], deadbeat control [68]–[74] in order to increase the voltage loop bandwidth.

2.2.3 Mode transition approach

With increasing renewable DGs, fast and stable mode transition technologies are substantial not only for sending power to the grid, but also for protecting DGs from grid fault conditions. Particularly, to supply power to the critical loads in any grid conditions has become an important issue [75], because most critical loads are sensitive to voltage variations, which can make the critical loads' performance worse or shut down the system operation.

In the literature, two categories of critical loads have been discussed. One is the grid-scale power loads requiring very high quality of power including medical equipment, semiconductor industry, and broadcasting facilities [75 - 77]. The other is to supply the auxiliary power in renewable or energy storage power systems [78 - 79].

A low-cost power electronics stage to provide ride-through capability for critical loads has been explored [75]. The use of a micro high-temperature superconducting magnetic energy storage system was proposed to support critical industrial loads with a ride-through capability of around 20 cycles [76]. The micro-wind energy conversion scheme with battery energy storage was proposed as support for the critical load [77]. The dc-ac inverter in current controlled mode exchanges active and reactive power. The

approach provides continuous power to the critical load under operational modes. A control algorithm for fault ride through with voltage compensation capability for the critical load is proposed in a three-phase utility-interactive inverter with a critical load [78].

Fig. 8 shows a molten carbonate fuel cell (MCFC) power plant which is composed of a fuel cell stack, mechanical balance of plant (MBOP) and electrical balance of plant (EBOP). The safeties of the MBOP and EBOP are very important and considered as critical loads in operating fuel cell power plant systems [79 - 81]. A new voltage sag compensator for powering critical loads in electric distribution systems has been discussed in an ac–ac converter [82].

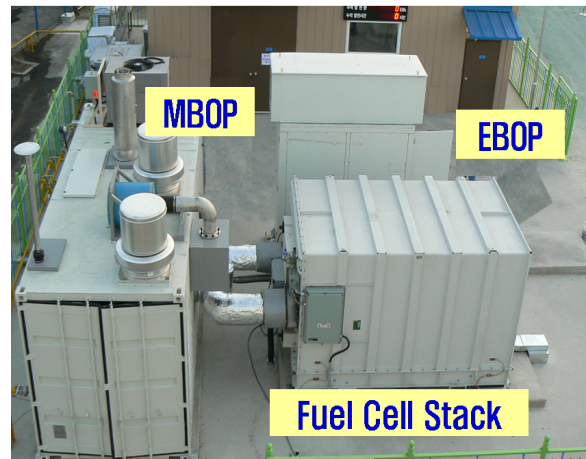


Fig. 8. MCFC power plant [80]

Fig. 9 shows a systemic configuration of DG inverter [83]. Usually, the DG has a dc-ac inverter based power conversion system, which is either to deliver power to the grid or to supply power to the load. In the grid connected (GC) mode, DG inverters control the output current with respect to the voltage phase angle to send power to the grid. In standalone (SA) mode, DG inverters supply power to the critical or local load by regulating the output voltage. Two physical switches connect or disconnect DGs. The mode switch is turned on and connected to the grid in GC mode and is turned off in SA mode under grid fault conditions. It can use a static transfer switch or circuit breaker [84]. The point of common coupling (PCC) switch is another protection switch. If the grid is under fault conditions such as over / under voltage, over / under frequency etc., then the DG is disconnected from the grid for the protection of the critical load and DG inverter. If the auxiliary power of the DG inverter control board supplies from the grid as a critical

load, the DG inverter should operate in both GC and SA modes to provide uninterrupted and continuous power [85]. Therefore, it is important that the DG inverter controller can detect exact fault conditions and transfer the seamless operational mode within allowable duration to reduce the voltage and current spikes.

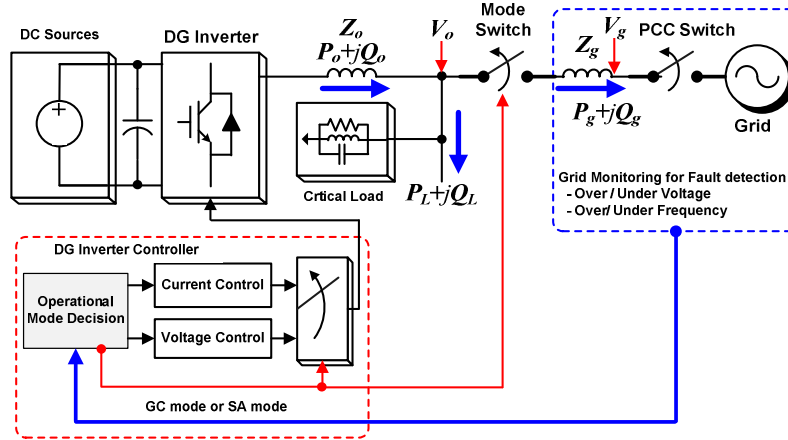


Fig. 9. DG inverter system configuration with mode transition

Seamless mode transition controls have been investigated [86 - 97]. A seamless transfer algorithm can switch the inverter operation from voltage-controlled mode to current-controlled mode and vice versa with minimum interruption to the load [92]. The use of the mode switch helps in disconnecting the grid within a half line cycle. An indirect current control algorithm for seamless transfer of utility-interactive voltage source inverters has been proposed [93-94]. Fig. 10 shows the indirect current control for seamless transfer of three-phase utility interactive inverters [93]. With the proposed method, the DG inverter is able to provide critical loads with a stable and seamless voltage during the whole transition period including both clearing time and control mode change. A seamless transfer of single-phase grid-interactive inverters between GC and SA mode was presented [95]. The transfer between both modes is just the change of the reference voltage, so the transfer between the output voltage controller and the grid current controller does not exist in the proposed method. Wang *et al.* [96] described four different mode combinations with two switches. Switch one is to control the mode between current control and voltage control, and the other switch is to control two operation modes between GC mode and SA mode. The weighted parameter current / voltage control scheme showed good performance. However, practically, it requires additional tuning procedures with respect to the power rating, transfer switch delay time, and

control loop sample time. Teodorescu *et al.* [97] presented the development and test of a flexible control strategy for an 11-kW wind turbine with a back-to-back power converter capable of working in both SA and GC.

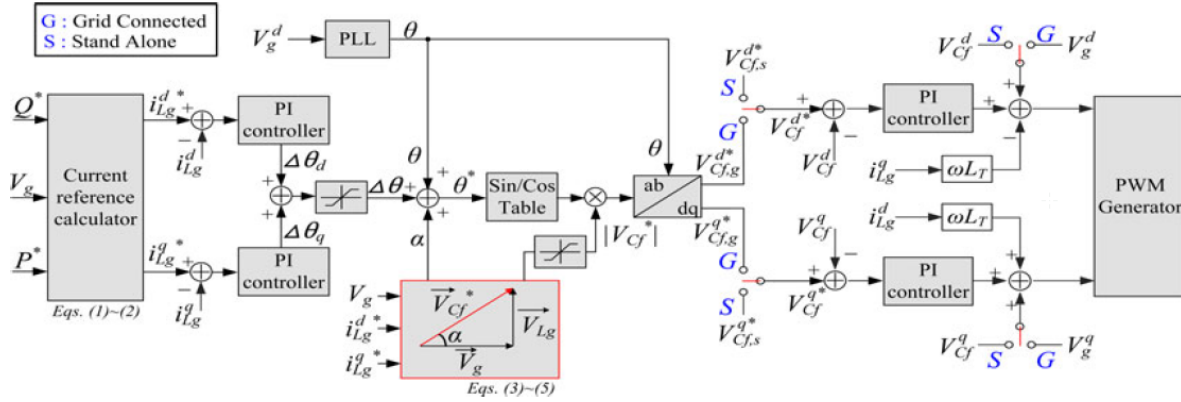


Fig. 10. Indirect current control for seamless transfer of three-phase utility interactive inverters [93]

2.3 Control of DG inverter under grid voltage unbalance

The importance of the voltage source inverters (VSI) is increasing recently, due to the increments of DG represented mostly by renewable energy sources such as solar and wind energy. This VSI should guarantee the safety of the equipment and control the current injected by the DG into the grid supports the voltage [98 - 99].

When a fault occurs, unbalanced grid voltage appears. Then, the current injected into the grid affects their sinusoidal and balanced power flow. Furthermore, the interaction between unbalanced voltage and current would create unregulated oscillation in the active and reactive powers delivery to the grid as well as current and voltage ripples to the dc link. So far, there have been many studies on the control strategy to reduce current and voltage ripples under unbalanced grid voltage. Among them, a control strategy to directly regulate the instantaneous active power to a constant state without any ripple components has been considered to show the most effective method [100– 110].

A dual current control was proposed to minimize the dc link voltage ripple with the positive- and negative-sequence current controllers in synchronous reference frame [101-104]. A new current-reference generator implemented directly in stationary reference frame was proposed [105]. A flexible active power

control based on a fast current controller and a various current reference generator was explained [106]. Wang et al. [107] has proposed methods for independent active and reactive power control of DG inverters under unbalanced grid voltage. The impact of the positive- and negative-sequence components on the instantaneous power and interactions between the positive- and negative-sequence has been explained in detail.

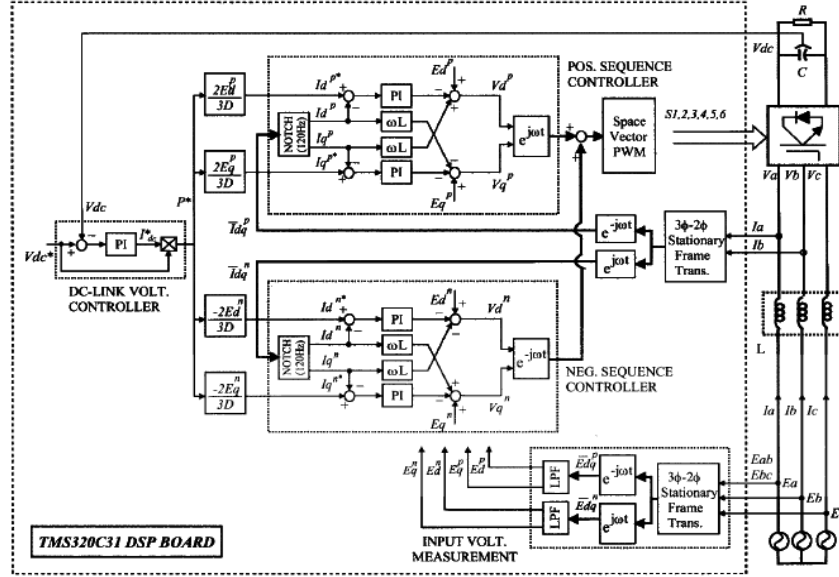


Fig. 11. Dual current control scheme in synchronous reference frame for PWM converter under unbalanced input voltage conditions [101]

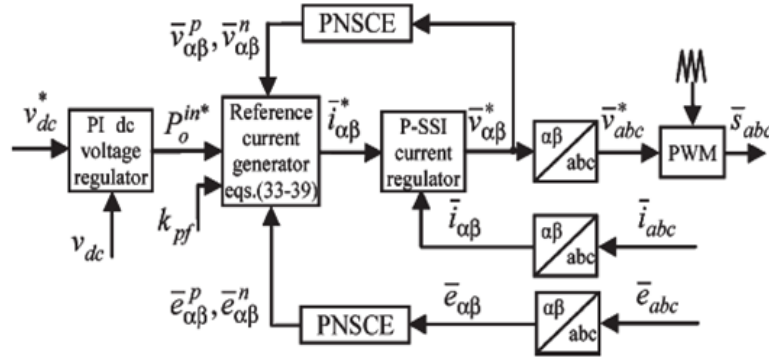


Fig. 12. New stationary frame control scheme for three-phase PWM rectifiers under unbalanced voltage dips conditions [105]

A control and operation of doubly fed induction generator based wind power systems under unbalanced grid voltage was investigated [108]. An input-power, input-output-power, and output-power control methods for PWM rectifier under unbalanced grid voltage are proposed in single stationary reference

frame [109]. A supplementary dc voltage ripple suppressing controller to eliminate the second-order harmonic in the dc voltage of the MMC-HVDC system was presented [110].

On the other hand, the current ripple in the dc link can affect the fuel cell capacity as well as the fuel cell reliability [111-112]. The results showed that the fuel cell not only needs higher power capability, but also consumes 10% more fuels [111]. An advanced active control method, which uses linearized ac signal model of ripple current path, has been proposed to incorporate a current control loop in the dc-dc converter for the reduction of current ripple [21].

In summary, none of the literature explained clearly how to minimize the impact of the mode transition for the DG inverters. And also they showed the control performance to suppress the only dc voltage oscillation of the *LCL* filter based DG inverters under unbalanced operating conditions. Therefore, the conventional approaches are limited to suppress both dc voltage and dc current of DG inverters under grid voltage unbalance.

CHAPTER 3. SEAMLESS CONTROL OF DC-DC CONVERTERS BETWEEN DCM AND CCM

The boost converter operates either in discontinuous conduction mode (DCM) or in continuous conduction mode (CCM)¹. The operation mode is determined by the duty ratio, load and parameters of the boost converter. The plant models in DCM and CCM are different in the frequency domain. Therefore, it will be difficult to design a controller with stable operation and fast transient response for both modes. Moreover, if the boost converter operates in CCM with the DCM control gain or vice versa, it will be unstable.

The proposed control strategy can make mode transitions between DCM and CCM seamlessly by adding a mode tracker, and then the boost converter can autonomously operate by selecting the appropriate control loop in both operation modes. The proposed controller still has a voltage control loop in DCM and current/voltage control loops in CCM. The proposed mode tracker will be explained with a frequency domain analysis. In the case of a portable fuel cell, the boost converter is required to operate from very light load (DCM) to regular load (CCM) conditions. Because of the wide range operation of the portable fuel cell, the strategy of proposed smooth mode transition will be suitable. In addition, smooth operation of the converter will also be beneficial to the reliability of the fuel cell stack. A 20 W boost converter prototype will be used to verify the performance of the proposed control scheme.

3.1 Boost Converter Modeling In DCM and CCM

3.1.1 Small signal modeling in CCM and DCM

Fig.13 shows a typical boost converter configuration. Equations based on the average model of the boost converter in CCM are given in (1) and (2) [113].

$$\frac{di_L}{dt} = \frac{v_i}{L} - \frac{(1-d)v_o}{L} \quad (1)$$

¹ Most of the results presented in this chapter have been published in [136], and [137].

$$\frac{dv_o}{dt} = \frac{(1-d)i_L}{C} - \frac{v_o}{RC} \quad (2)$$

where, v_i is the input voltage, i_L is the inductor current, v_o is the output voltage, L is the inductance, C is the filter capacitance, R is the load resistor, and d is the duty ratio.

In (1) and (2), small-signal model equations in CCM can be written as

$$\frac{d\tilde{i}_L}{dt} = \frac{\tilde{v}_i}{L} - \frac{(1-D)\tilde{v}_o}{L} + \frac{V_o}{L} \tilde{d} \quad (3)$$

$$\frac{d\tilde{v}_o}{dt} = -\frac{I_L \tilde{d}}{C} + \frac{(1-D)\tilde{i}_L}{C} - \frac{\tilde{v}_o}{RC} \quad (4)$$

where, D is the dc component of on-duty cycle of switch, V_o is the dc component of the output voltage, and I_L is the dc component of the inductor current.

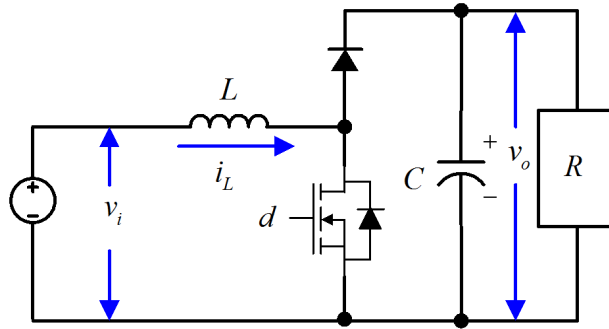


Fig. 13. Boost converter configuration.

On the other hand, average model equations in DCM are presented in (5) and (6)

$$i_L = \frac{v_i}{2L} \frac{d^2 T_s v_o}{v_o - v_i} \quad (5)$$

$$\frac{dv_o}{dt} = \frac{v_i}{v_o} \frac{i_L}{C} - \frac{v_o}{RC} \quad (6)$$

where, T_s is the switching time[23].

The small signal model equations in DCM are written in (7) and (8)

$$\tilde{i}_L = \frac{2I_L}{D} \tilde{d} \quad (7)$$

$$\frac{d\tilde{v}_o}{dt} = \frac{V_i}{V_o C} \tilde{i}_L + \frac{I_L}{V_o C} \tilde{v}_i - \frac{2}{RC} \tilde{v}_o \quad (8)$$

Then, the duty ratio-to-inductor current transfer function and the inductor current-to-output voltage transfer function in CCM are given as

$$G_{di_CCM}(s) = \left. \frac{\tilde{i}_L}{\tilde{d}} \right|_{\tilde{v}_i=0} = \frac{RCV_o s + V_o + (1-D)I_L R}{RLCs^2 + Ls + (1-D)^2 R} \quad (9)$$

$$G_{iv_CCM}(s) = \left. \frac{\tilde{v}_o}{\tilde{i}_L} \right|_{\tilde{v}_i=0} = \frac{-RI_L Ls + (1-D)V_o R}{RCV_o s + V_o + (1-D)I_L R} \quad (10)$$

The duty ratio-to-inductor current transfer function and the inductor current-to-output voltage transfer function in DCM are given as

$$G_{di_DCM}(s) = \left. \frac{\tilde{i}_L}{\tilde{d}} \right|_{\tilde{v}_i=0} = \frac{2I_L}{D} \quad (11)$$

$$G_{iv_DCM}(s) = \left. \frac{\tilde{v}_o}{\tilde{i}_L} \right|_{\tilde{v}_i=0} = \frac{V_o}{I_L} \frac{1}{RCs + 2} \quad (12)$$

In the reduced-order models, the inductor current is defined as a constant value in (5) and (7). This means that the boost converter in DCM will be designed with only voltage control.

3.1.2 Mode Boundary [113]

In order to choose between DCM and CCM, a critical load resistance, R_{crit} , is defined as

$$R_{crit} = \frac{2L}{D(1-D)^2 T_s} \quad (13)$$

$$R_{crit} < R \text{ in DCM , and } R_{crit} > R \text{ in CCM} \quad (14)$$

On the other hand, a critical boundary condition, K_{crit} , is defined as

$$K_{crit} = D(1-D)^2 \quad (15)$$

$$K_{crit} > K \text{ in DCM , } K_{crit} < K \text{ in CCM} \quad (16)$$

$$K = \frac{2L}{T_s R} \quad (17)$$

3.1.3 Issues with Designing the Controller for both CCM and DCM

Fig. 14 shows the frequency responses of the duty ratio-to-output voltage transfer function in CCM and DCM. The CCM boost converter shown in Fig. 14 (a) has limitations, which is the resonance point due to double poles and non-minimum phase due to a right half plane zero (RHPZ). They can affect the cutoff frequency when a compensator is designed. In the worst case, it is difficult to achieve a stable phase margin with high bandwidth. Therefore, the CCM boost converter is difficult to design with a compensator of wide range operation. On the other hand, the DCM boost converter shown in Fig. 14 (b) is a first order system. In order to achieve a high bandwidth, PI or lead-lag compensator can be used easily. Fig. 15 (a) shows a loop gain of compensator designed in DCM. The phase margin (PM) is 90° and the bandwidth (BW) is 100Hz. The designed PI compensator, $G_{C1}(s)$, is given as

$$G_{C1}(s) = 18.27 + \frac{1.827}{s} \quad (18)$$

However, this compensator will be unstable in CCM as shown Fig. 15 (a). A stable compensator, $G_{C2}(s)$, in both DCM and CCM shown in Fig. 15 (b) is derived as

$$G_{C2}(s) = \frac{4.1657}{s} \quad (19)$$

The phase margin is 44.6° in DCM and 90° in CCM. And the bandwidth is about 16Hz. In order to design the stable controller in both modes, the bandwidth is decreased from 100Hz to 16Hz. This implies that it can be difficult to design a stable controller with a fast response time in both DCM and CCM.

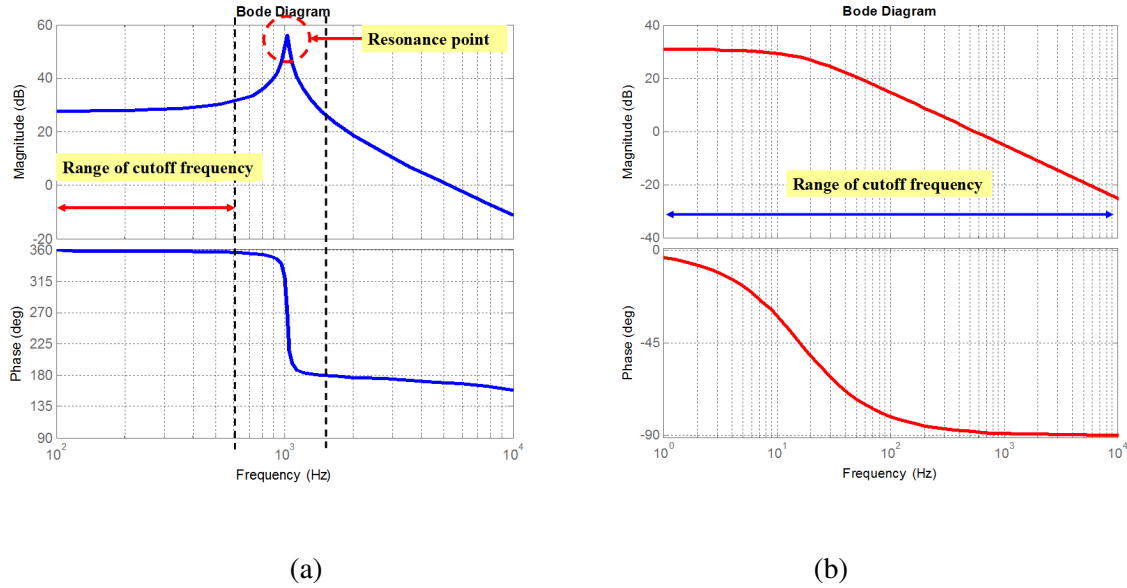


Fig. 14. Frequency responses of the duty ratio-to-output voltage transfer function in CCM and DCM. (a) CCM boost converter. (b) DCM boost converter.

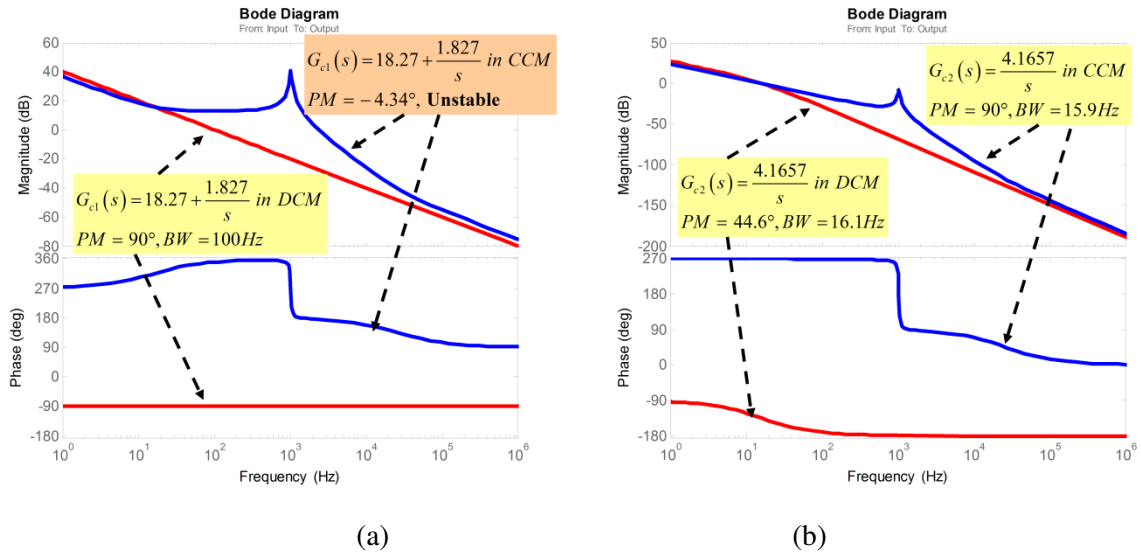


Fig. 15. Loop gains of compensator according to DCM and CCM. (a) Loop gain of compensator designed in DCM. (b) Loop gain of compensator designed in both modes.

3.2 Proposed Controller Design in DCM and CCM

3.2.1 Current Control in CCM [114]

From Fig. 14 (a) the boost converter in CCM has a high resonant pole in the duty ratio-to- inductor current transfer function and the RHPZ in the inductor current-to-output voltage transfer function. In order to cancel the high resonance pole, a nonlinear feedforward scheme has been proposed [20]. With this method, the duty ratio of the boost converter is calculated as

$$d = 1 - \frac{v_i}{v_o} + \frac{v_c}{v_o} \quad (20)$$

Equations in the average model are expressed in

$$\frac{di_L}{dt} = \frac{v_c}{L} \quad (21)$$

$$\frac{dv_o}{dt} = \frac{v_i i_L}{C v_o} - \frac{i_L d_c}{C} - \frac{v_o}{RC} \quad (22)$$

Hence, equations in the small-signal model are written as

$$\frac{d\tilde{i}_L}{dt} = \frac{\tilde{v}_c}{L} \quad (23)$$

$$\frac{d\tilde{v}_o}{dt} = \frac{V_i}{CV_o} \tilde{i}_L - \frac{2}{RC} \tilde{v}_o - \frac{I_L}{CV_o} \tilde{v}_c + \frac{I_L}{CV_o} \tilde{v}_i \quad (24)$$

Transfer functions of the boost converter by nonlinear feedforward are given as

$$G_{v_c i_CCM_FFD}(s) = \left. \frac{\tilde{i}_L}{\tilde{v}_c} \right|_{\tilde{v}_i=0} = \frac{V_o}{Ls} \quad (25)$$

$$G_{iv_CCM_FFD} = \left. \frac{\tilde{v}_o}{\tilde{i}_L} \right|_{\tilde{v}_i=0} = \frac{V_o}{I_L} \frac{-LI_L/V_i s + 1}{RCs + 2} \quad (26)$$

Fig. 16 shows the block diagram of the proposed current control with nonlinear feedforward in CCM.

By using the nonlinear feedforward, the plant can be simplified as (25). The control gains are $k_{pc} = L\omega_c$,

$k_{ic} = r\omega_c$ and $k_{vc} = r$, and ω_c is the control bandwidth.

Then, the overall closed loop transfer function becomes

$$\frac{\tilde{i}_L^*}{\tilde{i}_L} = \frac{k_{pc}/Ls + k_{ic}/L}{s^2 + (k_{vc} + k_{pc})/Ls + k_{ic}/L} = \frac{\omega_c s + r\omega_c}{s^2 + (\omega_c + r)s + r\omega_c} = \frac{\omega_c (s + r)}{(s + \omega_c)(s + r)} = \frac{\omega_c}{s + \omega_c} \quad (27)$$

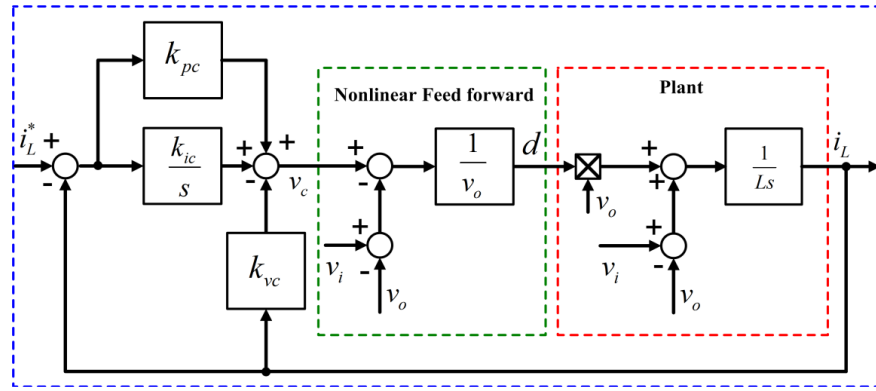


Fig. 16. Block diagram of proposed current control with nonlinear feedforward in CCM.

3.2. 2 Feedforward Current Control in DCM

Fig. 17 shows the block diagram of feedforward current control in DCM. Since there are no state variables in DCM, the feedforward scheme is used without a feedback loop. As the voltage control in the outer loop is connected, the voltage-mode control is activated.

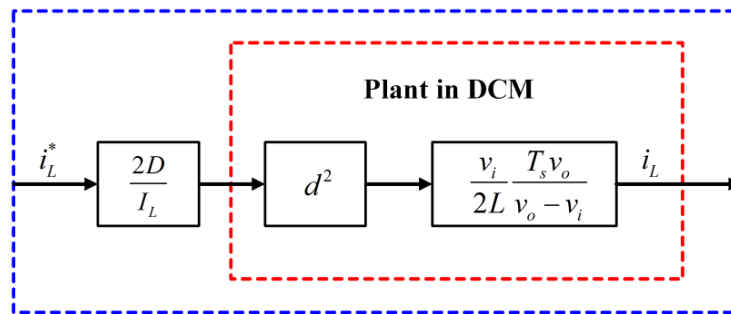


Fig. 17. Block diagram of feedforward current control in DCM.

3.2.3 Voltage Control in both CCM and DCM

Fig. 18 shows the block diagram of voltage control in CCM. The current control shown in Fig.4 is located in the inner loop. In the outer loop, it can assume that current loop gain is equal to 1 because inner loop is faster than the outer loop. The inductor current-to-output voltage transfer function with nonlinear feedforward in CCM, $G_{iv_CCM_FFD}(s)$, has the RHPZ with comparison of the inductor current-to-output voltage transfer function in DCM, $G_{iv_DCM}(s)$. This means that it has the RHPZ in CCM but disappears in DCM.

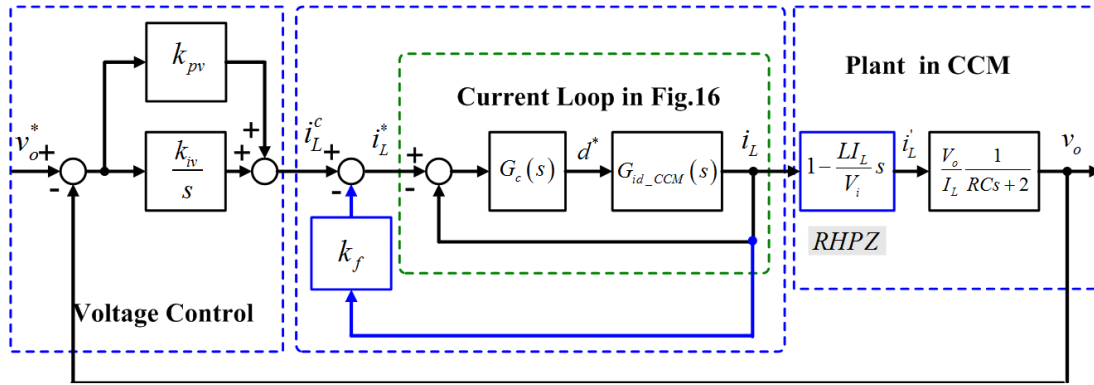


Fig. 18. Block diagram of voltage control in CCM.

From Fig. 18, the transfer function from i_L^c to i_L is given as

$$\frac{i_L}{i_L^c} = \frac{\omega_c}{s + \omega_c(1 + k_f)} \quad (28)$$

where, k_f is the feedforward gain in the voltage loop.

And it can be rewritten as

$$\frac{i_L}{i_L^c} = \frac{\omega_c \left(1 - \frac{s}{\alpha_z}\right)}{s + \omega_c(1 + k_f)} = \frac{\omega_c}{\alpha_z} \frac{-s + \alpha_z}{s + \omega_c(1 + k_f)} \quad (29)$$

where $\alpha_z = V_i / LI_L$.

The feedforward gain, k_f , is defined as

$$\omega_c (1 + k_f) = \alpha_z \text{ or } k_f = \frac{\alpha_z}{\omega_c} - 1 \quad (30)$$

As canceling with the all pass filter, the impact of RHPZ will be minimized. Hence the transfer function from i_L' to i_L can be approximated as

$$\frac{i_L'}{i_L^c} = \frac{\omega_c}{\omega_c (1 + k_f)} \frac{-s + \alpha_z}{s + \alpha_z} = \frac{1}{1 + k_f} \quad (31)$$

Fig. 19 shows the block diagram of voltage control in DCM. The feedforward current control shown in Fig.17 is connected.

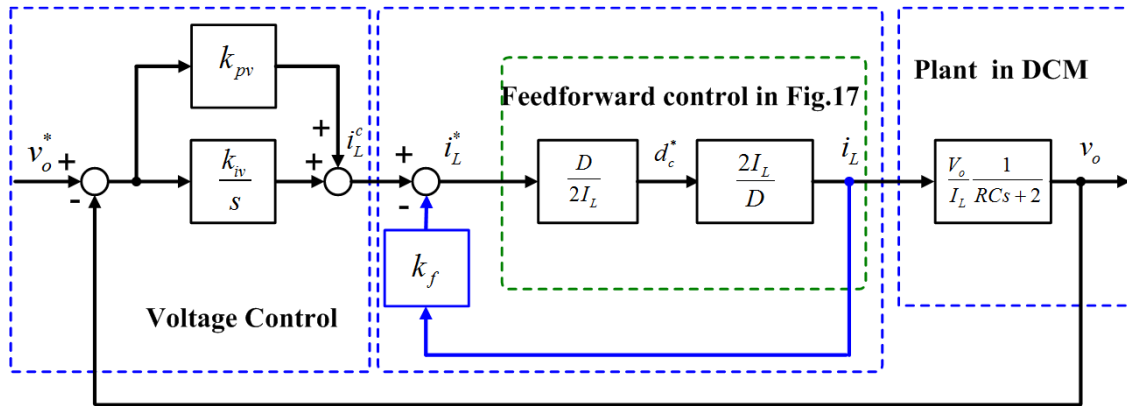


Fig. 19. Block diagram of voltage control in DCM.

From Fig. 19, the transfer function from i_L^c to i_L is given as

$$\frac{i_L}{i_L^c} = \frac{1}{1 + k_f} \quad (32)$$

The result is the same as (31). This means that the voltage control with the feedforward term in CCM can be used in DCM. Therefore, the same voltage control in outer loop is always applied and the current control in inner loop operates according to the operation mode.

3.2. 4 Proposed Seamless Control System with Mode Tracker

Fig. 20 shows the proposed control block diagram with a mode tracker. DCM and CCM will be determined by (13) - (17). From the critical boundary condition, K_{crit} , is calculated by the duty ratio, D . Based on the output current, i_o , and the output voltage, v_o , the instantaneous load resistor, \hat{R} , can be obtained in the boost converter. Then, the mode decision parameter, K , will be determined by \hat{R} . To avoid continuous variations of K , the low pass filter (LPF) is necessary. \hat{K} is the result of applying the LPF to K . \hat{K} will affect the transient response time of the output voltage during mode transitions. In the mode tracker, K_{crit} is a set point and \hat{K} is a variable signal with respect to the mode transitions. The difference between K_{crit} and \hat{K} implies the mode conditions. If K_{crit} is greater than \hat{K} , the mode is CCM. If K_{crit} is less than \hat{K} , the mode is DCM. If K_{crit} is equal to \hat{K} , it will be at the critical boundary condition. The output of the proportional error amplifier, k_{pm} , is a factor for decision of the operation mode. If the error is close to a zero, this implies the system is near the critical boundary condition. The value of critical boundary condition needs to be shifted from 0.0 to 0.5 because the mixed control gain is defined within $0 \leq k_m \leq 1$. Therefore, an offset value of 0.5 is added in the output of k_{pm} . In DCM and CCM, the error will increase continuously. A limiter is used in order to make DCM and CCM result in maximum and minimum values of k_m . Therefore, the mixed control gain contains values within $0 \leq k_m \leq 1$. If it is close to 0.5, the system is near the critical boundary condition between CCM and DCM. If k_m is 1 or 0 then it is operating in CCM or DCM. In the case of some value between 0 and 1, k_m will be proportional to the operating conditions.

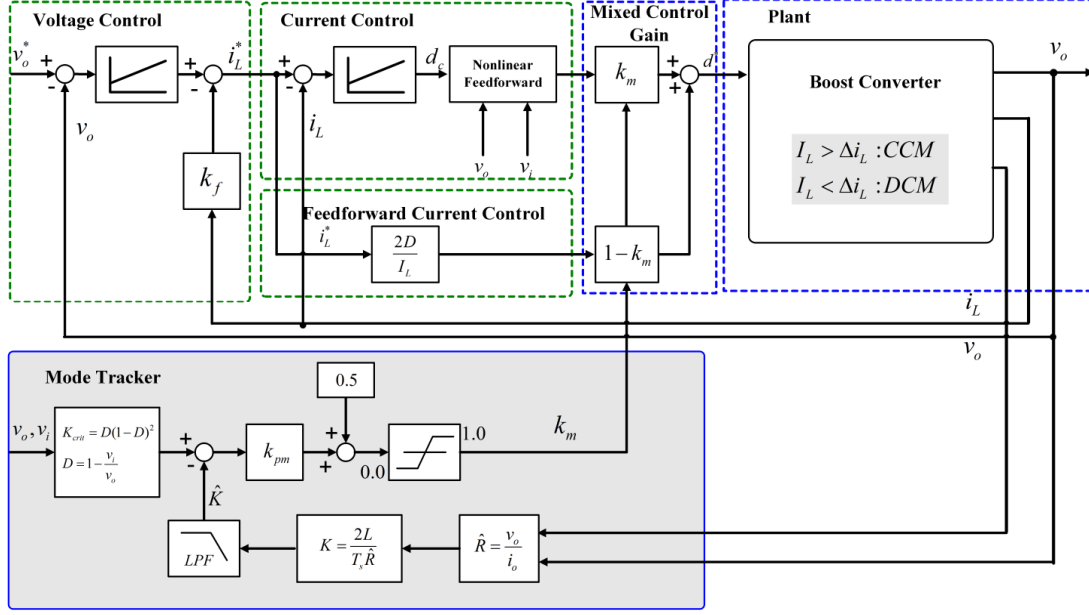


Fig. 20. Proposed control block diagram with a mode tracker.

3.2.5 Stability and Robustness of Seamless Mode Transition

In order to get K_{crit} and K , feedback signals $(i_L, \dot{i}_o, v_i, v_o)$ need to be measured. When feedback signals are measured, there is some noises and error. Therefore, it will be difficult to track an exact operation mode. Moreover, the critical boundary condition supposes that k_m corresponds exactly to 0.5. However, operation mode can be either CCM or DCM with some margin. As a result, there can be unexpected transitions between both controllers. To verify robustness under parameter variations and feedback signal errors, the proposed mode tracker is analyzed in the frequency domain. The analysis assumes that the error of k_m is about 10%. In this case, k_m at the critical boundary condition ranges from 0.4 to 0.6. Fig. 21 shows the mixed control block diagram with respect to CCM, DCM and k_m . We consider two cases. First, the mixed controller shown in Fig. 22 is activated and the boost converter is operated in CCM and the critical boundary condition ($0.4 < k_m \leq 1.0$). Second, the mixed controller is activated and the boost converter is operated in DCM and the critical boundary condition ($0 \leq k_m < 0.6$).

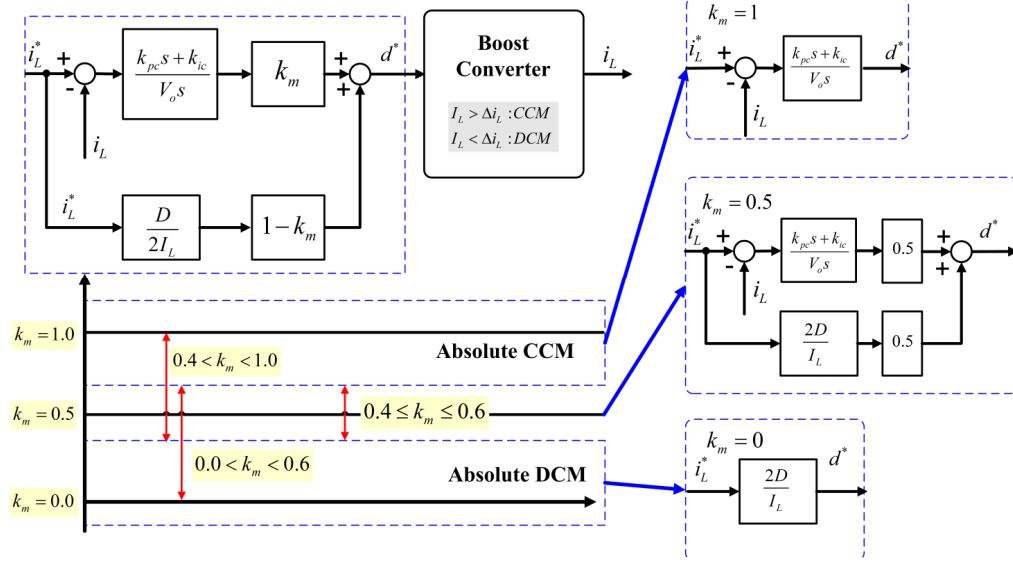


Fig. 21. Mixed control block diagram with respect to the operation mode and k_m .

If the mixed controller is operating in CCM and the critical boundary condition ($0.4 < k_m \leq 1.0$), the closed loop transfer function is given as

$$T_{cl1}(s) = \frac{(L\omega_c k_m + 0.5DV_o(1 - k_m)/I_L)s + r\omega_c k_m}{Ls^2 + (r + L\omega_c k_m)s + r\omega_c k_m} \quad (33)$$

In the case where k_m is 1, the transfer function is calculated as

$$T_{cl1}(s) = \frac{\omega_c}{s + \omega_c} \quad (34)$$

This is expected for the voltage regulation in CCM. On the other hand, when the mixed controller operates in DCM and the critical boundary condition ($0 \leq k_m < 0.6$), the closed loop transfer function is expressed as

$$T_{cl2}(s) = \frac{(2D(1 - k_m) + I_L k_{pc} k_m)s + I_L k_{ic} k_m}{(I_L k_{pc} k_m + 2D)s + I_L k_{ic} k_m} \quad (35)$$

When k_m is zero, the transfer function is calculated as

$$T_{cl1}(s) = 1 \quad (36)$$

This is also expected for the voltage regulation in DCM. However, the cases of $0.4 \leq k_m \leq 0.6$ can result in unexpected transitions due to an uncertainty of the mode tracker. Based on the frequency domain analysis, it determines the system stability during transitions.

The open loop gain of mixed controller with respect to CCM plant ($0.4 \leq k_m \leq 0.6$) is given as

$$T_1(s) = \frac{k_p k_m s + k_i k_m}{Ls^2 + rs} \quad (37)$$

The open loop gain of mixed controller with respect to DCM plant ($0.4 \leq k_m \leq 0.6$) is given as

$$T_2(s) = \frac{2k_p k_m I_L s + 2k_i k_m I_L}{DV_o s} \quad (38)$$

Fig. 22 shows the Bode plot of $T_1(s)$. The cutoff frequency is about from 300Hz to 500Hz for $0.4 \leq k_m \leq 0.6$. Fig. 23 shows the bode plot of $T_2(s)$. The cutoff frequency is about from 80Hz to 100Hz for $0.4 \leq k_m \leq 0.6$. The cutoff frequency of the current loop in Fig. 16 is about 1kHz. However, due to k_m , the overall bandwidth is decreased. Therefore the cutoff frequency of the mixed control loop in Fig. 21 is slower than the cutoff frequency of the original control mode. However, both phase margins in loop gains are about 90° , which means they are stable during mode transitions. Hence, the proposed method can carry out the mode transition without instability.

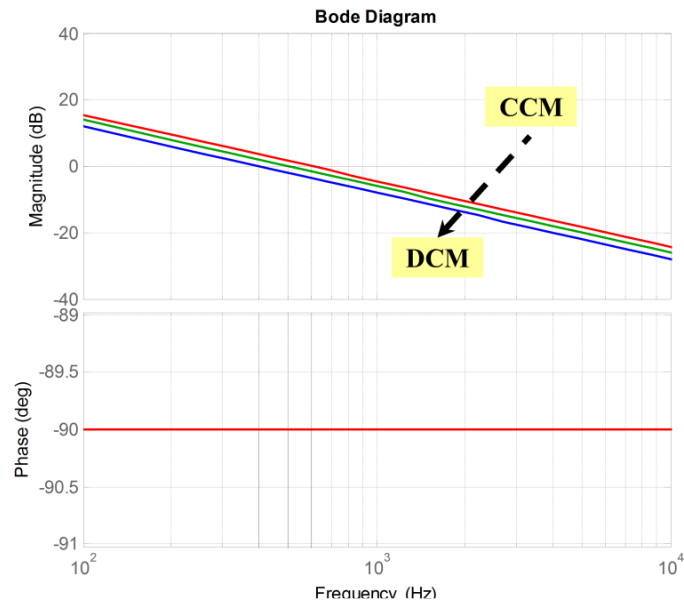


Fig. 22. Bode plot of $T_1(s)$ ($0.4 \leq k_m \leq 0.6$).

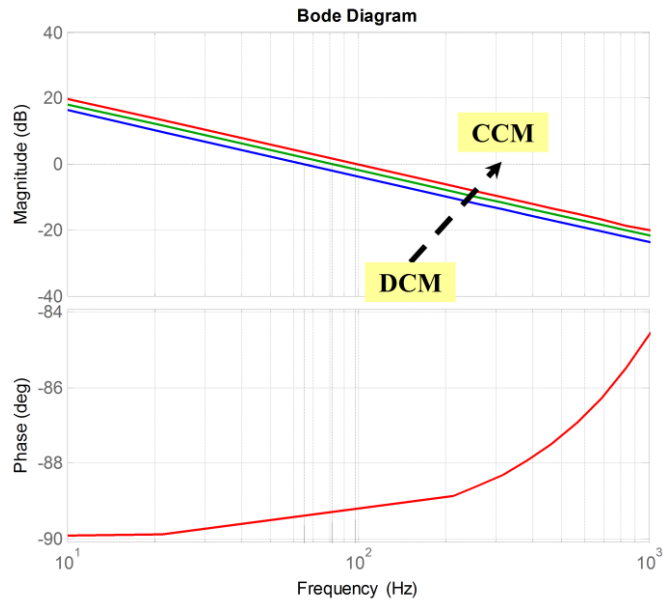


Fig. 23. Bode plot of $T_2(s)$ ($0.4 \leq k_m \leq 0.6$).

3.2.6 Transient Response during the mode transition

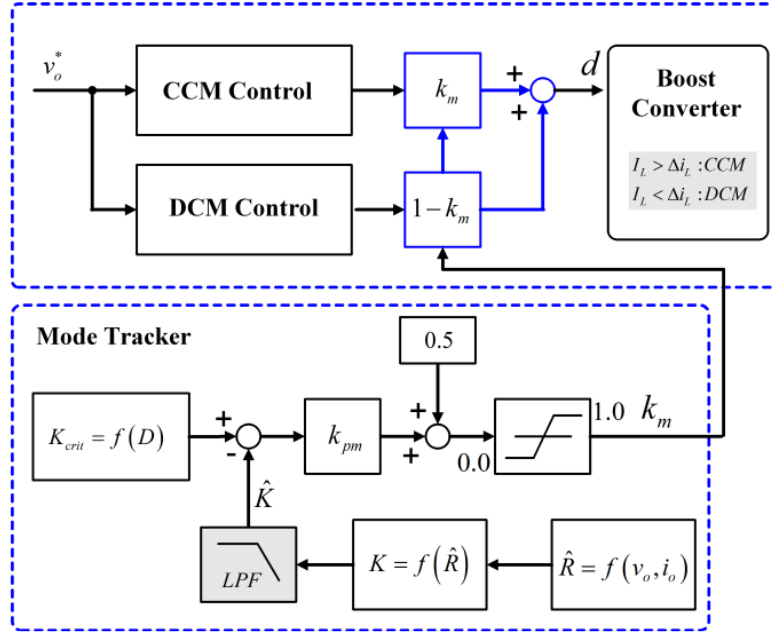


Fig. 24. Simplified control block diagram.

Fig. 24 shows the simplified control block diagram during the mode transition. In Fig. 25, the transient response time during the mode transition from CCM to DCM is within 5ms because the bandwidth of the mixed control loop is about from 100Hz to 1kHz in Fig. 22 and Fig. 23. The transient response during the mode transition is related to two factors. One is k_m and the other is the bandwidth of the LPF of the mode tracker. In the individual controller design, we suppose that k_m is equal to 1 or 0. Therefore, the designed controller's bandwidth is high. In the critical boundary condition, k_m is reduced and it affects to the overall bandwidth. In addition, in order to reduce continuous fluctuations near the critical boundary condition, the LPF is used in the mode tracker. The designed bandwidth of LPF is about 50Hz. Finally, during transient conditions, the controller response will be affected by the two factors and results in slow response.

3.3 Simulation Results

Simulations and tests were carried out to verify the proposed control method. The system parameters and ratings are listed in Table I.

TABLE I
Ratings and Known Parameters of Boost Converter and Control System

Ratings and Parameters	Value	Unit
Rated power	20	W
Output voltage	12	V
Input voltage	6	V
Inductance	15	μH
Capacitance	400	μF
Critical Resistance	25	Ω
Switching Frequency	100	kHz
Sampling Frequency	10	kHz

Fig. 25 shows the simulation waveform of the transient response of the converter with load transitions from $10\ \Omega$ (CCM) to $25\ \Omega$ (Critical boundary condition) and from $25\ \Omega$ to $15\ \Omega$. During the load transition, the transient response time of the output voltage is about 5ms ~ 10ms. k_m changes from 1.0 to 0.5 and from 0.5 to 1.0. It shows an approximate settling time of 10ms. Fig. 26 shows the simulation waveform of the transient response of the converter with load transitions from $10\ \Omega$ (CCM) to $100\ \Omega$ (DCM) and from $100\ \Omega$ to $10\ \Omega$. During the load transition, the transient response time of the output voltage is about 5ms ~ 10ms. k_m is changed from 1.0 to 0.0 and from 0.0 to 1.0. Operation modes can be changed smoothly within 5ms. And the real inductor current, i_L , is shown in Fig. 25 and Fig. 26.

Fig. 27 shows the simulation waveform of the transient response with a load transition from $10\ \Omega$ to $12.5\ \Omega$. The load is decreased step by step incrementally. During load variations, voltage ripples are between 12.1V and 11.6V.

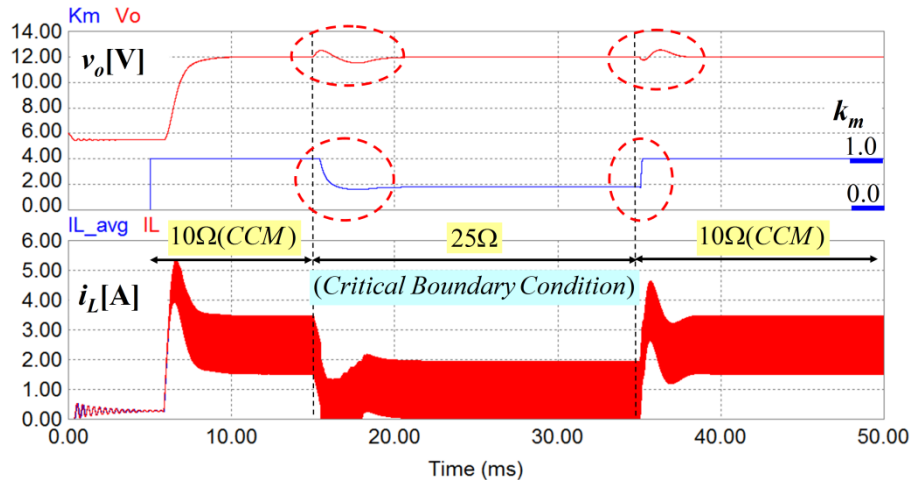


Fig. 25. Simulation waveform of transient response ($10\Omega \rightarrow 25\Omega \rightarrow 10\Omega$).

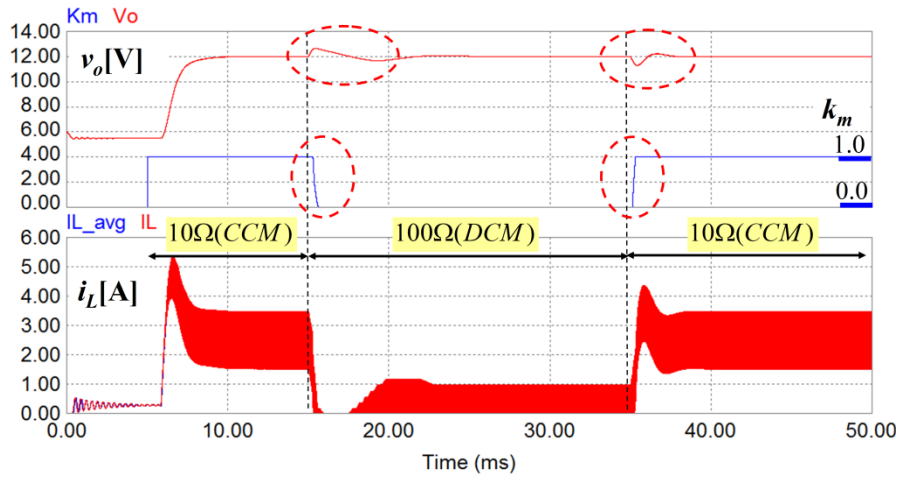


Fig. 26. Simulation waveform of transient response ($10\Omega \rightarrow 100\Omega \rightarrow 10\Omega$).

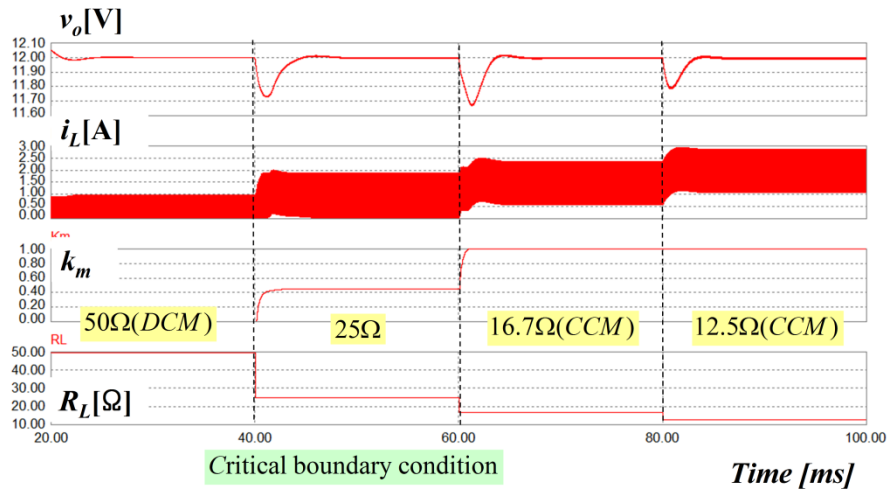


Fig. 27. Simulation waveform of transient response ($50\Omega \rightarrow 25\Omega \rightarrow 16.7\Omega \rightarrow 12.5\Omega$).

3.4 Experimental Results

Fig. 28 shows direct borohydride fuel cell (DBFC) and boost converter system. It consists of two pumps, two fuel bottles, the DBFC stack, and the boost converter with supercapacitors. The supercapacitors are intended to improve the response time in the case of using the DBFC as a power source [26]. The algorithms for the overall operation are implemented with a TI DSP (TMS320F28035). The monitored states are the inductor current, output voltage, and k_m . In order to observe current clearly, a feedback current, i_{L_AD} , which is the sampling current, is monitored because the inductor current has switching ripple.

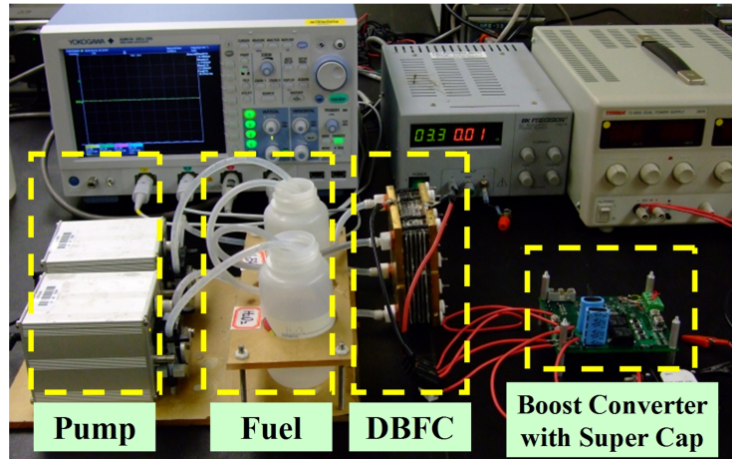


Fig. 28. DBFC and boost converter system.

Fig. 29 shows test waveforms of the transient response during the load change ($25 \Omega \leftrightarrow 10 \Omega$) with the proposed mixed control. The reference voltage is 12V. The fuel cell input voltage is 6V~8V. The recovery time for the output voltage regulation is about 5ms and the under shoot voltage is -0.5V. Two test waveforms show that the proposed control can make transitions between CCM and the critical boundary condition smoothly. In addition, these test results are close to the simulation results. It is clear that the proposed control method is verified by simulations and tests.

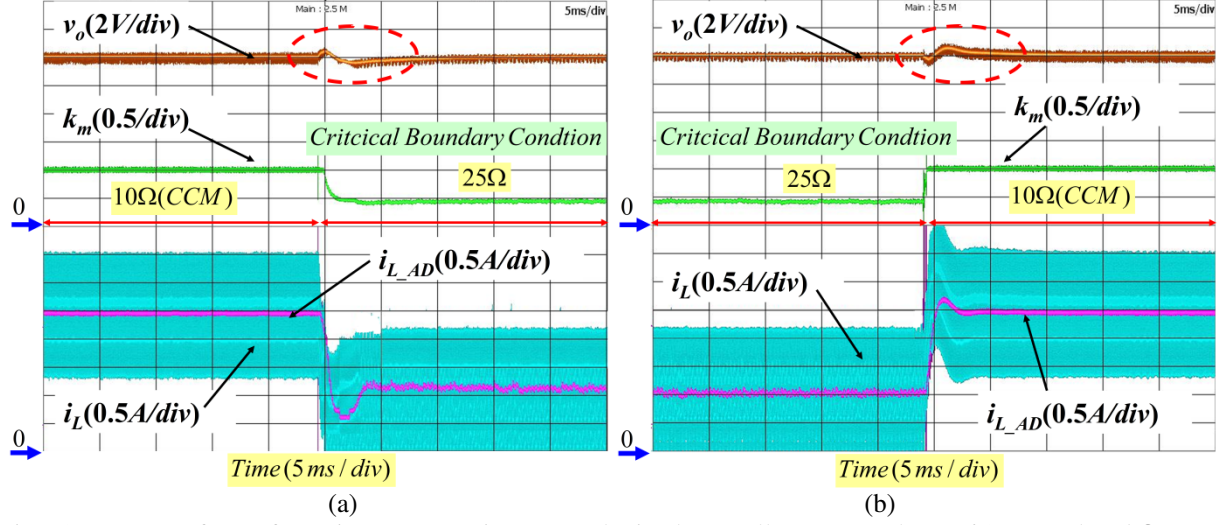


Fig. 29. Test waveform of transient response in proposed mixed controller (Input voltage: 6.0V, Load : 25 Ω \leftrightarrow 10 Ω). (a) 10 Ω \rightarrow 25 Ω . (b) 25 Ω \rightarrow 10 Ω .

In order to show results more clearly, tests are carried out for different input voltages. A bench power as input source is used. The input voltage is 4.5V. To compare the proposed mixed mode controller and single mode controllers, the current mode and voltage mode controller are used.

Fig. 30 (a) shows test waveform under load variation from 40 Ω to 10 Ω in current mode control. The recovery time for the output voltage regulation is about 30ms and the over or under shoot voltage is -1.0V. Fig. 30 (b) shows the test waveform under load variation from 40 Ω to 10 Ω in voltage mode control. The recovery time for the output voltage regulation is 5ms~10ms and the under shoot voltage is less than -0.8V. Fig. 30 (c) shows test waveform under load variation from 40 Ω to 10 Ω with the proposed mixed control. The recovery time for the output voltage regulation is about 5ms and the over or under shoot voltage is less than -0.5V. Therefore, in this condition, the proposed mixed controller is faster than the voltage and current mode controllers.

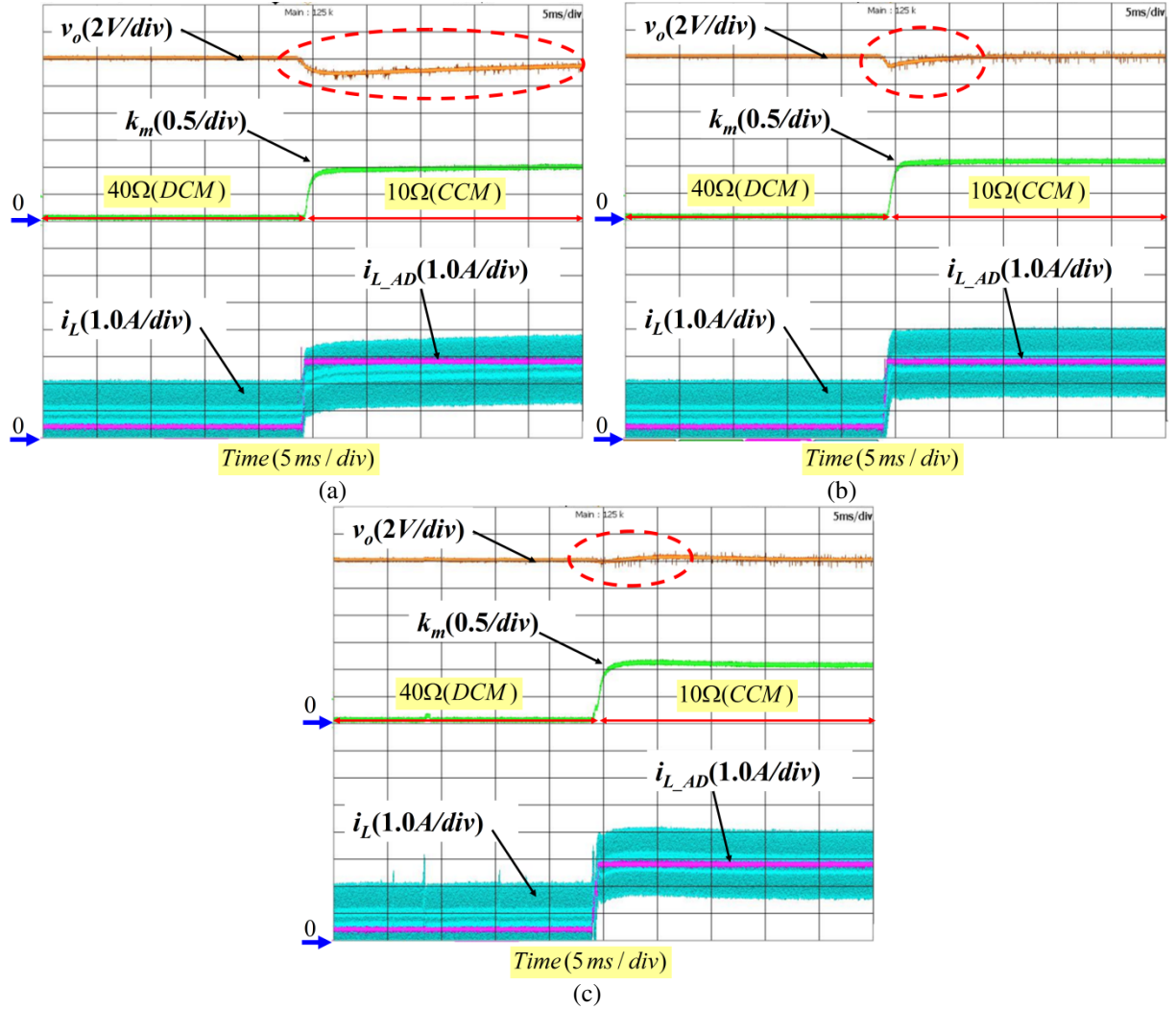


Fig. 30. Test waveform of transient response (Input voltage: $4.5V$, Load: $40\Omega \rightarrow 10\Omega$). (a) Current mode controller, (b) Voltage mode controller, and (c) Proposed mixed controller.

Additional tests are performed to verify severe load transient conditions. The DCM condition is close to no load. Fig. 31 (a) shows test waveforms under load variation from 10Ω to 120Ω in the current mode control. Fig. 31 (b) shows test waveforms under load variation from 10Ω to 120Ω in the voltage mode control. Both controllers are unstable during mode transitions. Fig. 31 (c) shows test waveforms under load variation from 10Ω to 120Ω in the proposed mixed control. The recovery time for the output voltage regulation is $5ms \sim 10ms$ and the under shoot voltage is less than $-0.5V$. The proposed mixed controller has similar performance in comparison to previous test results. Therefore, the single mode controller will be

unstable under these operating conditions. However, the proposed mixed controller has a wide range operation without instability.

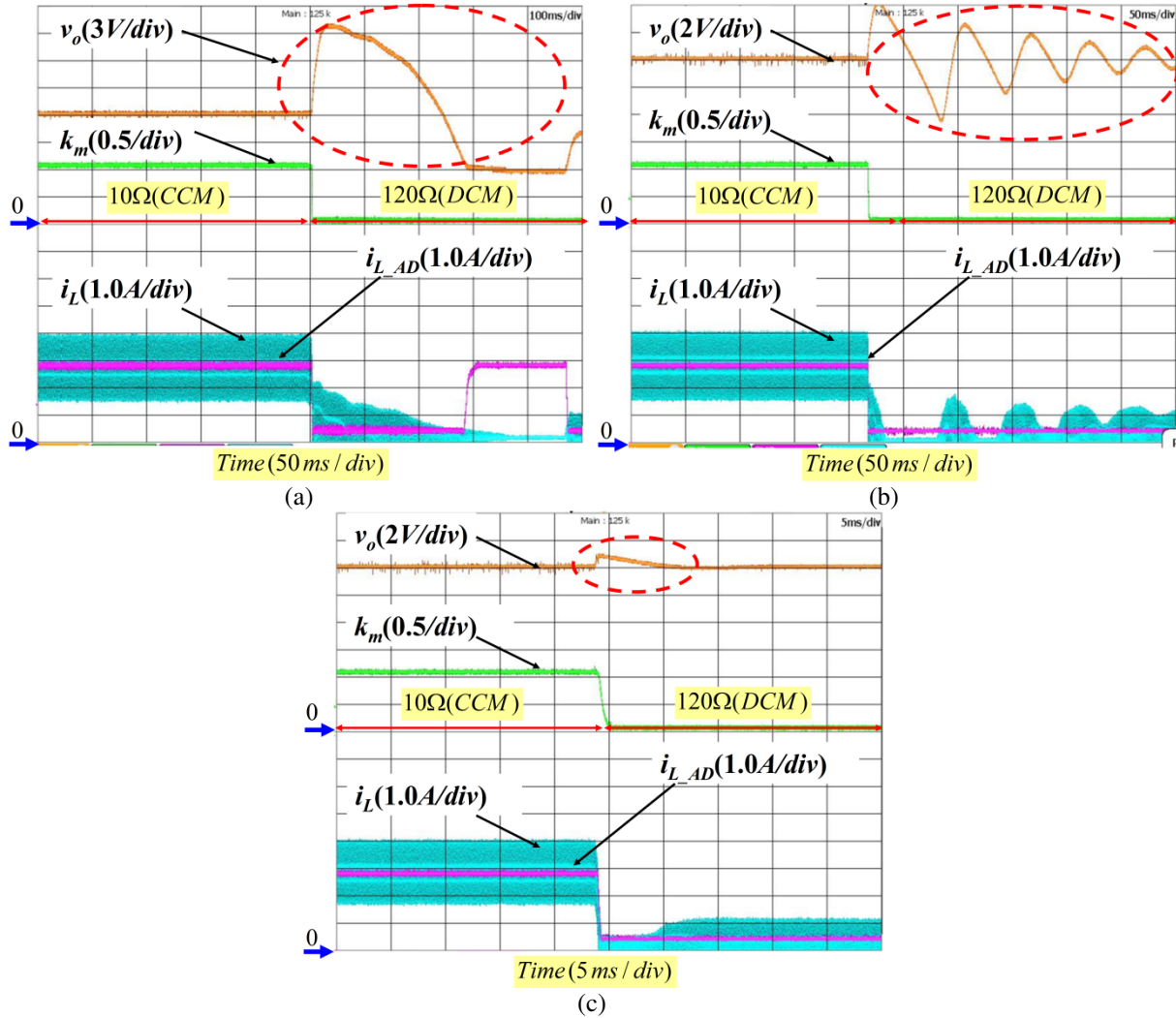


Fig. 31. Test waveform of transient response (Input voltage: 4.5V, Load: $10\Omega \rightarrow 120\Omega$). (a) Current mode controller, (b) Voltage mode controller, and (c) Proposed mixed controller.

3.5 Conclusion

In this chapter, a proposed seamless control scheme was proposed for the boost converter with wide range stable operation in both CCM and DCM. The proposed controller was designed to improve the stability and response time with CCM, DCM, and mode transition conditions. By adding the mode tracker, the proposed control scheme proved smooth transitions between operation modes without chattering near the critical boundary condition. Simulation and test results were well matched. The proposed control

scheme will be very useful in the fuel cell portable application, which is required to operate for widely variable input voltage conditions. In addition, the smooth and wide operation will also benefit to the reliability of the fuel cell stack. Furthermore, the proposed principle will be applicable to the other mode transient mechanisms such as grid mode transitions and master and slave mode transitions.

CHAPTER 4. SEAMLESS CONTROL OF DG INVETERS FOR MODE TRANSITIONS UNDER GRID DISTURBANCE

This chapter is to introduce a seamless grid interconnection control strategy for the renewable energy distributed generations (DG)². Based on the performance analysis of the conventional voltage and current control loops, sophisticated control strategies, which can overcome the limited capability of the DG inverter control in mode transition conditions for unknown power plant conditions, are needed in order to protect critical loads and operate the DG inverter without fault trip. The proposed control strategy consists of a current controller and a feedforward voltage controller to minimize the grid overvoltage. The feedforward voltage control loop was added to the d - q -axis current control loop. The proposed control strategy reduces the overvoltage stress of the renewable energy and the critical load under the grid fault or disturbance conditions. In addition, the smooth operation of the inverter will also enhance the stability and reliability of the grid. Real time digital simulator based hardware-in-the-loop experimental results and simulation results showed that DG inverter could achieve seamless mode change under grid overvoltage conditions.

4.1 Impact of DG Inverter in Overvoltage Conditions

4.1.1 Mode transitions of DG inverter in Overvoltage Conditions

Fig. 32 shows the occurrence of the critical load faults during the conventional mode transition in the overvoltage. The disconnection time of the DG inverter from the grid according to voltage deviations of IEEE 1547 standard is 1 second in 110% overvoltage and 0.16 second in 120% overvoltage [115]. Therefore, conventional mode transition from GC mode to SA mode will be acceptable during 10~60 cycles of fundamental frequency.

² Most of the results presented in this chapter have been published in [138], and [139].

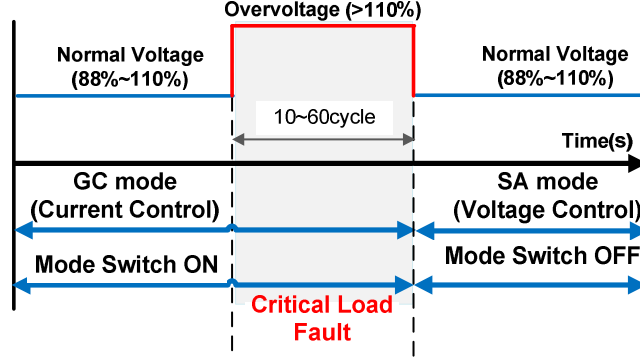


Fig. 32. Occurrence of the critical load faults during conventional mode transition in the overvoltage.

However, since the critical load will encounter overvoltage fault due to the grid overvoltage within 1 or 2 cycles, the DG inverter needs to switch mode immediately to avoid the critical load fault. The grid overvoltage results from two conditions: one is when the grid point common coupling (PCC) switch is turned off, and the other is when the grid voltage is swelling.

4.1.2 Mode transition in the overvoltage condition due to PCC switch-off

Since the DG inverter cannot recognize whether the PCC switch is turned off or not, the PCC switch can be turned off before the mode switch is turned off when the main grid is the fault condition. At this point, the DG inverter continues with current control as in GC mode. Then, the output voltage condition of the DG inverter will experience the overvoltage depending on the power conditions of the DG inverter and the critical load. The overvoltage at the DG inverter is determined as

$$\text{if } |S_o| > |S_L|, S_g = 0, \text{ then } v_o = v_{Limit} \quad (39)$$

where v_{Limit} is the limited output value of the current controller, S_o is the apparent power of the DG inverter, S_L is the apparent power in the critical load, and S_g is apparent power in the grid.

The output voltage of the DG inverter will reach a limit value given in (39). It can exceed 110% of the normal grid voltage. The DG inverter will be increased up to the saturated output voltage until the mode transition that changes control from GC mode to SA mode. After the mode transition, the DG inverter will regulate the output voltage to the normal level through the voltage controller in the SA mode.

Fig.33 (a) shows the DG inverter power flow under overvoltage due to PCC switch off. Fig.33(b) shows the voltage level with respect to operational mode and control mode in the overvoltage due to PCC switch-off. If the DG inverter can change quickly from GC to SA mode within 1 ~ 2 cycles, then the occurrence of the fault trip in the critical load will be reduced because the critical load experiences less overvoltage.

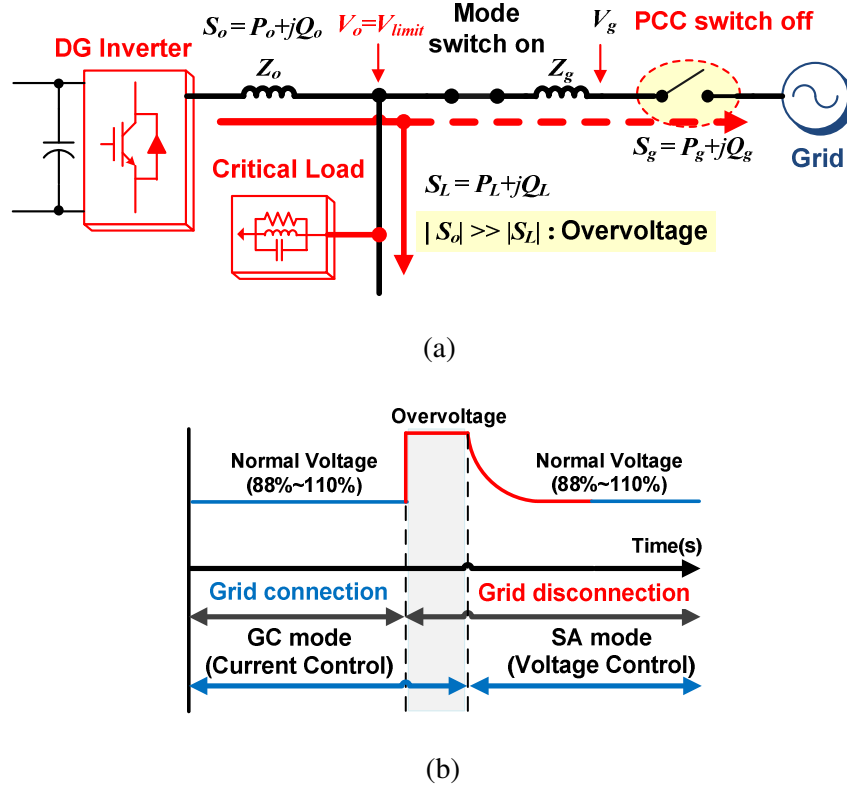


Fig. 33. Overvoltage due to PCC switch-off, (a) DG inverter power flow, (b) voltage level with respect to operational mode and control mode

4.1.3 Mode transition in the overvoltage condition due to grid voltage swell

Fig. 34 (a) shows the DG inverter power flow in the overvoltage due to grid voltage swell. Fig. 34 (b) shows the voltage level with respect to operational mode and control mode in the overvoltage due to grid voltage swell. If the DG inverter performs a fast mode transition within 1 cycle in the overvoltage due to grid voltage swell, the DG inverter fault such as an over-current may occur. Although the DG inverter wants to regulate the output voltage in the grid voltage swell, it is difficult to control the output voltage,

due to the lack of DG inverter capacity compared to the grid. It implies that the fast mode transition in the grid voltage swell with one or two cycles can be failed due to the voltage control instability.

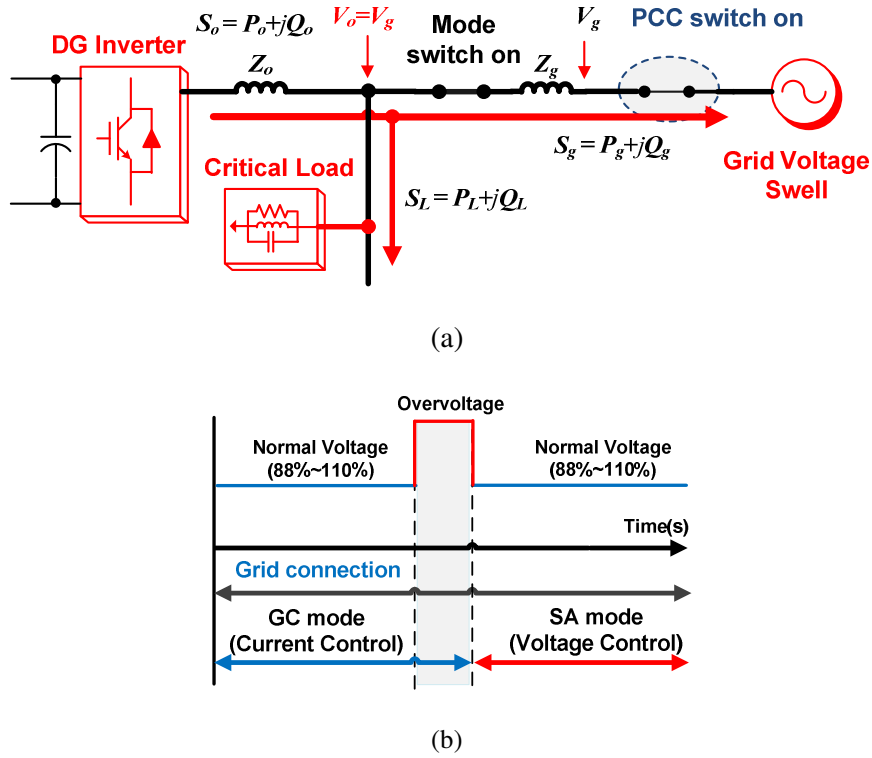


Fig. 34. Overvoltage due to main grid voltage, (a) DG inverter power flow, (b) voltage level with respect to operational mode and control mode

4.1. 4 Requirements for Fast Mode transition of DG inverter in overvoltage conditions

Fig. 35 (a) shows the voltage control in the critical load during fast mode transition in the overvoltage due to PCC switch-off. The response time of the voltage controller depends on the critical load variation. We assume that the minimum and maximum critical loads are 0.5% and 50% of the rated power of the DG. This requires the robust voltage control with one cycle response from 0.5% critical load to 50% critical load. Fig. 35 (b) shows the voltage and current control in the grid during fast mode transition in the overvoltage due to grid voltage swell. The fast mode transition can make unexpected control mode in the overvoltage due to grid voltage swell. The voltage control of DG inverter connected to the grid is not able to regulate the grid voltage. It will cause the voltage control instability in the worst case. Even

though the DG inverter still operates with the voltage control loop in GC mode within short durations, it needs to be changed from voltage control to current control in overvoltage due to grid voltage swell.

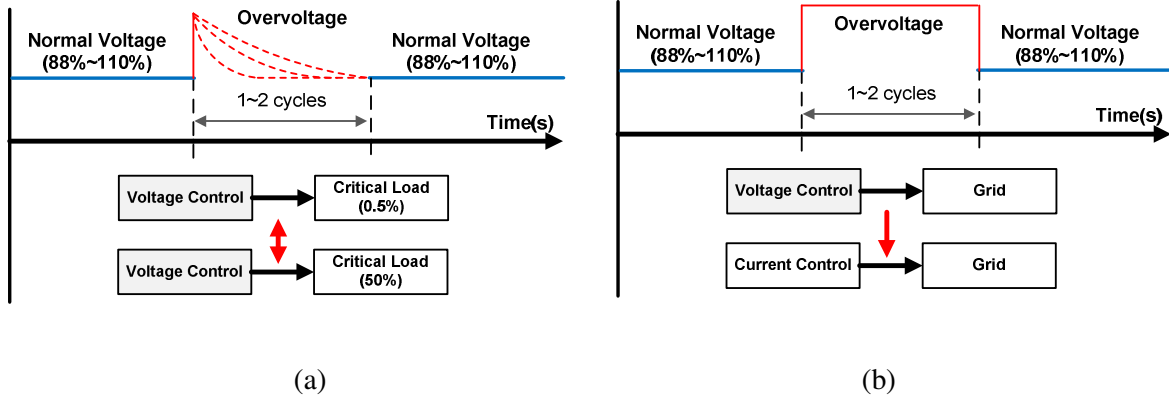


Fig. 35. Control state during fast mode transition (a) overvoltage due to PCC switch-off, (b) overvoltage due to grid voltage swell

Hence, the voltage control needs to have fast response time under the critical load variation to make the fast mode transition in the overvoltage due to PCC switch-off. In addition, the voltage control needs to guarantee the stable operation in the overvoltage due to grid voltage swell. It means that the voltage control is necessary to be designed with considering plants in GC and SA modes. It will satisfy a seamless control of the DG inverter with the critical load safety in overvoltage conditions.

4.2 Conventional DG Inverter Control with Operational Modes

4.2.1 DG inverter Modeling in GC mode and SA mode (Appendix A)

Fig. 36 shows the circuit diagram of the DG inverter with the main grid and the critical load. It consists of the three phase dc-ac inverter, the *LCL* filter, and switches. State variables are defined as below:

\mathbf{v} is the inverter voltage, \mathbf{v}_c is the capacitor voltage of the *LCL* filter, \mathbf{v}_o is the output voltage, \mathbf{v}_g is the grid voltage, \mathbf{i} is the inverter current, \mathbf{i}_c is the capacitor current of the *LCL* filter, \mathbf{i}_o is the output current, \mathbf{i}_r is the resistive load current, \mathbf{i}_l is the inductive load current, and \mathbf{i}_c is the capacitive load current, L_f is the filter inductor, C_f is the filter capacitor, L_g is the grid inductor, R_l is the resistor of the critical load, L_l is the inductor of the critical load, C_l is the capacitor of the critical load, and ω_{res} is the resonance frequency of the *LCL* filter. The rated capacity of the dc-ac inverter is 30kVA. The rated active power of

the DG is 20kW. The rated grid voltage, v_g , is 440VAC line-to-line. The dc-link voltage of dc-ac inverter is 800V. The LCL filter' values are $L_f = L_g = 2mH$ and $C_s = 2\mu F$ [116-118].

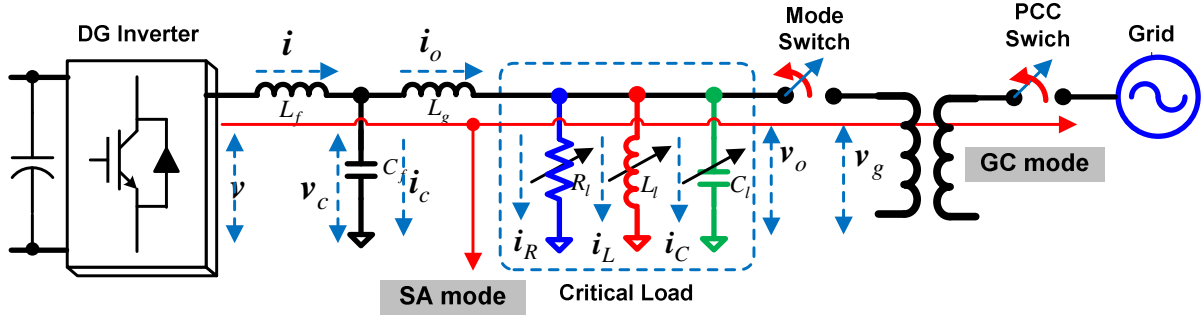


Fig. 36. Circuit diagram of the DG inverter with the grid and the critical load

The following expression is used to transform the abc axis variables to the $\alpha\beta$ axis variables into a complex space vector form:

$$\mathbf{x}_{\alpha\beta} = x_{\alpha} + jx_{\beta} = \frac{2}{3} \left(x_a + x_b e^{j2\pi/3} + x_c e^{j4\pi/3} \right) \quad (40)$$

where, $\mathbf{x}_{\alpha\beta}$ is the complex space vector in the $\alpha\beta$ axis.

To transform the $\alpha\beta$ axis variables to the dq axis variables, the complex space vector form is defined as

$$\mathbf{x}_{dq} = x_d + jx_q = \mathbf{x}_{\alpha\beta} e^{-j\theta} \quad (41)$$

where, \mathbf{x}_{dq} is the complex space vector in the dq axis. $\theta = \omega t$. The d -axis is related to the active power.

The q axis is related to the reactive power.

From Fig.36, complex space vector equations in the dq axis are given as

$$\mathbf{v}_{dq} = L_f \frac{d\mathbf{i}_{dq}}{dt} + j\omega L_f \mathbf{i}_{dq} + \mathbf{v}_{cdq} \quad (42)$$

$$\mathbf{i}_{cdq} = C_f \frac{d\mathbf{v}_{cdq}}{dt} + j\omega C_f \mathbf{v}_{cdq} \quad (43)$$

$$\mathbf{i}_{dq} = \mathbf{i}_{odq} + \mathbf{i}_{cdq} \quad (44)$$

$$\mathbf{v}_{cdq} = L_g \frac{d\mathbf{i}_{odq}}{dt} + j\omega L_g \mathbf{i}_{odq} + \mathbf{v}_{odq} \quad (45)$$

In GC mode, the output voltage is the same as the grid voltage.

$$\mathbf{v}_{odq} = \mathbf{v}_{gdq} \quad (46)$$

In SA mode, the output voltage is determined as

$$\mathbf{v}_{odq} = L_l \frac{d\mathbf{i}_{Ldq}}{dt} + j\omega L_l \mathbf{i}_{Ldq} \quad (47)$$

$$\mathbf{i}_{odq} = \frac{\mathbf{v}_{odq}}{R_l} + C_l \frac{d\mathbf{v}_{odq}}{dt} + j\omega C_l \mathbf{v}_{odq} + \mathbf{i}_{Ldq} \quad (48)$$

From (47) and (48), the complex impedance of the critical load is given as

$$\frac{\mathbf{v}_{odq}}{\mathbf{i}_{odq}} = \mathbf{z}_l(s) = \mathbf{z}_{la}(s) + j\mathbf{z}_{lb}(s) \quad (49)$$

Impedance transfer functions are expressed as

$$\mathbf{z}_{la}(s) = \frac{a_3 s^3 + a_2 s^2 + a_1 s + a_0}{s^4 + c_3 s^3 + c_2 s^2 + c_1 s + c_0} \quad (50)$$

$$\mathbf{z}_{lb}(s) = \frac{b_2 s^2 + b_0}{s^4 + c_3 s^3 + c_2 s^2 + c_1 s + c_0} \quad (51)$$

where

$$\begin{aligned} a_3 &= \frac{1}{C_l}, a_2 = \frac{1}{R_l C_l^2}, a_1 = \frac{\omega^2}{C_l} + \frac{1}{L_l C_l^2}, a_0 = \frac{\omega^2}{R_l C_l^2}, \\ b_2 &= \frac{1}{C_l}, b_0 = \frac{\omega^3}{C_l} - \frac{\omega}{L_l C_l^2}, c_3 = \frac{2}{R_l C_l}, c_2 = 2\omega^2 + \frac{2}{L_l C_l} + \frac{1}{R_l^2 C_l^2}, \\ c_1 &= \frac{2}{R_l C_l} \omega^2 + \frac{2}{R_l L_l C_l^2}, c_0 = \omega^4 - \frac{2}{L_l C_l} \omega^2 + \frac{\omega^2}{R_l^2 C_l^2} + \frac{1}{L_l^2 C_l^2} \end{aligned}$$

Based on (50) - (52), the response time of voltage controllers will be investigated in SA mode. Parameters with respect to power consumption of the critical load are given in Table II.

TABLE II
PARAMETERS WITH RESPECT TO POWER CONSUMPTION OF THE CRITICAL LOAD
(NOMINAL LINE-TO-LINE VOLTAGE: 440VAC, NOMINAL FREQUENCY: 60HZ)

Critical Load Type	$R_l (\Omega)$		$L_l (\text{mH})$		$C_l (\mu\text{F})$	
	Min.	Max.	Min.	Max.	Min.	Max.
Resistive load (R load)	1936 (0.1kW)	19.36 (10kW)	-	-	-	-
Resistive and Inductive loads (RL loads)	1936 (0.1kW)	19.36 (10kW)	102.7 (5kVar)	51.4 (10kVar)	-	-
Resistive and Capacitive loads (RC loads)	1936 (0.1kW)	19.36 (10kW)	-	-	68.507 (5kVar)	137.01 (10kVar)
Resistive, Inductive and Capacitive loads (RLC loads)	1936 (0.1kW)	19.36 (10kW)	102.7 (5kVar)	51.4 (10kVar)	68.507 (5kVar)	137.01 (10kVar)

Fig. 37 shows the transfer function block diagram of the DG inverter in either GC or SA modes based on (42) – (49).

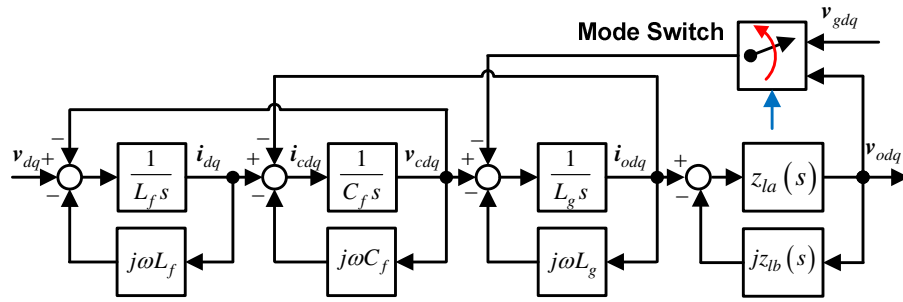


Fig. 37. Transfer function block diagram of the DG inverter.

4.2.2 Current Control in GC mode

Fig. 38 shows the transfer function block diagram of the DG inverter in GC mode. The active damping control to remove a resonance of the *LCL* filter can be added. Therefore, voltage and current controllers of the DG inverter are designed based on the dynamic plant models of the DG inverter with the active damping. The *d-q* axis coupling terms in Fig. 37 can be removed through feedforward methods. The output current feedforward method in Fig. 38 will minimize the impact of grid impedance [118-120].

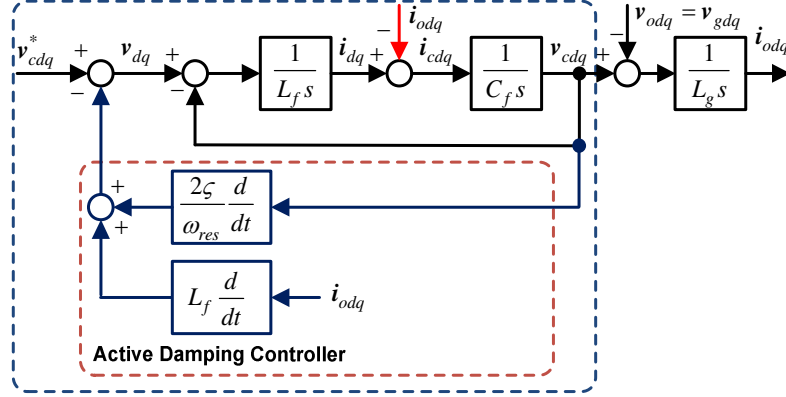


Fig. 38. Transfer function block diagram of DG inverter in GC mode

The LCL filter can be expressed as a second order system because it is damped by an additional compensator. In Fig. 38, the v_{cdq}^* - to- v_{cdq} transfer function, which is equivalent active damping *LCL* filter, is given as

$$G_f(s) = \frac{v_{cdq}}{v_{cdq}^*} = \frac{\omega_{LC}^2}{s^2 + 2\zeta\omega_{LC}s + \omega_{LC}^2} \quad (52)$$

where $\omega_{LC} = \frac{1}{\sqrt{L_f C_f}}$, $\varsigma = 0.707$.

Fig. 39 shows the transfer function block diagram in SA mode. The decoupling impedance, $z_{lb}(s)$, will be ignored because it is regarded as a disturbance term.

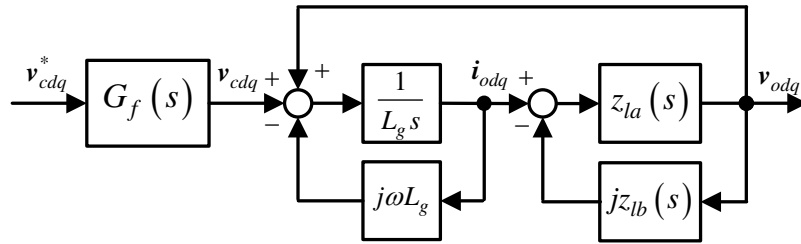


Fig. 39. Transfer function block diagram of DG inverter in SA mode

Fig. 40 shows the current control block diagram in GC mode. The compensator is designed with a PI bncontroller.

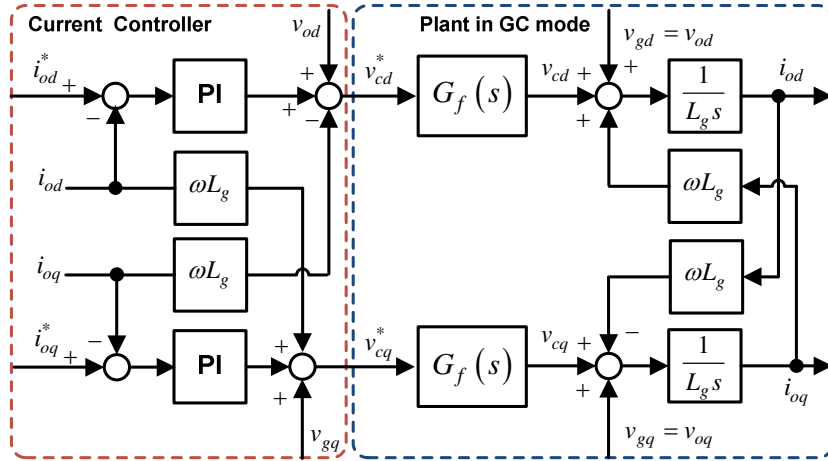


Fig. 40. Current control block diagram in GC mode

4.2.3 Voltage control in SA mode

Fig.41 shows the voltage control block diagram in SA mode. The compensator is designed with a PI controller. In inner loop, the current control can be added. This can be optional. Two voltage controls with / without current loop will have different dynamics.

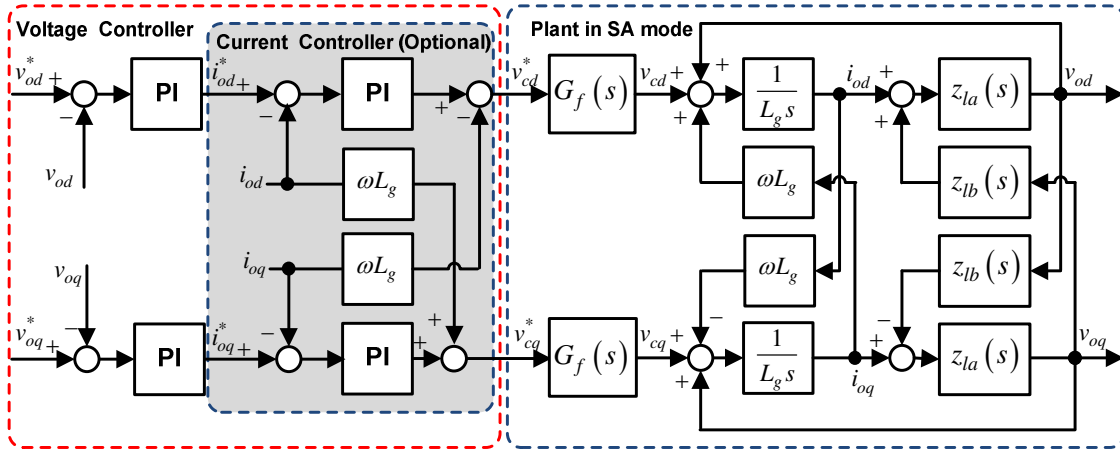


Fig. 41. Voltage control block diagram in SA mode

4.2.4 Performance and Limitation of Voltage Control in the overvoltage conditions

There are a lot of approaches to regulate the ac output voltages of the dc-ac inverter in ac power supplies or uninterruptible power supplies. The ac output terminal of the dc-ac inverter can be connected to an *LCL* filter to reduce switching harmonics. It can be implemented by the current control method, in which inner loop is used by current controller for over-current protection and outer loop is used by

voltage controller. However, this method has the limitation in the response time of the voltage regulation under variable and distorting loads.

The voltage controller has to provide the fast regulation of the output voltage during overvoltage condition due to PCC switch-off. If the overvoltage occurs by the grid swell with one cycle, the voltage control should be stable in the grid connection. The DG inverter will go back to original GC mode after recognizing the overvoltage due to grid voltage swell. Therefore, it is important to design the voltage control with fast regulation and stable operation in the overvoltage conditions. It means that the voltage control needs to consider two operational modes. Here, we will compare the voltage control method with the current loop and without the current loop in terms of response time in SA mode and stability in GC mode.

Fig. 42 shows the simplified voltage control loop with current loop in SA mode. The compensator is designed with a PI controller. In the inner loop, the current loop has variable parameters with respect to the critical load impedance, $z_{la}(s)$. Therefore, the dynamic response will be different according to $z_{la}(s)$. Moreover, it will affect to the dynamic response of voltage loop. At the light load condition, the current will be decreased. Then, it will be more difficult to regulate the output voltage. In the worst case, this controller will be worst to regulate in no load condition.

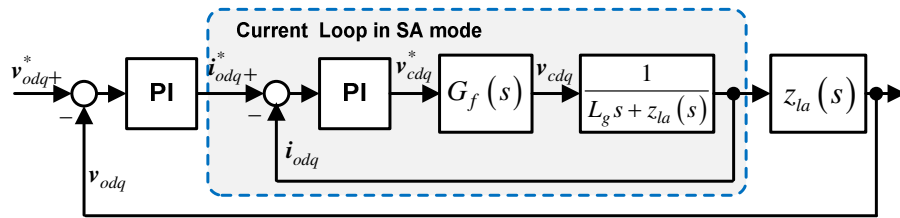
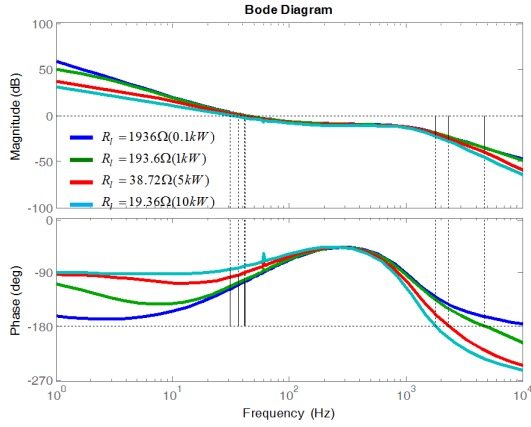


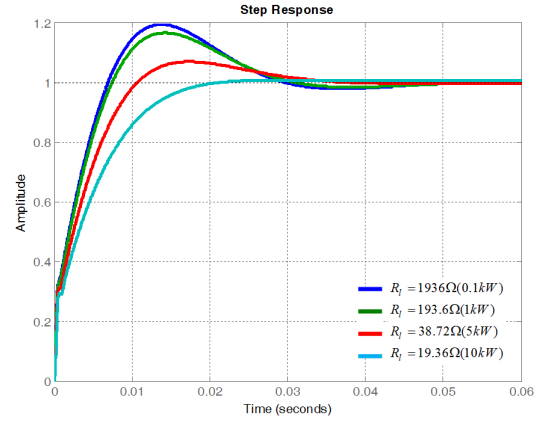
Fig. 42. Simplified voltage control loop with current loop in SA mode.

Fig. 43 shows responses of the voltage control with current loop according to the critical load type in Table I. Fig 43 (a) shows frequency responses of open loop gain according to the resistive load. Fig. 43 (b) shows step responses of the voltage control with current loop with the resistive load. In cases of resistive, inductive, and capacitive loads, frequency and step responses are shown in Fig. 43 (c) and (d), respectively. There is no instability according to the critical load type. However, the response time of the

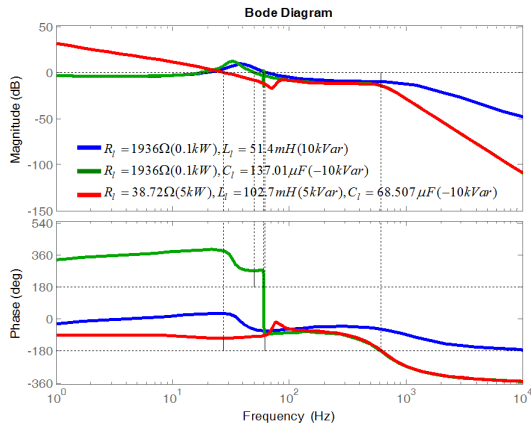
current controller varies with respect to the resistive load. Hence, it is difficult to achieve the voltage regulation with no overshoot in very light resistive load condition because of the inner current loop response is sensitive to the resistive load. Finally, the overshoot will make additional overvoltage. On the other hand, if this controller is operated in the overvoltage due to grid voltage swell, then the DG inverter operation will be stable because the output current flow can be limited.



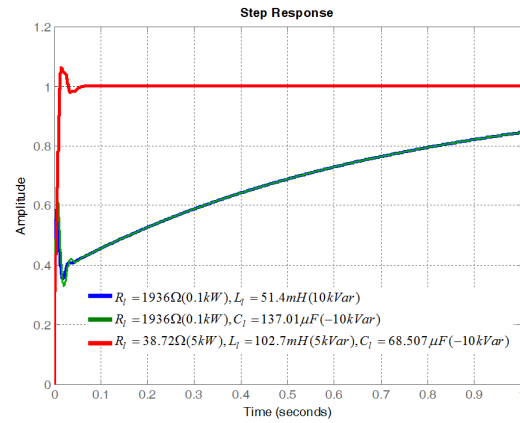
(a)



(b)



(c)



(d)

Fig. 43. Responses of the voltage control with current loop according to the critical load type. (a) frequency responses of open loop gain (R load), (b) step responses (R load), (c) frequency responses of open loop gain (RL, RC, RLC loads), (d) step responses (RL, RC, RLC loads).

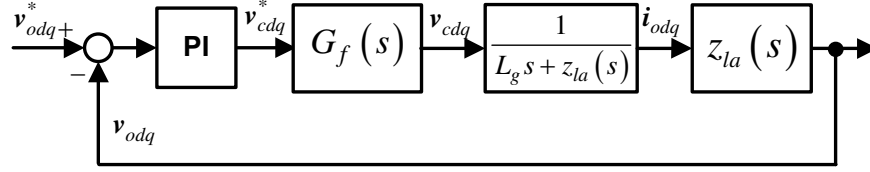
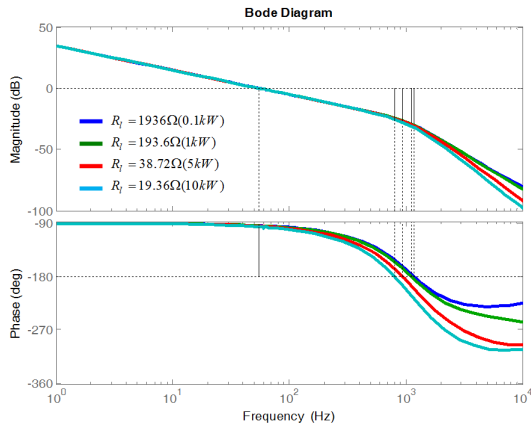
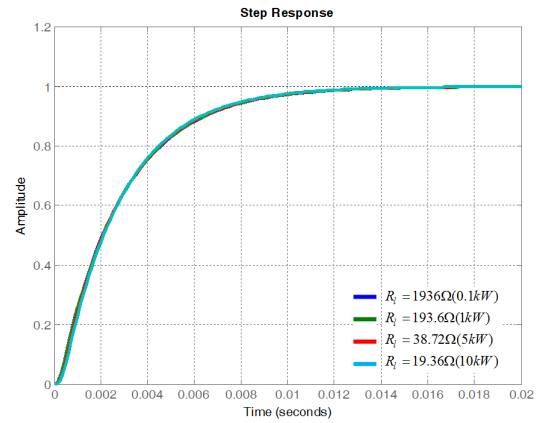


Fig. 44. Simplified voltage control loop without the current control loop in SA mode.

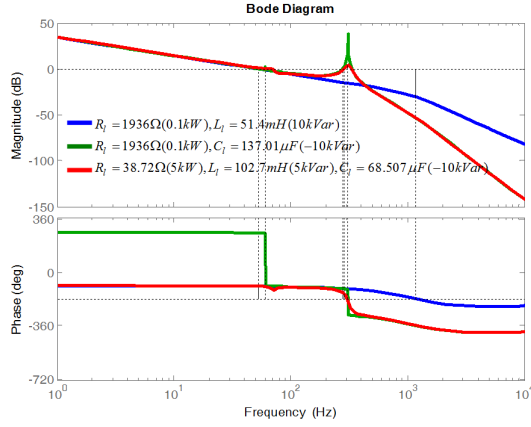
Fig. 44 shows the simplified voltage control loop without current loop in SA mode. The compensator is designed with a PI controller. The voltage loop response varies with respect to the critical load impedance, $z_{la}(s)$. Fig. 45 shows responses of the voltage control with current loop according to the critical load type in Table I. Fig. 45 (a) shows the frequency response of the open loop gain in the resistive load. Fig. 45 (b) shows the step response of the voltage loop with resistive load. In cases of resistive, inductive, and capacitive loads, frequency and step responses are shown in Fig.45 (c) and (d), respectively. Responses of the voltage control without current loop shown in Fig. 43 are fixed with respect to the resistive load. It implies that the voltage control without current loop is robust under the resistive load variation. However, it can be unstable under either inductive or capacitive loads because there exists some resonance points shown in Fig. 45 (c). Moreover, in the overvoltage due to the grid voltage swell, it will make uncontrolled current flow, because there is no inner current loop.



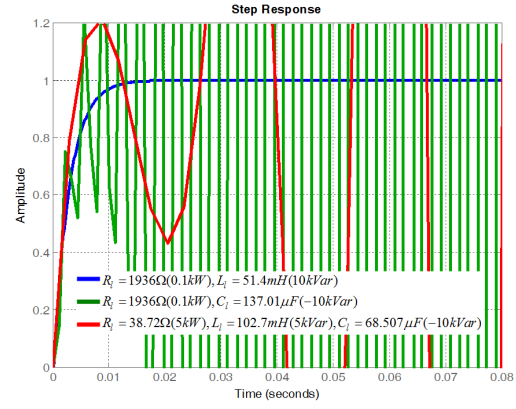
(a)



(b)



(c)



(d)

Fig. 45. Responses of the voltage control without current loop according to the critical load type. (a) frequency responses of open loop gain (R load), (b) step responses (R load), (c) frequency responses of open loop gain (RL, RC, and RLC loads), and (d) step responses (RL, RC, and RLC loads).

4.3 Seamless Control Strategy in Overvoltage Conditions

4.3.1 Proposed controller configuration

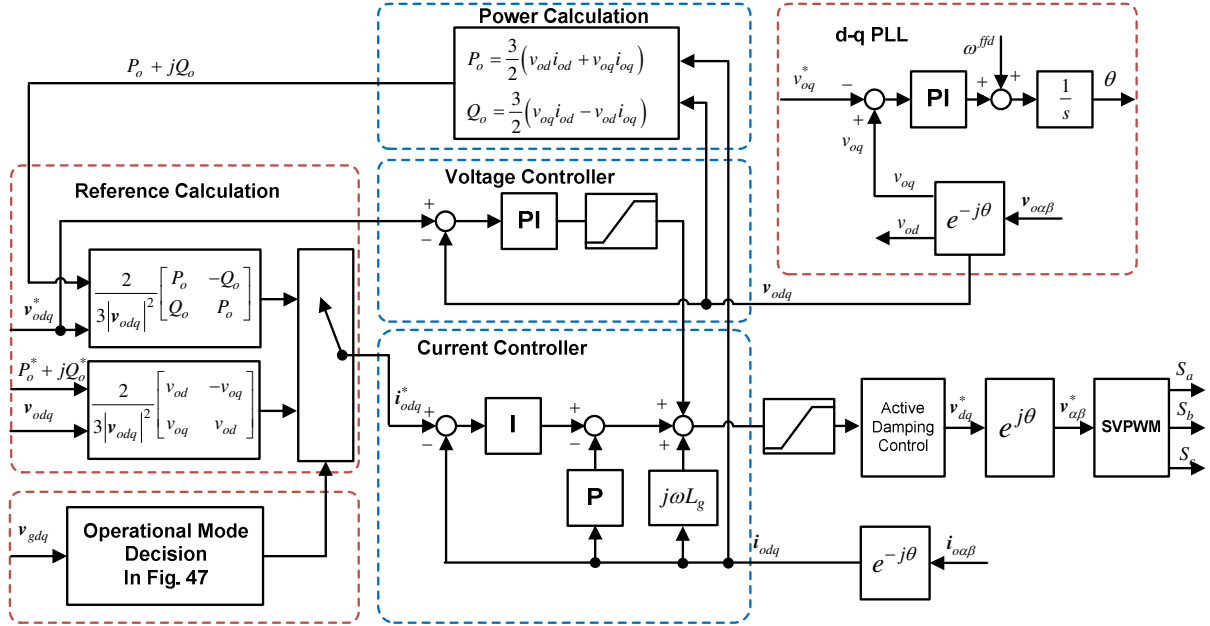


Fig. 46. Proposed overall control block diagram.

Fig. 46 shows the proposed overall control block diagram. It is designed based on the synchronous reference frame, which means the d - q axis. The active power is controlled in the d -axis. And the reactive power is controlled in the q -axis. In GC mode, the current control with the current reference calculation from active and reactive power references is selected by the operational mode decision under the overvoltage conditions. In SA mode, the current controller is connected by the current reference calculation with the d - q axis voltage references. The current reference calculation will be explained in (16)-(19). In addition, a feedforward voltage control is added in the d - q axis current control. Therefore, the proposed feedforward voltage controller in the d - q axis can help the fast voltage regulation in SA mode. The angle control detects the grid angle by regulating the d -axis voltage.

4.3.2 Current Reference Calculation with respect to Operational Modes

The output power of the DG inverter is given as

$$P_o = \frac{3}{2} (v_{od} i_{od} + v_{oq} i_{oq}) \quad (53)$$

$$Q_o = \frac{3}{2} (v_{oq} i_{od} - v_{od} i_{oq}) \quad (54)$$

where, P_o is the output active power, Q_o is the output reactive power.

From (53) and (54), the d - q axis current references with respect to the active and reactive power reference in GC mode can be derived as

$$\begin{bmatrix} i_{od}^* \\ i_{oq}^* \end{bmatrix} = \frac{2}{3(v_{od}^2 + v_{oq}^2)} \begin{bmatrix} v_{od} & -v_{oq} \\ v_{oq} & v_{od} \end{bmatrix} \begin{bmatrix} P_o^* \\ Q_o^* \end{bmatrix} \quad (55)$$

where, P_o^* is the output active power reference, Q_o^* is the output reactive power reference, i_{od}^* is the d -axis output current reference, i_{oq}^* is the q -axis output current reference.

The d - q -axis current references with respect to the d - q axis output voltage references in SA mode can be derived as

$$\begin{bmatrix} i_{od}^* \\ i_{oq}^* \end{bmatrix} = \frac{2}{3(v_{od}^2 + v_{oq}^2)} \begin{bmatrix} P_o & -Q_o \\ Q_o & P_o \end{bmatrix} \begin{bmatrix} v_{od}^* \\ v_{oq}^* \end{bmatrix} \quad (56)$$

where, v_{od}^* is the d -axis output voltage reference, v_{oq}^* is the q -axis output voltage reference.

Fig. 47 shows a state flow diagram for the operational mode decision in overvoltage conditions. In GC mode, the mode switch is turned on. The current reference with respect to the active and reactive power is determined by (56). In the overvoltage (OV) condition, the mode switch continues to be turned on. The current reference with respect to the active and reactive power is determined by (56). After changing from the current reference in (55) to the current reference in (56), the DG inverter experience two different behaviors of the current loop during OV condition.

If the error value of the current control in Fig. 47 is decreased near to zero, the overvoltage comes from PCC switch-off because the current reference in (56) is matched to the critical load. The DG inverter will change from OV condition to the SA mode in Fig. 47 (a). In the SA mode, the mode switch is turned off. The current reference with respect to the active and reactive power is determined by (56). If the error value of the current control is increased, the output of current control will reach the limited value. In this case, the overvoltage is caused by the grid voltage swell. The DG inverter can return from OV condition to GC mode in Fig. 47(b).

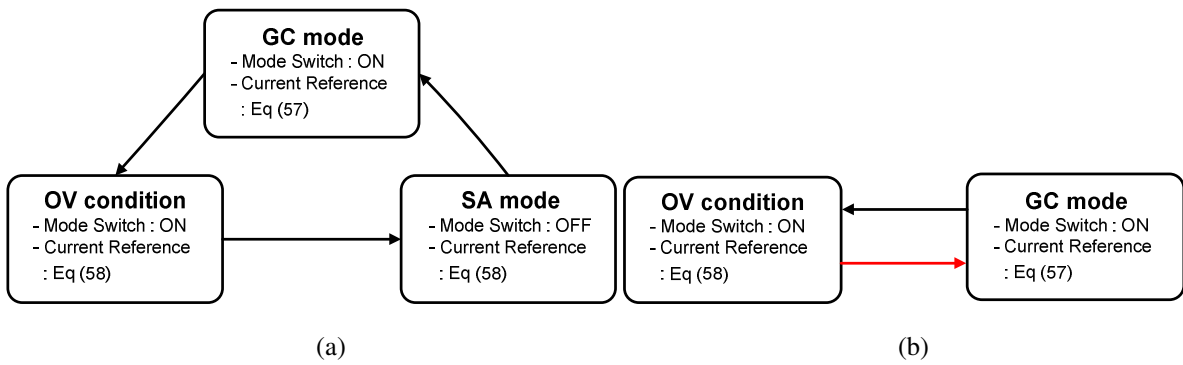


Fig. 47. State flow diagram for operational mode decision in overvoltage conditions, (a) overvoltage due to PCC switch-off, (b) overvoltage due to grid voltage swell.

4.3.3 Current Control with Feed forward Voltage loop

Fig. 48 shows the block diagram of the current control with feedforward voltage loop in SA mode.

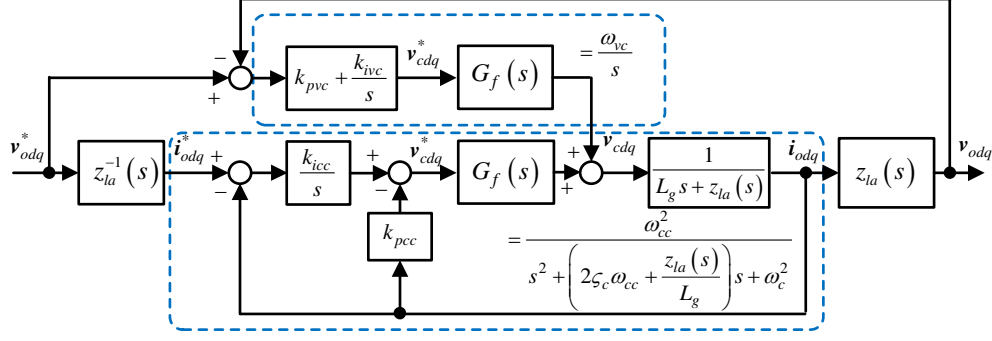


Fig. 48. Block diagram of the simplified current control with feed forward voltage loop in SA mode.

In the current loop, the current reference is calculated as

$$\mathbf{i}_{odq}^* = \mathbf{z}_{la}^{-1}(s) \mathbf{v}_{odq}^* \quad (57)$$

From Fig. 48, the output current can be expressed as

$$\begin{aligned} \mathbf{i}_{odq} = & \frac{\omega_{cc}^2}{s^2 + \left(2\zeta_c \omega_{cc} + \frac{z_{la}(s)}{L_g}\right)s + \omega_c^2} \mathbf{i}_{odq}^* \\ & + \frac{\frac{1}{L_g} s}{s^2 + \left(2\zeta_c \omega_c + \frac{z_{la}(s)}{L_g}\right)s + \omega_{cc}^2} \frac{\omega_{vc}}{s} (\mathbf{v}_{odq}^* - \mathbf{v}_{odq}) \end{aligned} \quad (58)$$

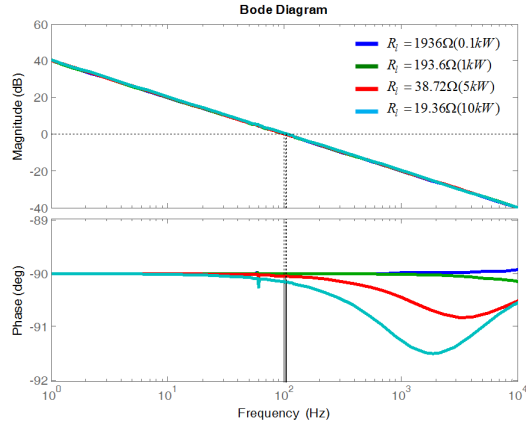
From (58), the closed transfer function in d - q axis can be derived as

$$\frac{\mathbf{v}_{odq}}{\mathbf{v}_{odq}^*} = \frac{\mathbf{i}_{odq}}{\mathbf{i}_{odq}^*} = \frac{\omega_{vc} s + \omega_{cc}^2 + \frac{z_{la}(s)}{L_g} \omega_{vc}}{s^2 + \left(2\zeta_c \omega_c + \frac{z_{la}(s)}{L_g}\right)s + \omega_c^2 + \frac{z_{la}(s)}{L_g} \omega_{vc}} \quad (59)$$

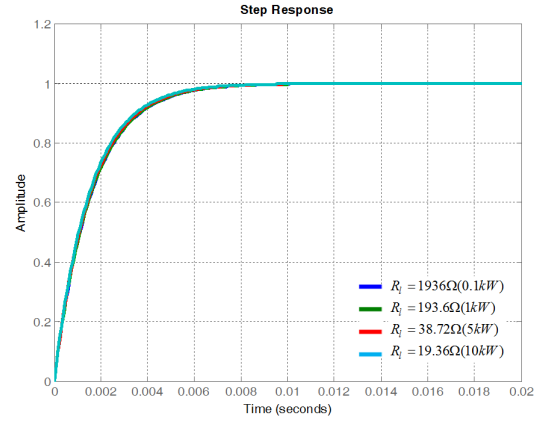
where, $k_{pcc} = 2\zeta_c \omega_{cc} L_g$, $k_{icc} = \omega_{cc}^2 L_g$, $k_{pvc} = \omega_{vc} / \omega_{LC}$, $k_{ivc} = \omega_{vc}$, ω_{cc} is the bandwidth of the current controller, and, ω_{vc} is the bandwidth of the voltage controller.

Fig. 49 shows responses of the current control with feedforward voltage loop according to the critical load type in Table I. Fig. 49 (a) shows the open loop gain's frequency responses of the current control with feedforward voltage loop in the resistive load. Fig. 49 (b) shows the step response of the current control with feedforward voltage loop in the resistive load. Fig. 49 (c) and (d) show the open loop gain's

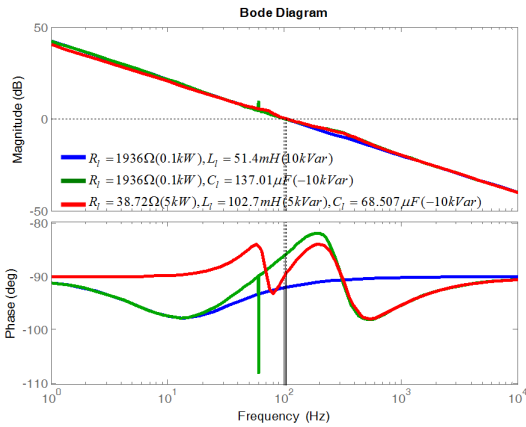
frequency responses and step responses of the current control with feedforward voltage loop in resistive, inductive, and capacitive loads, respectively. Response times of the output voltage are almost constant in regardless with the critical load type. That means that the proposed control scheme is very robust under resistive, inductive, capacitive load variation. Specially, the proposed control is able to regulate in the no load condition because of the feedforward voltage loop.



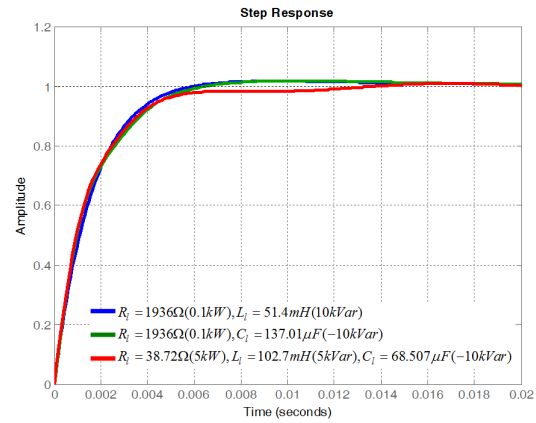
(a)



(b)



(c)



(d)

Fig. 49. Responses of the current control with feedforward voltage loop according to the critical load type. (a) frequency responses of open loop gain (R load), (b) step responses (R load), (c) frequency responses of open loop gain (RL, RC, and RLC loads), and (d) step responses (RL, RC, and RLC loads).

If this control loop is activated in GC mode, the d - q axis current loop is operated with respect to the grid impedance. There is no effect in the q -axis current loop because the q -axis feed forward voltage control is regulated with a zero reference. On the other hand, the d -axis feed forward voltage loop's

output is fixed by the voltage limiter when the d -axis voltage reference is not same to the d -axis grid voltage. Hence, this control scheme is stable in the GC mode.

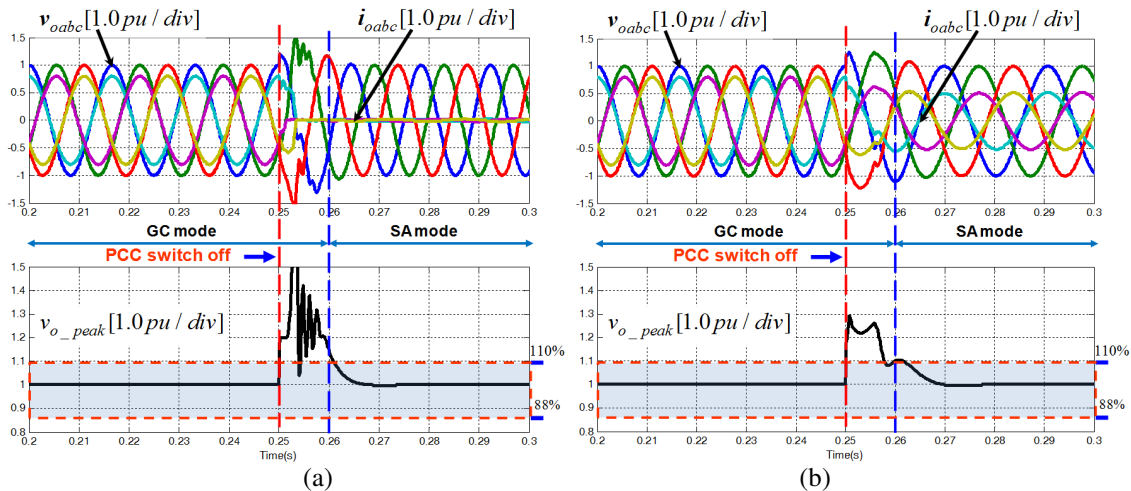
4.4 Simulation Results

The DG inverter needs to consider two cases; one is the overvoltage of the DG inverter resulting from the PCC switch-off, and the other one is the overvoltage due to the grid voltage swell. Based on Table I, we will compare response time of controllers. The critical load condition is given as below:

- 1) Resistive load: $R_l = 1936\Omega(0.1kW)$, and $R_l = 38.72\Omega(5kW)$
- 2) Resistive and inductive loads: $R_l = 1936\Omega(0.1kW)$, $L_l = 51.4mH(10kVar)$
- 3) Resistive and capacitive loads: $R_l = 1936\Omega(0.1kW)$, $C_l = 137.01\mu F(-10kVar)$
- 4) Resistive, inductive and capacitive loads
: $R_l = 38.72\Omega(5kW)$, $L_l = 102.7mH(5kVar)$, $C_l = 68.507\mu F(-10kVar)$

Fig. 50 shows simulation results of the conventional mode transition from the current control to the voltage control without the current loop. The response time of the voltage regulation is within one cycle in the overvoltage due to switch-off period with 0.1kW resistive load shown in Fig. 50 (a) and with 5kW resistive load shown in Fig. 50 (b), 0.1kW resistive and 10kVar inductive loads in Fig. 50 (c). However, it is unstable during the mode transition with 0.1kW resistive, -10kVar capacitive loads in Fig. 50 (d) and 5kW resistive, 5kVar inductive, -10kVar capacitive loads in Fig. 50 (e).

Moreover, the mode transition during grid voltage swells in Fig. 50 (f) shows unstable operation of the DG inverter in terms of uncontrolled current flow.



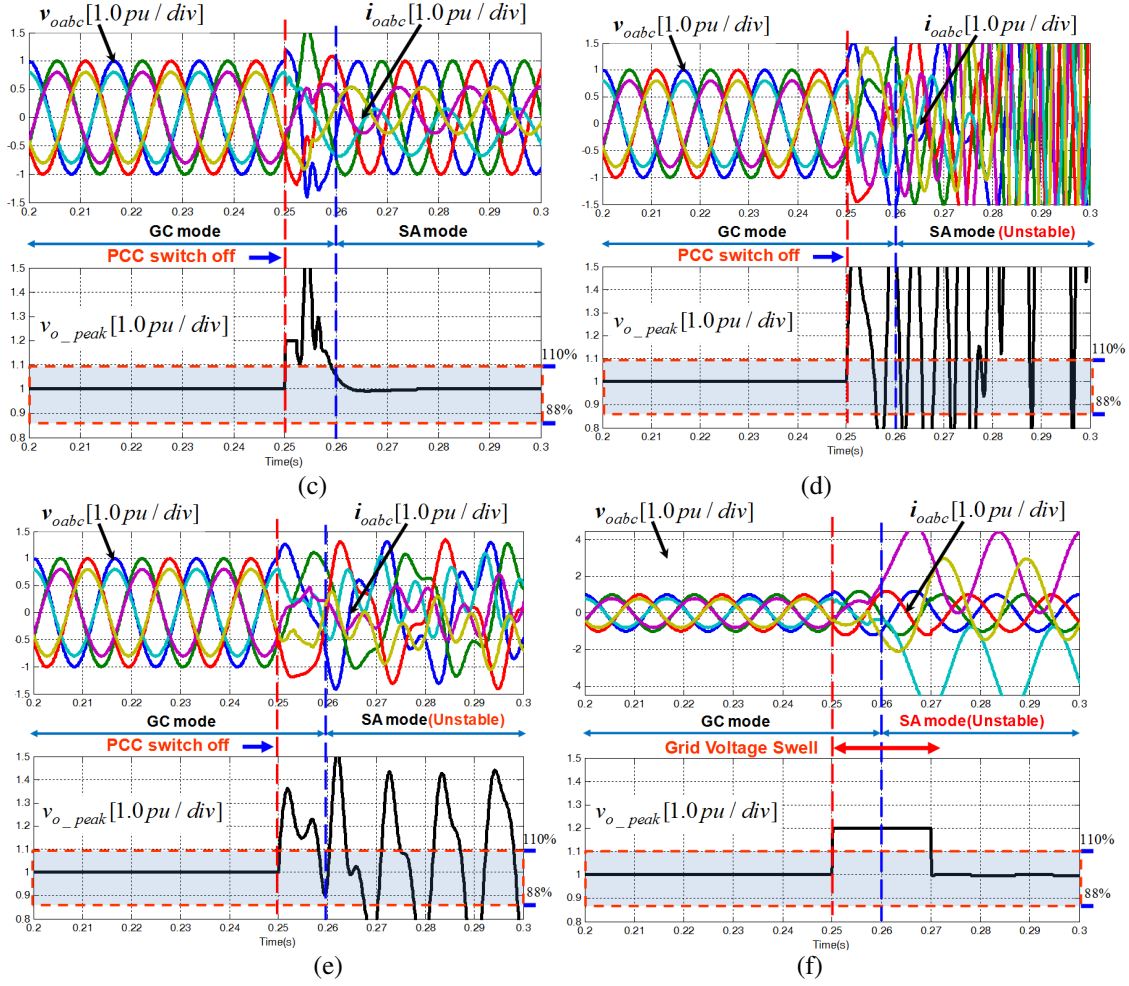


Fig. 50. Simulation results of the conventional mode transition from the current control to the voltage control with the current loop. PCC switch-off period with (a) 0.1kW resistive load, (b) 5kW resistive load, (c) 0.1kW resistive and 10kVar inductive loads, (d) 0.1kW resistive, -10kVar capacitive loads, (e) 5kW resistive, 5kVar inductive, -10kVar capacitive loads, and (f) grid voltage swell.

Fig. 51 shows simulation results of the conventional mode transition from the current control to the voltage control with the current loop. The output voltage is not regulated within one cycle in the overvoltage due to switch-off period with 0.1kW resistive load in Fig. 51 (a), 0.1kW resistive and 10kVar inductive loads in Fig. 51 (c), and 0.1kW resistive, -10kVar capacitive loads in Fig. 51 (e). The mode transition with 5kW resistive load in Fig. 51 (b) and 5kW resistive, 5kVar inductive, -10kVar capacitive loads in Fig. 51 (e) are acceptable. And the mode transition during grid voltage swells in Fig. 51 (f) shows stable DG inverter operation with limited current flow.

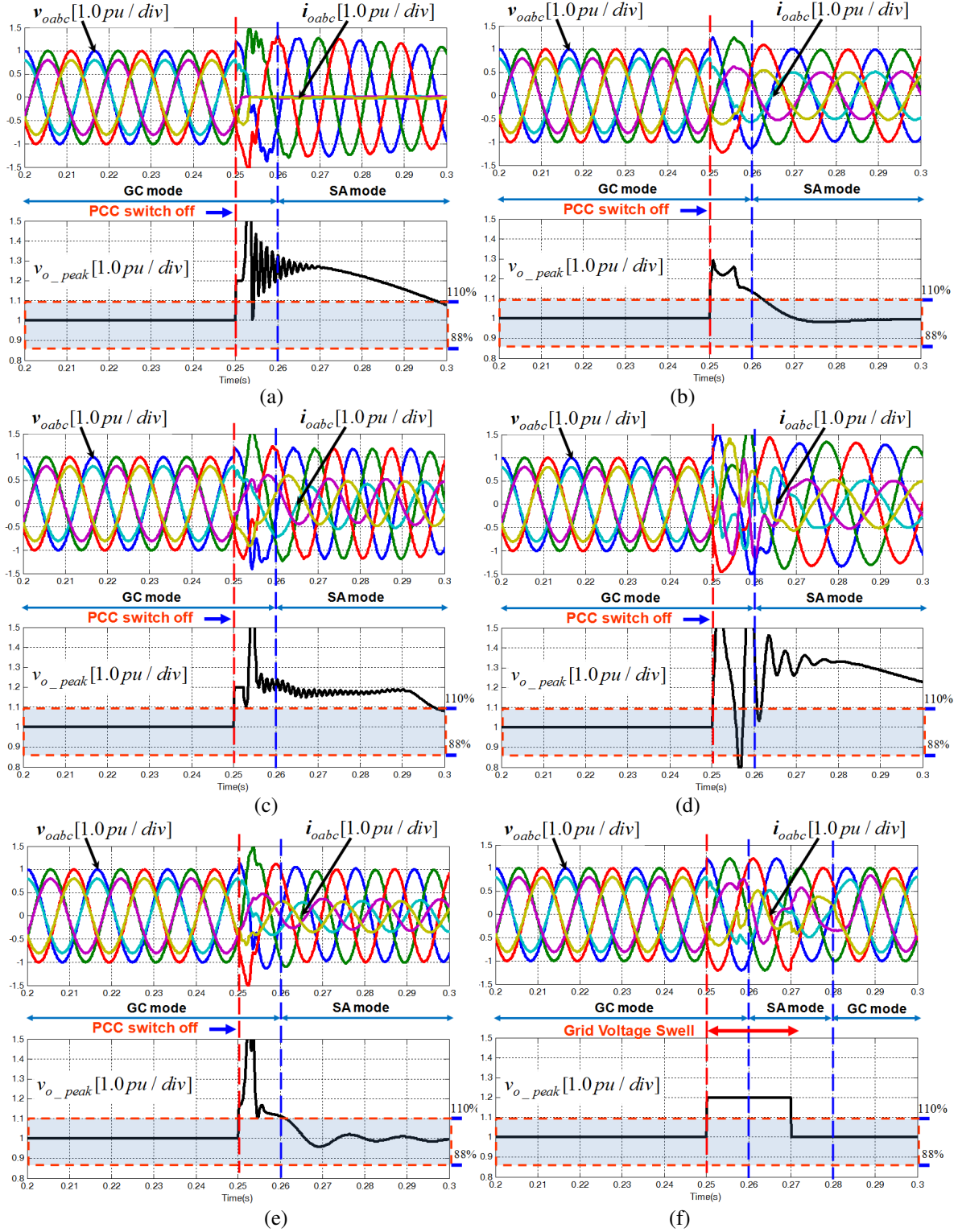


Fig. 51. Simulation results of the conventional mode transition from the current control to the voltage control without the current loop. PCC switch-off period with (a) 0.1kW resistive load, (b) 5kW resistive load, (c) 0.1kW resistive and 10kVar inductive loads, (d) 0.1kW resistive, -10kVar capacitive loads, (e) 5kW resistive, 5kVar inductive, -10kVar capacitive loads, and (f) grid voltage swell.

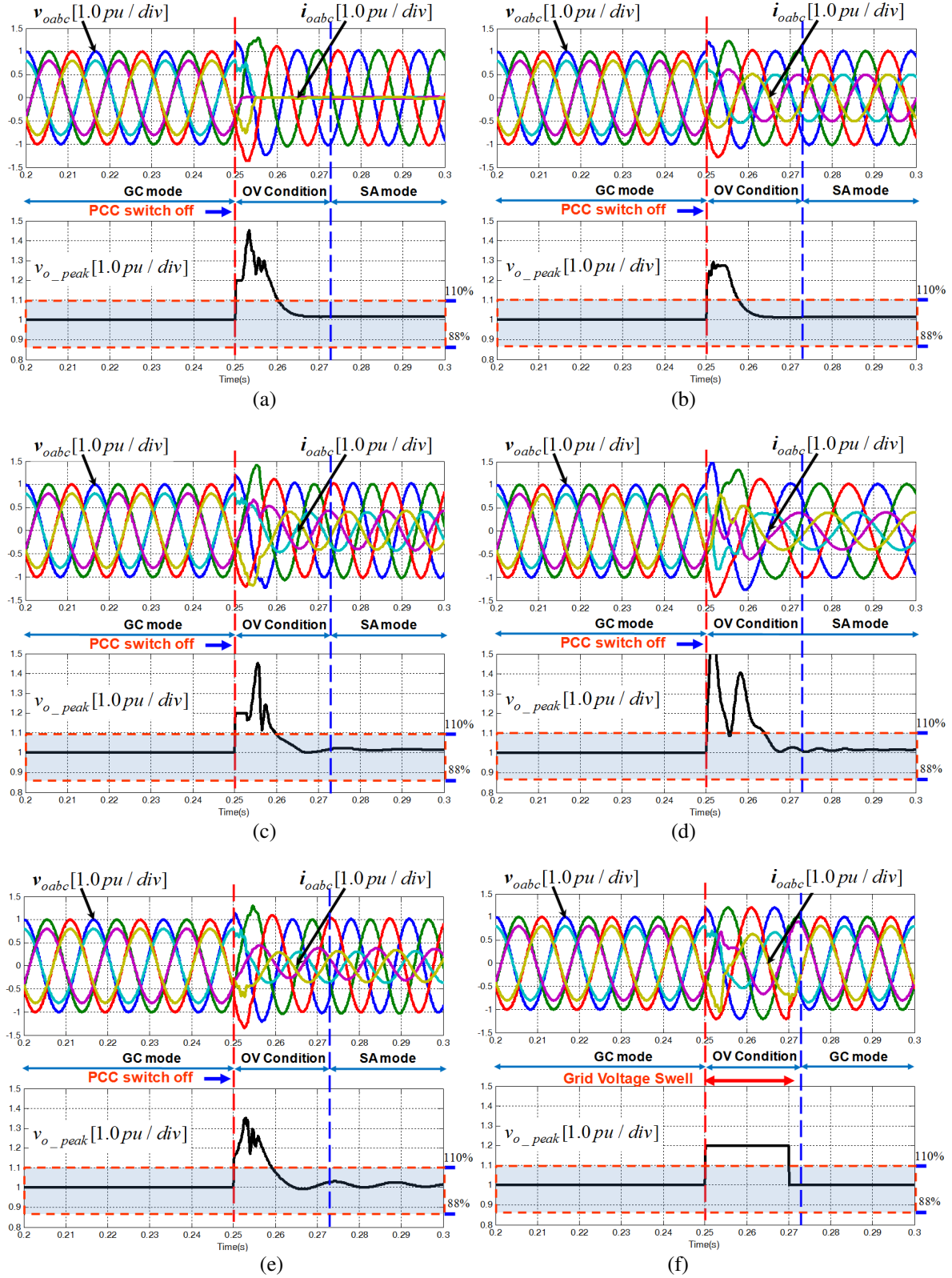


Fig. 52. Simulation results of the proposed mode transition in current control with feedforward voltage loop. PCC switch-off period with (a) 0.1kW resistive load, (b) 5kW resistive load, (c) 0.1kW resistive and 10kVar inductive loads, (d) 0.1kW resistive, -10kVar capacitive loads, (e) 5kW resistive, 5kVar inductive, -10kVar capacitive loads, and (f) grid voltage swell.

Fig. 52 shows simulation results of the proposed mode transition using the current control with feedforward voltage loop. The response time of the voltage regulation is within one cycle in the overvoltage due to switch-off period with all critical loads in Fig. 52 (a), (b), (c), (d), and (e). Moreover, the mode transition during grid voltage swells in Fig. 52 (f) shows stable DG inverter operation with limited current flow.

TABLE III
COMPARISON OF CONTROLLERS PERFORMANCE FOR MODE TRANSITION

Control Scheme	SA mode					GC mode
	R load 1936Ω(0.1kW)	R load 19.36Ω(10kW)	RL loads 1936Ω(0.1kW) 51.4mH(10kVar)	RC loads 1936Ω(0.1kW) 137.01μF(-10kVar)	RLC loads 38.72Ω(5kW) 51.4mH(10kVar) 137.01μF(-10kVar)	
Voltage control without current loop	Fast response	Fast response	Fast response	Unstable	Unstable	Unstable
Voltage control with current loop	Slow response	Fast response	Slow response	Slow response	Fast response	Stable
Current control with feedforward voltage loop	Fast response	Fast response	Fast response	Fast response	Fast response	Stable

Table III shows the comparison of controller's performance for operational mode transition based on the simulation results. The voltage control without current loop can achieve a fast response time with either resistive load or inductive load. However, it is unstable during the mode transition due to switch-off period with capacitive load, and the mode transition during grid voltage swells in GC mode because of no current limitation. On the other hand, the voltage control with current loop is stable during the mode transition due to switch-off period with capacitive load, and the mode transition during grid voltage swells in GC mode. However, it is difficult to achieve fast voltage regulation with one cycle in light resistive load. The proposed current control with feedforward voltage loop is not only a robust under the resistive, inductive, and coactive loads in terms of fast response time of voltage regulation but also stable in

unexpected mode transition in the overvoltage due to the grid voltage swell. As a result, the mode transition using the proposed current control with feedforward voltage loop can minimize the overvoltage during the PCC switch-off period and it can perform ride through without the DG inverter trip in the overvoltage due to the grid voltage swell.

4.5 Experimental Results

4.5.1 Hardware- In- the Loop Test using RTDS

Fig. 53 shows the experimental setup of hardware in the loop using real time digital simulator (RTDS). Power switch circuits including the DG inverter, LCL filter, step-down transformer connecting to the main power grid, and other power components are built in RSCAD. They are emulated in the RTDS. The proposed seamless control algorithm was implemented by the digital controller using the DSP control board (TMS320F28335). All PWM signals are transmitted RTDS through GTDI card. All voltage and current signals are measured from the output of GTA0 card.

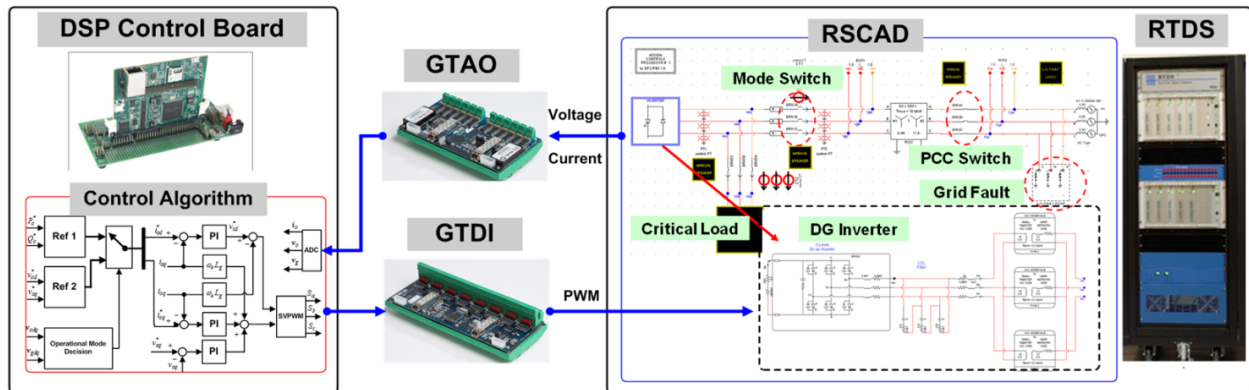


Fig. 53. Experimental setup of hardware in the loop using RTDS

4.5.2 Experimental Wave forms

Fig. 54 shows experimental waveforms of current control in GC mode during PCC switch-off period. Normal voltage is 88%~110% of the grid voltage. It shows that the current control in GC mode continues to operate during PCC switch-off period. The difference of the power between the DG inverter (20kW) and the resistive load (3.3kW) makes the overvoltage (130%).

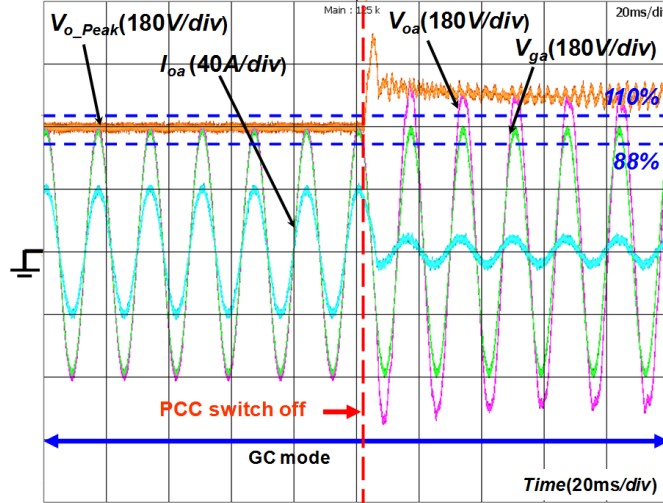


Fig. 54. Experimental waveform of current control in GC mode during PCC switch-off period with 3.3kW resistive load

Fig. 55 (a) shows experimental waveforms of the conventional mode transition from GC mode to SA mode during PCC switch-off period without the critical load. The control mode of the DG inverter is changed from the current control to the voltage control. The output voltage is regulated within 10msec. Fig. 55 (b) shows test waveform of the conventional control mode change during grid voltage swells. The control mode is changed from the current control in GC mode to the voltage control in GC mode. After the control mode is changed, the current of the DG inverter is increased, because the conventional voltage control has no the inner current loop with the current limiter. Therefore, the conventional voltage control has fast regulation capability in the overvoltage due to the PCC switch-off with no load condition. However, if the grid voltage swells, then the operation of the DG inverter becomes unstable likewise the reverse power flow.

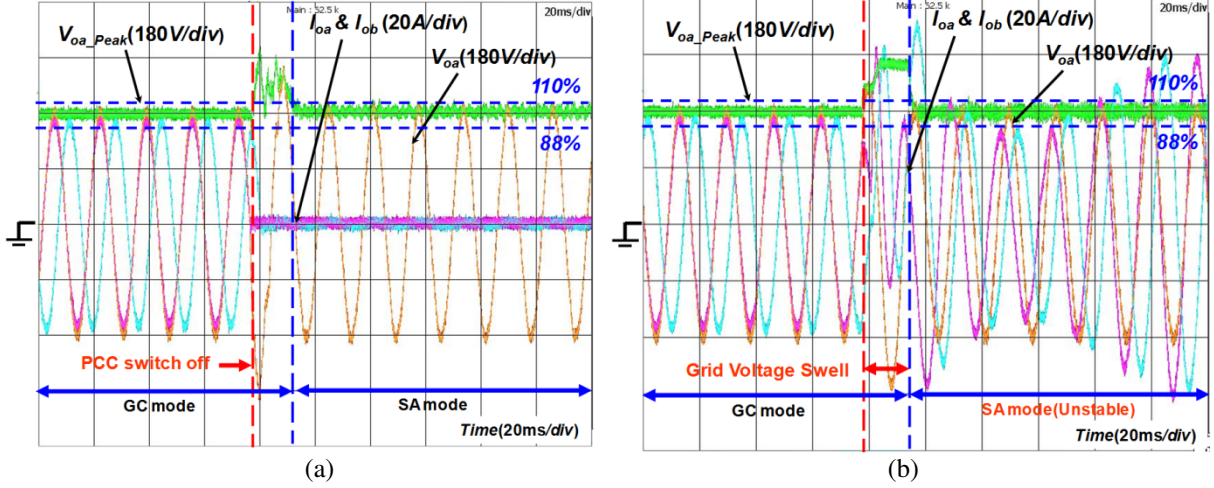


Fig. 55. Experimental waveforms of conventional mode transition using the voltage control without current loop, (a) mode transition from GC mode to SA mode during PCC switch-off period without critical load, (b) mode transition from GC mode to SA mode during grid voltage swell.

Fig. 56 (a) shows experimental waveforms of the proposed mode transition from GC mode to SA mode during PCC switch-off period without the critical load. The control mode of the DG inverter is used by the current control with feedforward voltage loop with changing the current reference in GC mode. The output voltage is regulated within 5ms. Fig. 56 (b) shows experimental waveforms of the proposed control mode change during grid voltage swell. The control mode of the DG inverter is used by the current control with feedforward voltage loop with changing the current reference in GC mode. After the operational mode is changed, the limited d - q -axis current will be generated. In the case of the grid voltage swell, the DG inverter will be operated by the current control with feedforward voltage loop using current reference in SA mode. After checking the grid fault, the DG inverter will change the current reference in SA mode to the current reference in GC mode without the instability shown in Fig. 56 (b).

Fig. 57 shows experimental waveforms of the proposed mode transition using the current control with feedforward voltage loop. Fig. 57 (a) shows the mode transition from 20kW active power generation in GC mode to 0.1kW resistive and 10kVar inductive loads in SA mode. The recovery time is within 10ms. Fig. 57 (b) shows the mode transition from 20kW active power generation in GC mode to 5kW resistive, 5kVar inductive, -10kVar capacitive loads in SA mode. The recovery time is within 10ms, which means that the proposed control method can transfer from GC mode to SA mode seamlessly.

Therefore, the fast mode transition can be carried out in order to minimize the overvoltage occurrence during the PCC switch-off period. This stable operation of DG inverter can be considered as ride through capability in the overvoltage due to the grid voltage swell.

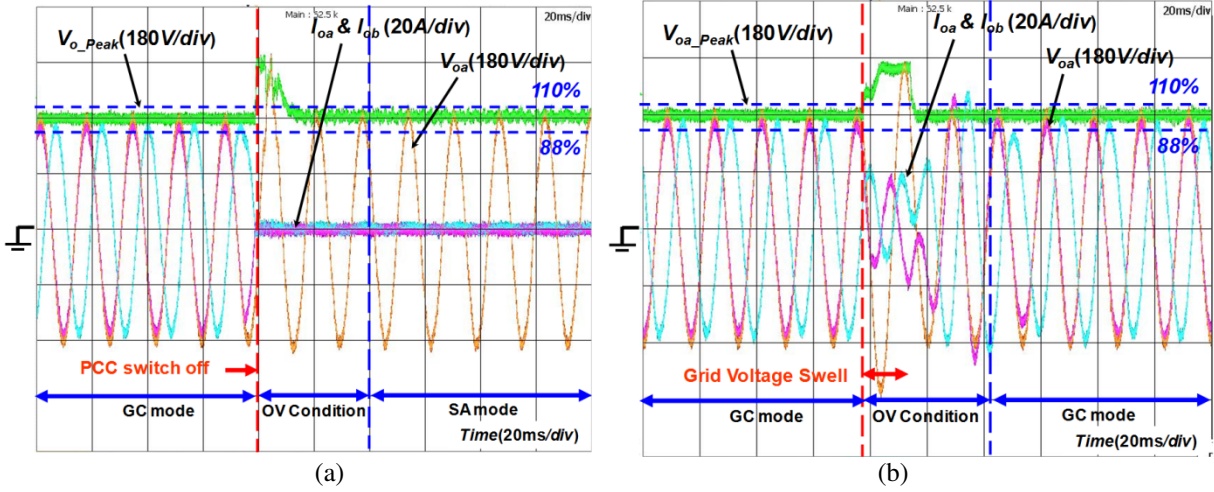


Fig. 56. Experimental waveforms of the proposed mode transition using the current control with feedforward voltage loop, (a) mode transition from GC mode to SA mode during PCC switch-off period without critical load, (b) control mode change during grid voltage swell

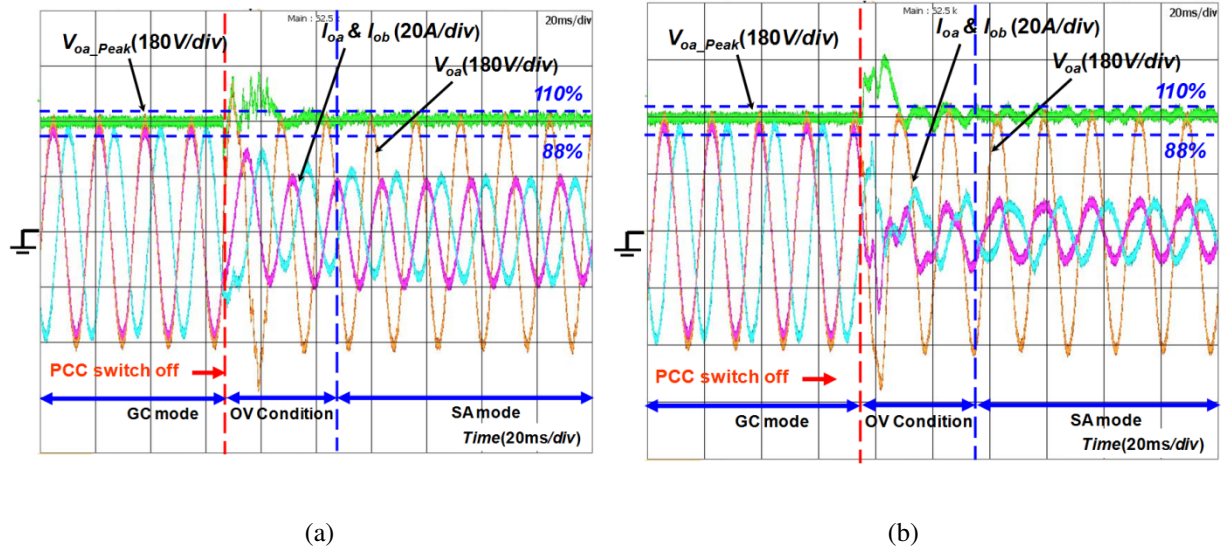


Fig. 57. Experimental waveforms of the proposed mode transition using the current control with feedforward voltage loop, (a) mode transition from 20kW power generation in GC mode to 0.1kW resistive and 10kVar inductive loads in SA mode, (b) mode transition from 20kW power generation in GC mode to 5kW resistive, 5kVar inductive, -10kVar capacitive loads in SA mode

4.6 Conclusion

This chapter presented a control strategy considering the response time of regulating output voltage in standalone operational mode transitions and stable operation of voltage control loop in grid connection mode under grid voltage overvoltage conditions. Conventional current control and voltage control loops have limited response for unknown power plant conditions during mode transition. The proposed control loop consists of a current controller and a feedforward voltage controller, which minimizes the grid overvoltage. The feedforward voltage control loop was added to the d - q axis current control loop. It responded within 1 or 2 cycles to protect the critical load in standalone operation during the grid fault conditions, and regulated the output voltage to maintain the critical load in standalone operational mode during the grid fault conditions. The proposed control strategy reduces the impact of the renewable energy and the critical load under the grid fault or disturbance conditions. In addition, the smooth operation of the distributed generation inverter will also enhance the stability and reliability of the utility grid. Real time digital simulator based hardware in the loop tests and simulation results showed that distributed generation inverter is able to achieve seamless mode change under grid overvoltage conditions.

CHAPTER 5. CONTROL OF LCL FILTER BASED DG INVERTERS TO SUPPRESS DC POWER OSCILLATION UNDER GRID VOLTAGE UNBALANCE

This chapter presents how to suppress a dc power oscillation of the *LCL* filter based DG inverter under unbalanced operating conditions³. The grid voltage unbalance affects to oscillate the dc voltage and dc current at the dc-link. This influences the life cycle of renewable energy systems such as photovoltaic or fuel cell power plants. In order to minimize the dc power oscillation, an enhanced current reference for the dc power oscillation suppression is necessary, because the conventional current reference is acceptable only for L filter based DG inverters but limited for *LCL* filter based DG inverters.

A new δ - γ transformation is proposed on the unbalanced rotating frame so that the unbalanced current vector becomes a constant vector without oscillation. By using the δ - γ transformation, the δ - γ frame current controller enables regulation of a constant current in the δ - γ axis as well as enhancement of the bandwidth of the controller. The proposed δ - γ frame current controller with improved current reference enables minimization of the dc power oscillation and enhancement of the response time of current control loop. The proposed control method will reduce the impact to the renewable energy sources under grid voltage unbalance. As a result, the dc power conversion without oscillation of the DG inverter will improve the stability and reliability of renewable energy sources. Simulation and hardware-in-the loop experimental results validated the proposed control method under unbalanced operating conditions.

5.1 Control overview of LCL filter based DG inverter under grid voltage unbalance

The objective of this chapter is 1) to minimize both dc voltage and dc current oscillations by means of the dc power oscillation, 2) to control sinusoidal output current without distortion under grid voltage unbalance. Fig. 58 shows a control overview to suppress the dc power oscillation of the *LCL* filter based DG inverter under grid voltage unbalance. The grid voltage unbalance affects the DG source with dc voltage and dc current ripples due to dc oscillating power generation and the output ac current with distortion as disturbances.

³ Some of the results presented in this chapter have been published in [140].

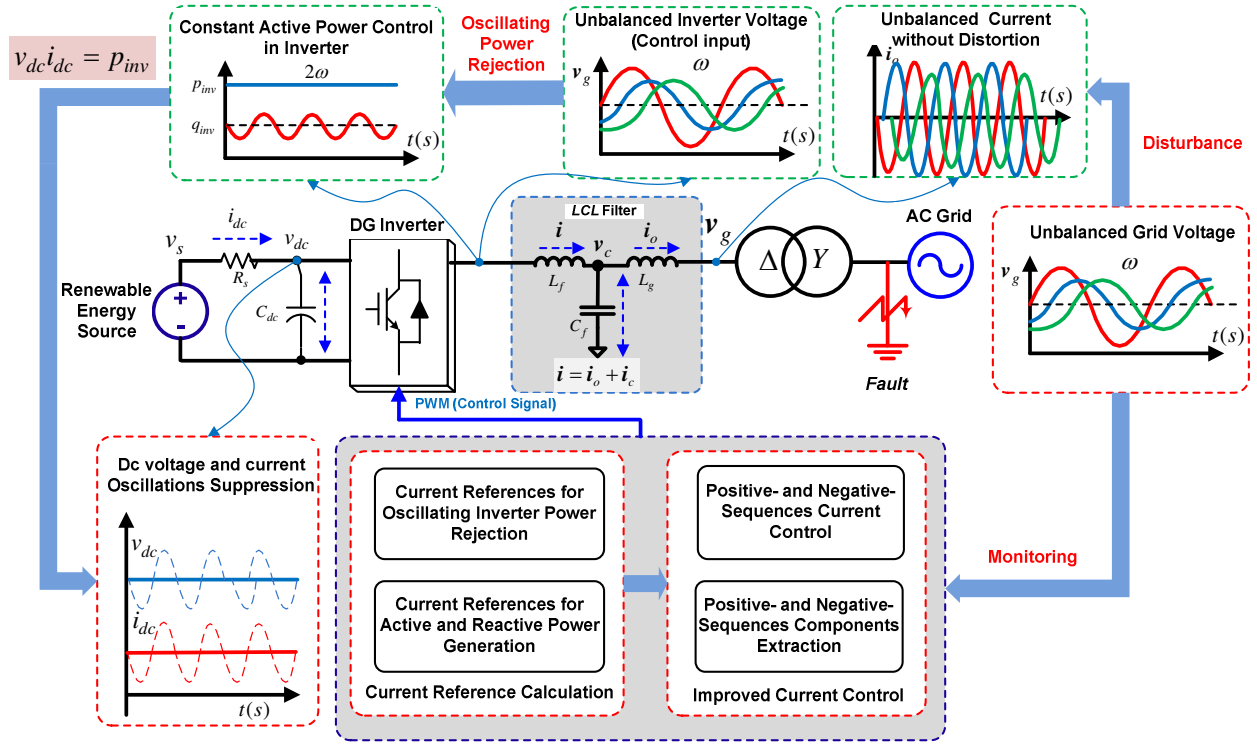


Fig.58. Overall control approaches to suppress dc power oscillation under grid voltage unbalance

Diverse current control schemes have been proposed to overcome these issues in the case of L filter based dc-ac inverters [101-104]. Their approaches are designed based on *symmetrical coordinate method* to extract the positive- and negative- sequence components of unbalanced current and voltage. Then, it regulates the positive- and negative- sequence current components [98]. Flexible active and reactive powers are generated by removing the oscillating powers of the inverter or the grid [105]. A constant active power generation without oscillating powers of the inverter is able to minimize the dc voltage and dc current oscillations because the dc power is linked to the active power of the inverter directly. However, the conventional approaches are limited to suppress the dc power oscillation for the LCL filter based dc-ac inverters. Therefore, we need *an enhanced current reference* to remove the dc oscillating powers by deriving a new current matrix.

In order to regulate the positive- and negative- sequence current components without distortion, double synchronous reference ($d-q$) frame current controllers have been proposed with conventional current reference blocks [101-104]. Conventional double $d-q$ frame current controller is composed of positive-

sequence d - q frame current controller and negative-sequence d - q frame current controller as extracting the positive- and negative-sequence current components with filters in the feedback. The performance is limited to improve the bandwidth of the controllers. Therefore, *an enhanced current control scheme* is proposed in this chapter.

5.2 Impact of DG Inverter under Grid Voltage Unbalance

5.1.1 DG inverter modeling under unbalanced grid voltage

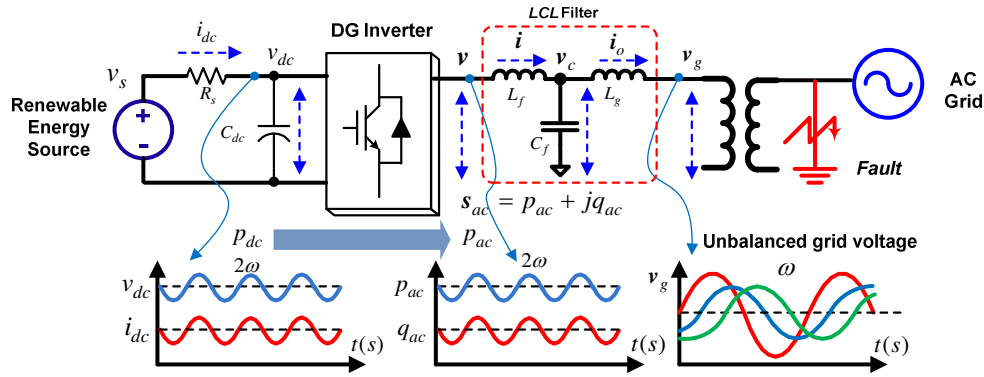


Fig. 59. Power flow of the LCL filter based DG inverter under unbalanced grid voltage.

Fig. 59 shows the LCL filter based DG inverter and its power flow under unbalanced grid voltage. where, v : the inverter voltage, v_c : the capacitor voltage of the LCL filter, v_g : the grid voltage, i : the inverter current, i_o : the output current, v_s : the DG source voltage, and i_{dc} : the dc current, L_f : the filter inductor, C_f : the filter capacitor, L_g : the grid inductor, C_{dc} : the dc link capacitor, R_s : the input impedance of the dc source, ω_{LCL} : the resonance frequency of the LCL filter.

The LCL filter based DG inverter system consists of the dc-ac inverter, the LCL filter, and the transformer. They are linked to the grid. When grid faults at the output of transformer occur, the input voltage of transformer will experience unbalanced grid voltage. Due to voltage unbalance, ac power oscillation is generated in the dc-ac inverter. Then dc current and dc voltage oscillations are generated at the dc-link due to oscillating active power of the dc-ac inverter. Thus, the dc power oscillation can affect the renewable energy source.

Current and voltage equations at the dc-link are given as

$$v_s = R_s i_{dc} + v_{dc} \quad (60)$$

$$i_{dc} = C_{dc} \frac{dv_{dc}}{dt} + \frac{p_{ac}}{v_{dc}} \quad (61)$$

$$p_{ac} = \text{Re}(s_{ac}) \quad (62)$$

The instantaneous power of dc-ac inverter is given as

$$s_{ac} = \frac{3}{2} \mathbf{v}_{dq} \cdot \bar{\mathbf{i}}_{dq} = \frac{3}{2} \mathbf{v}_{\alpha\beta} \cdot \bar{\mathbf{i}}_{\alpha\beta} \quad (63)$$

During unbalanced operating condition, the space vector in the α - β axis consists of the positive-sequence state vector in the d - q axis with respect to $e^{+j\theta}$ and the negative-sequence state vector in the d - q axis with respect to $e^{-j\theta}$ as follows:

$$\mathbf{x}_{\alpha\beta} = e^{+j\theta} \mathbf{x}_{dq}^+ + e^{-j\theta} \mathbf{x}_{dq}^- \quad (64)$$

where $\mathbf{x}_{dq}^+ = x_d^+ + jx_q^+$, $\mathbf{x}_{dq}^- = x_d^- + jx_q^-$, $\theta = \omega t$, θ : the phase angle of the grid voltage and, $\omega = 2\pi f$: the frequency of the grid voltage.

The positive-sequence voltage and current equations in the d - q axis are express as follows:

$$\mathbf{v}_{dq}^+ = L_f \frac{d\mathbf{i}_{dq}^+}{dt} + j\omega L_f \mathbf{i}_{dq}^+ + \mathbf{v}_{cdq}^+ \quad (65)$$

$$\mathbf{i}_{dq}^+ = C_f \frac{d\mathbf{v}_{cdq}^+}{dt} + j\omega C_f \mathbf{v}_{cdq}^+ + \mathbf{i}_{odq}^+ \quad (66)$$

$$\mathbf{v}_{cdq}^+ = L_g \frac{d\mathbf{i}_{odq}^+}{dt} + j\omega L_g \mathbf{i}_{odq}^+ + \mathbf{v}_{gdq}^+ \quad (67)$$

The negative-sequence voltage and current equations in the d - q axis are given as follows:

$$\mathbf{v}_{dq}^- = L_f \frac{d\mathbf{i}_{dq}^-}{dt} - j\omega L_f \mathbf{i}_{dq}^- + \mathbf{v}_{cdq}^- \quad (68)$$

$$\mathbf{i}_{dq}^- = C_f \frac{d\mathbf{v}_{cdq}^-}{dt} - j\omega C_f \mathbf{v}_{cdq}^- + \mathbf{i}_{odq}^- \quad (69)$$

$$\mathbf{v}_{cdq}^- = L_g \frac{d\mathbf{i}_{odq}^-}{dt} - j\omega L_g \mathbf{i}_{odq}^- + \mathbf{v}_{gdq}^- \quad (70)$$

5.1.2 Dc power oscillation due to oscillating ac power under grid voltage unbalance

During grid voltage unbalance, ac active and reactive powers of the dc-ac inverter are expressed as

$$\mathbf{s}_{ac} = \frac{3}{2} \left(\mathbf{v}_{dq}^+ e^{j\omega t} + \mathbf{v}_{dq}^- e^{-j\omega t} \right) \cdot \left(\mathbf{i}_{dq}^+ e^{-j\omega t} + \mathbf{i}_{dq}^- e^{j\omega t} \right) = p_{ac} + jq_{ac} \quad (71)$$

$$p_{ac} = p_0 + p_{c2} \cos(2\omega t) + p_{s2} \sin(2\omega t) \quad (72)$$

$$q_{ac} = q_0 + q_{c2} \cos(2\omega t) + q_{s2} \sin(2\omega t) \quad (73)$$

From (72) - (73), the dc components and the second order oscillating components of active and reactive powers are given as follows:

$$p_0 = 1.5 \left(v_d^+ i_d^+ + v_q^+ i_q^+ + v_d^- i_d^- + v_q^- i_q^- \right) \quad (74)$$

$$p_{c2} = 1.5 \left(v_d^- i_d^+ + v_q^- i_q^+ + v_d^+ i_d^- + v_q^+ i_q^- \right) \quad (75)$$

$$p_{s2} = 1.5 \left(v_q^- i_d^+ - v_d^- i_q^+ - v_q^+ i_d^- + v_d^+ i_q^- \right) \quad (76)$$

$$q_0 = 1.5 \left(v_q^+ i_d^+ - v_d^+ i_q^+ + v_q^- i_d^- - v_d^- i_q^- \right) \quad (77)$$

$$q_{c2} = 1.5 \left(v_q^- i_d^+ - v_d^- i_q^+ + v_q^+ i_d^- - v_d^+ i_q^- \right) \quad (78)$$

$$q_{s2} = 1.5 \left(-v_d^- i_d^+ - v_q^- i_q^+ + v_d^+ i_d^- + v_q^+ i_q^- \right) \quad (79)$$

From (60) and (61), the dc power at the dc-link and the ac power of dc-ac inverter are written as

$$p_{dc} = v_{dc} i_{dc} = -\frac{1}{R_s} v_{dc}^2 + \frac{1}{R_s} v_s v_{dc} \quad (80)$$

$$p_{ac} = -\frac{1}{R_s} v_{dc}^2 + \frac{1}{R_s} v_s v_{dc} - C_{dc} v_{dc} \frac{dv_{dc}}{dt} \quad (81)$$

Based on the small signal modeling, the transfer function from \tilde{p}_{ac} to \tilde{p}_{dc} is given as

$$G_{dc}(s) = \frac{\tilde{p}_{dc}}{\tilde{p}_{ac}} = \frac{\omega_{dc}}{s + \omega_{dc}} \quad (82)$$

where $\omega_{dc} = \frac{2V_{dc} - V_s}{V_{dc} R_s C_{dc}}$, V_s is a dc term of the dc source voltage, and V_{dc} is a dc term of the dc-link voltage.

Substituting (65)-(70) into (72), the active power oscillation can be express as

$$\tilde{p}_{ac} = P_{c2} \cos(2\omega t) + P_{s2} \sin(2\omega t) + \Delta p_{ac} \quad (83)$$

where Δp_{ac} is the high order terms. P_{c2} and P_{s2} are the ac power oscillation coefficients .

And the active power oscillation coefficients are written as follows:

$$\begin{cases} P_{c2} = 3\alpha_g Z_T (i_{oq}^- i_{od}^+ - i_{od}^- i_{oq}^+) \\ \quad + 1.5(\alpha_f \alpha_g - Z_T Y_C) (v_{gq}^+ i_{oq}^- + v_{gd}^+ i_{od}^- + v_{gq}^- i_{oq}^+ + v_{gd}^- i_{od}^+) \\ \quad + 1.5\alpha_f Y_C (-v_{gd}^- v_{gq}^+ + v_{gq}^- v_{gd}^+ + v_{gd}^+ v_{gq}^- - v_{gq}^+ v_{gd}^-) \end{cases} \quad (84)$$

$$\begin{cases} P_{s2} = -3\alpha_g Z_T (i_{od}^- i_{od}^+ + i_{oq}^- i_{oq}^+) \\ \quad + 1.5(Z_T Y_C - \alpha_f \alpha_g) (v_{gq}^+ i_{od}^- - v_{gd}^+ i_{oq}^- - v_{gq}^- i_{od}^+ + v_{gd}^- i_{oq}^+) \\ \quad - 1.5\alpha_f Y_C (v_{gq}^- v_{gq}^+ + v_{gd}^- v_{gd}^+ + v_{gq}^+ v_{gq}^- + v_{gd}^+ v_{gd}^-) \end{cases} \quad (85)$$

where $Z_T = \omega L_T - \omega^3 L_f L_g C_f$, $\alpha_f = 1 - \omega^2 L_f C_f$, $\alpha_g = 1 - \omega^2 L_g C_g$, $Y_C = \omega C_f$, $L_T = L_g + L_f$.

These results are caused by the modeling of the *LCL* filter based inverter. In the case of the *L* filter based inverter modeling, the ac power oscillation coefficients are the same to (75) and (76) because the inverter current equals to the output current through *L* filter. Therefore, conventional current references are computed by (74) - (79) [101-104]. We need a *new current reference* in order to remove the dc power oscillation of the *LCL* filter based DG inverter from (84) and (85).

The dc power oscillation is a result that the ac power oscillation in (83) passes a low pass filter in (82). Therefore the high order term, Δp_{ac} , can be filtered and ignored. Since the frequency of the oscillation

(2ω) is not high enough to be removed, the ac power oscillation coefficients become the dc power oscillation coefficients as follows:

$$\tilde{p}_{dc} = P_{c2} \cos(2\omega t) + P_{s2} \sin(2\omega t) \quad (86)$$

If the double d - q frame current controller are applied to regulate unbalanced output current [98], transfer functions from the d - q axis current references, \mathbf{i}_{odq}^{+*} and \mathbf{i}_{odq}^{-*} , to the d - q axis output currents, \mathbf{i}_{odq}^{+*} and \mathbf{i}_{odq}^{-*} are given as

$$G_c^+(s) = \frac{\mathbf{i}_{odq}^+}{\mathbf{i}_{odq}^{+*}}, \text{ and } G_c^-(s) = \frac{\mathbf{i}_{odq}^-}{\mathbf{i}_{odq}^{-*}} \quad (87)$$

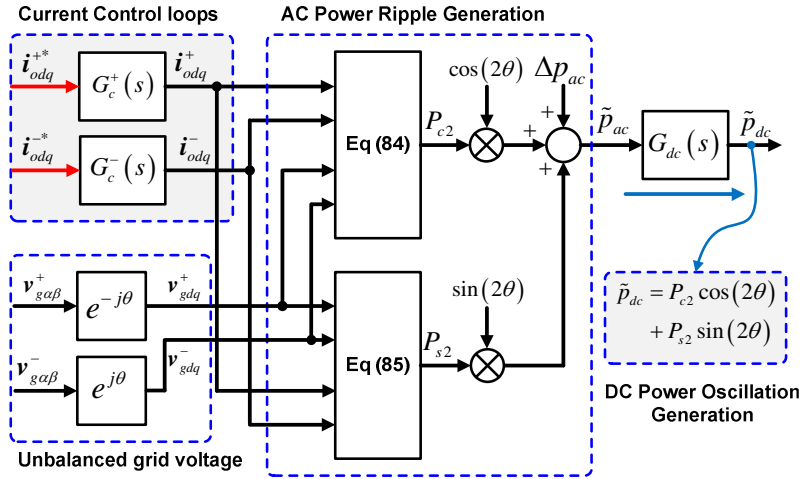


Fig. 60. Block diagram of the dc power oscillation generation under unbalanced grid voltage.

Fig. 60 shows the block diagram of the dc power oscillation generation under unbalanced grid voltage. This analysis for a mechanism of the dc power oscillation generation is to minimize the dc power oscillation of the LCL filter based DG inverter under grid voltage unbalance. If we can find conditions to remove the dc power oscillation coefficients in (85) and (86), the dc power oscillation, \tilde{p}_{dc} , will be rejected. The only way to remove the dc power oscillation is to generate the current references, \mathbf{i}_{odq}^{+*} and \mathbf{i}_{odq}^{-*} . Therefore, it is necessary to find the current references to suppress power oscillation coefficients.

5.2 Performance of Conventional Control Scheme

5.2.1 Conventional current reference calculations [98]

The conditions to deliver a constant inverter power without power oscillations of L filter inverter are given as

$$\begin{cases} P = \frac{3}{2} \left(v_{gd}^+ i_{od}^+ + v_{gq}^+ i_{oq}^+ + v_{gd}^- i_{od}^- + v_{gq}^- i_{oq}^- \right) \\ Q = \frac{3}{2} \left(v_{gq}^+ i_{od}^+ - v_{gd}^+ i_{oq}^+ + v_{gq}^- i_{od}^- - v_{gd}^- i_{oq}^- \right) \\ p_{c2} = \frac{3}{2} \left(v_d^- i_{od}^+ + v_q^- i_{oq}^+ + v_d^+ i_{od}^- + v_q^+ i_{oq}^- \right) = 0 \\ p_{s2} = \frac{3}{2} \left(v_q^- i_{od}^+ - v_d^- i_{oq}^+ - v_q^+ i_{od}^- + v_d^+ i_{oq}^- \right) = 0 \end{cases} \quad (88)$$

From (88), the power vector is written with the current components ($i_{od}^+, i_{oq}^+, i_{od}^-$ and i_{oq}^-) in the following matrix expression:

$$\begin{bmatrix} P \\ Q \\ P_{c2} \\ P_{s2} \end{bmatrix} = \frac{3}{2} \begin{bmatrix} v_{gd}^+ & v_{gq}^+ & v_{gd}^- & v_{gq}^- \\ v_{gq}^+ & -v_{gd}^+ & v_{gq}^- & -v_{gd}^- \\ v_d^- & v_q^- & v_d^+ & v_q^+ \\ v_q^- & -v_d^- & -v_q^+ & v_d^+ \end{bmatrix} \begin{bmatrix} i_{od}^+ \\ i_{oq}^+ \\ i_{od}^- \\ i_{oq}^- \end{bmatrix} \quad (89)$$

By inverting this matrix, it is possible to find the current references to generate active and reactive powers without active power oscillation under grid voltage unbalance, i.e.

$$\begin{bmatrix} i_{od}^{+*} \\ i_{oq}^{+*} \\ i_{od}^{-*} \\ i_{oq}^{-*} \end{bmatrix} = \frac{2}{3} \begin{bmatrix} v_{gd}^+ & v_{gq}^+ & v_{gd}^- & v_{gq}^- \\ v_{gq}^+ & -v_{gd}^+ & v_{gq}^- & -v_{gd}^- \\ v_d^- & v_q^- & v_d^+ & v_q^+ \\ v_q^- & -v_d^- & -v_q^+ & v_d^+ \end{bmatrix}^{-1} \begin{bmatrix} P^* \\ Q^* \\ 0 \\ 0 \end{bmatrix} \quad (90)$$

Substituting (90) into (85) and (86), the dc power oscillation can be derived in the L and LCL filter based inverters.

1) L filter based inverter ($C_f = 0$)

$$\begin{aligned}
P_{c2} &= 1.5(v_{gq}^+ + Z_T i_{od}^+) i_{oq}^- + 1.5(v_{gd}^+ - Z_T i_{od}^+) i_{od}^- \\
&\quad + 1.5(v_{oq}^- - Z_T i_{od}^-) i_{oq}^+ + 1.5(v_{gd}^- + Z_T i_{oq}^-) i_{od}^+ = 0 \\
P_{s2} &= 1.5(v_q^+ i_{od}^- - v_d^+ i_{oq}^- - v_q^- i_{od}^+ + v_d^- i_{oq}^+) = 0
\end{aligned} \tag{91}$$

Hence, the dc power oscillation is able to be removed as follows:

$$\tilde{p}_{dc} = P_{c2} \cos(2\omega t) + P_{s2} \sin(2\omega t) = 0 \tag{91}$$

2) *LCL* filter based inverter

The P_{c2} and P_{s2} are not canceled as follows:

$$\tilde{p}_{dc} = P_{c2} \cos(2\omega t) + P_{s2} \sin(2\omega t) \neq 0 \tag{92}$$

If the DG inverter is connected with the *LCL* filter, additional current, which is the capacitor current, is generated. However, the current reference calculation in (90) is derived by considering the *L* filter based inverter, which assumes that the inverter current equals to the output current. Fig. 61 shows simulation waveforms of dc voltage and dc current oscillation suppression using conventional current reference in (90). Results show that the dc current and dc voltage oscillations are not reduced under grid voltage unbalance in the *LCL* filter based inverter.

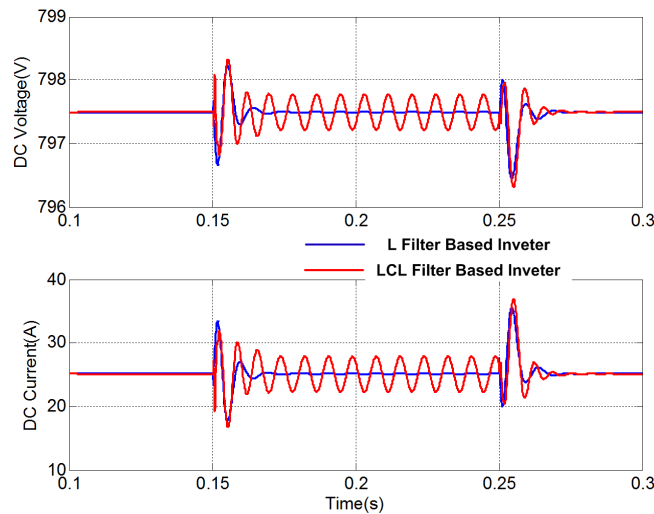


Fig. 61. Simulation waveforms of dc voltage and dc current oscillation suppression using conventional current reference.

5.2.3 Conventional double synchronous reference frame current control [98]

Fig. 62 shows the block diagram of conventional d - q frame current control. In order to extract the positive- and negative-sequence components, either a notch filter at 2ω or an all pass filter can be implemented. The positive-sequence current controller is designed with a PI regulator. The negative-sequence current controller is the same to the positive-sequence current controller. The current references are generated by (90). In order to analyze the dynamic response of conventional d - q frame current control, the transfer function can be derived from the space vector analysis.

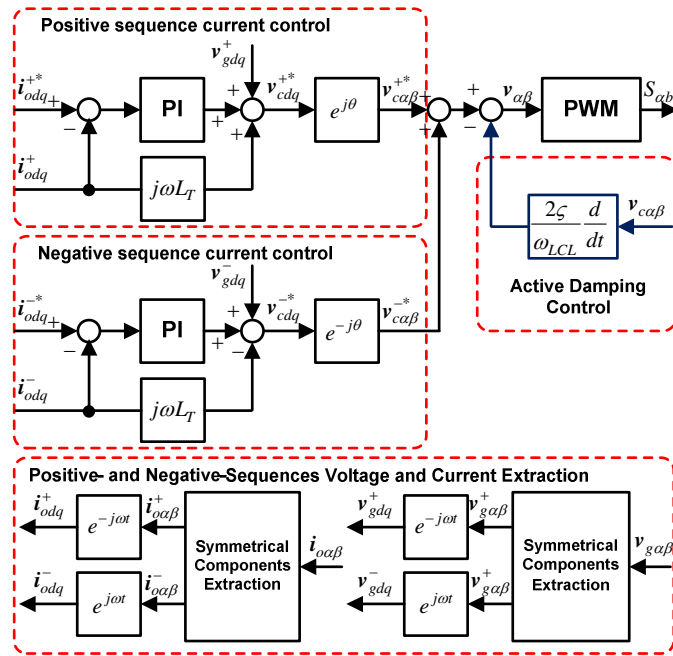


Fig. 62. Block diagram of double d - q frame current control.

A space vector, $\mathbf{x}_{\alpha\beta}$ is written as

$$\mathbf{x}_{\alpha\beta}(t) = e^{j\omega t} \mathbf{x}_{dq}^+(t) + e^{-j\omega t} \mathbf{x}_{dq}^-(t) \quad (93)$$

From Appendix C, a skew-symmetric complex operator of positive-sequence is expressed as

$$\mathbf{T}_{\alpha\beta}^+ = \frac{1}{2}(1 + j\hat{q}) \quad (94)$$

A skew-symmetric complex operator of negative-sequence is expressed as

$$\mathbf{T}_{\alpha\beta}^- = \frac{1}{2}(1 - j\hat{q}) \quad (95)$$

By applying (94) and (95) in (93), the positive- and negative- sequence state vectors in the α - β axis are computed as

$$\begin{aligned} \mathbf{T}_{\alpha\beta}^+ \mathbf{x}_{\alpha\beta}(t) &= \frac{1}{2}(1 + j\hat{q}) \left(e^{j\omega t} \mathbf{x}_{dq}^+(t) + e^{-j\omega t} \mathbf{x}_{dq}^-(t) \right) \\ &= \frac{1}{2} \left(e^{j\omega t} \mathbf{x}_{dq}^+(t) + e^{j\frac{\pi}{2}} \hat{q} e^{j\omega t} \mathbf{x}_{dq}^+(t) \right) + \frac{1}{2} \left(e^{-j\omega t} \mathbf{x}_{dq}^-(t) + e^{j\frac{\pi}{2}} \hat{q} e^{-j\omega t} \mathbf{x}_{dq}^-(t) \right) \end{aligned} \quad (96)$$

$$\begin{aligned} \mathbf{T}_{\alpha\beta}^- \mathbf{x}_{\alpha\beta}(t) &= \frac{1}{2}(1 - j\hat{q}) \left(e^{j\omega t} \mathbf{x}_{dq}^+(t) + e^{-j\omega t} \mathbf{x}_{dq}^-(t) \right) \\ &= \frac{1}{2} \left(e^{j\omega t} \mathbf{x}_{dq}^+(t) + e^{-j\frac{\pi}{2}} \hat{q} e^{j\omega t} \mathbf{x}_{dq}^+(t) \right) + \frac{1}{2} \left(e^{-j\omega t} \mathbf{x}_{dq}^-(t) + e^{-j\frac{\pi}{2}} \hat{q} e^{-j\omega t} \mathbf{x}_{dq}^-(t) \right) \end{aligned} \quad (97)$$

Usually, the skew-symmetric operators in (94) and (95) are implemented by filtering methods such as the second-order adaptive filter (AF) based on a generalized integrator and the second-order AF based on a second-order generalized integrator [98]. These approaches are useful to extract symmetrical components of the grid voltage in the phase lock loop (PLL) for the grid synchronization because response time of the PLL is sufficient with using a low gain in terms of the phase angle of the grid voltage. However, the second-order filters to extract symmetrical components of the feedback current can affect the phase margin of the current control loop substantially. Therefore, the first-order all pass filter (APF) can be used to implement approximated phase-shifting operator.

Transfer function of the APF is given as

$$Q(s) = \frac{-s + \omega}{s + \omega} \quad (98)$$

The phase-shifting operator based on the APF can be transformed to frequency domain as follows:

$$\hat{q}e^{j\omega t}\mathbf{x}(t) \rightarrow e^{j\left(\theta-\frac{\pi}{2}\right)}Q(s)\mathbf{x}(s) \quad (99)$$

$$\hat{q}e^{j\omega t}\mathbf{x}(t) \rightarrow e^{j\left(\theta-\frac{\pi}{2}\right)}Q(s)\mathbf{x}(s) \quad (100)$$

By applying (99) and (100) in (96) and (97), frequency responses of the positive- and negative- sequence state vectors in the in the α - β axis are written as

$$\begin{aligned} \mathbf{T}_{\alpha\beta}^+\mathbf{x}_{\alpha\beta}(s) &= \frac{1}{2}\left(e^{j\theta}\mathbf{x}_{dq}^+ + e^{j\frac{\pi}{2}}e^{j\left(\theta-\frac{\pi}{2}\right)}Q(s)\mathbf{x}_{dq}^+(s)\right) + \frac{1}{2}\left(e^{-j\theta}\mathbf{x}_{dq}^- + e^{j\frac{\pi}{2}}e^{-j\left(\theta-\frac{\pi}{2}\right)}Q(s)\mathbf{x}_{dq}^-(s)\right) \\ &= \frac{1}{2}e^{j\theta}(1+Q(s))\mathbf{x}_{dq}^+(s) + \frac{1}{2}e^{-j\theta}(1-Q(s))\mathbf{x}_{dq}^-(s) \\ &= e^{j\theta}\frac{\omega}{s+\omega}\mathbf{x}_{\alpha\beta}^+ + e^{-j\theta}\frac{s}{s+\omega}\mathbf{x}_{\alpha\beta}^- \end{aligned} \quad (101)$$

$$\begin{aligned} \mathbf{T}_{\alpha\beta}^-\mathbf{x}_{\alpha\beta}(s) &= \frac{1}{2}\left(e^{j\theta}\mathbf{x}_{dq}^+ + e^{-j\frac{\pi}{2}}e^{j\left(\omega t-\frac{\pi}{2}\right)}Q(s)\mathbf{x}_{dq}^+(s)\right) + \frac{1}{2}\left(e^{-j\theta}\mathbf{x}_{dq}^- + e^{-j\frac{\pi}{2}}e^{-j\left(\theta-\frac{\pi}{2}\right)}Q(s)\mathbf{x}_{dq}^-(s)\right) \\ &= \frac{1}{2}e^{j\theta}(1-Q(s))\mathbf{x}_{dq}^+(s) + \frac{1}{2}e^{-j\theta}(1+Q(s))\mathbf{x}_{dq}^-(s) \\ &= e^{j\theta}\frac{s}{s+\omega}\mathbf{x}_{\alpha\beta}^+ + e^{-j\theta}\frac{\omega}{s+\omega}\mathbf{x}_{\alpha\beta}^- \end{aligned} \quad (102)$$

Therefore, frequency responses of the positive- and negative- sequence state vectors in the in the d - q axis are expressed as

$$\hat{\mathbf{x}}_{dq}^+(s) = e^{-j\theta}\mathbf{T}_{\alpha\beta}^+\mathbf{x}_{\alpha\beta}(s) = \frac{\omega}{s+\omega}\mathbf{x}_{dq}^+(s) + e^{-j2\theta}\frac{s}{s+\omega}\mathbf{x}_{dq}^-(s) \quad (103)$$

$$\hat{\mathbf{x}}_{dq}^-(s) = e^{j\theta}\mathbf{T}_{\alpha\beta}^-\mathbf{x}_{\alpha\beta}(s) = \frac{\omega}{s+\omega}\mathbf{x}_{dq}^-(s) + e^{j2\theta}\frac{s}{s+\omega}\mathbf{x}_{dq}^+(s) \quad (104)$$

From (103) and (104), the positive- and negative-sequence components in the d - q axis after applying the phase-shifting operator based on the APF include the response of the first order low pass filter(LPF) as follows:

$$\left. \frac{\hat{i}_{odq}^+}{i_{odq}^+} \right|_{i_{odq}^- = 0} = \frac{\omega}{s + \omega}, \text{ and } \left. \frac{\hat{i}_{odq}^-}{i_{odq}^-} \right|_{i_{odq}^+ = 0} = \frac{\omega}{s + \omega} \quad (105)$$

Fig. 63 shows the simplified double d - q frame current control loop. By applying the active damping control, the equivalent transfer function from v_c^* to v_c becomes a second order system. Due to the first order LPF in (105) for positive- and negative-sequence current components extraction, it will lose the phase margin in the control loop. Hence, this double d - q frame current controller has a limitation to achieve high bandwidth.

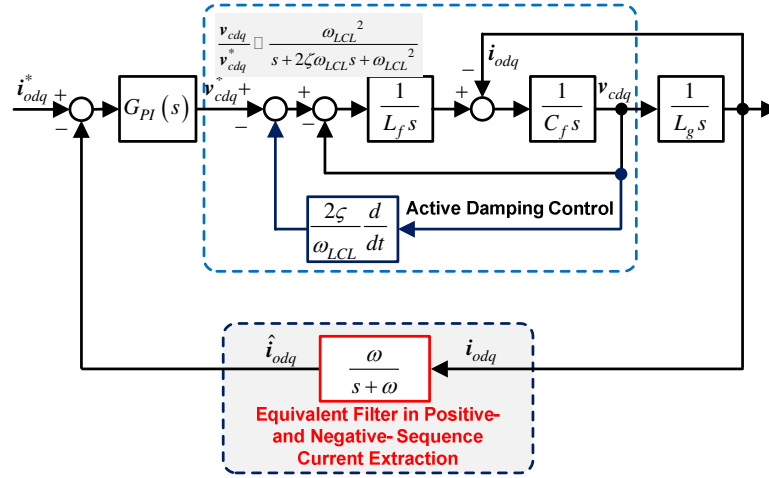


Fig. 63. Simplified double d - q frame current control loop.

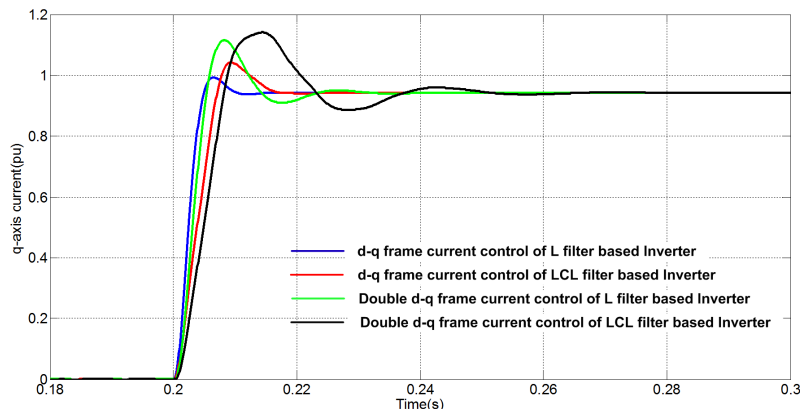


Fig. 64. Step responses of conventional current controllers of L and LC filters based inverter.

Fig. 64 shows step responses of conventional current controllers of L and LC filters based dc-ac inverters. The response times of controllers are determined by the order of the transfer function with

respect to the plant and filter. The conventional $d-q$ frame current controller is designed with the current using the $d-q$ rotating frame and without filtering in the feedback. The transfer function of L filter based inverter is the first order system with an integrator form. The LCL filter with active damping is the second order system as shown in Fig. 63. Thus, the transfer function of LCL filter based inverter becomes the third order system. The $d-q$ frame current controller of the L filter based inverter in Fig.64 shows the fastest response time, because there are no feedback filter and the LCL filter in the plant. But the double $d-q$ frame current controller of the LCL filter based inverter is more difficult to obtain the same response time of the $d-q$ frame current controller of the L filter based inverter, because it includes the second order system in the plant as well as the filter in the feedback. Since the double $d-q$ frame current controller is proposed to regulate the current for the LCL filter based DG inverter under grid voltage unbalance, the response time of the $d-q$ axis current is limited in terms of the stability vs. bandwidth.

5.3 Proposed Control Scheme for Suppression of DC Power Oscillation

In this section, two methods to minimize the dc power oscillation are proposed. First, an improved current reference is used to cancel coefficients of the dc power oscillation. Second, a modified reference frame current control is proposed to overcome the performance limitation of the double $d-q$ frame current control using the conventional filter approach to extract the positive- and negative-sequence current components. The proposed control scheme is able to not only regulate the unbalanced output current but also enhance the bandwidth of controller.

5.3.1 Improved current reference calculation

The conditions to deliver a constant inverter power without power oscillations of LCL filter inverter are given as

$$\begin{cases} P = \frac{3}{2} \left(v_{gd}^+ i_{od}^+ + v_{gq}^+ i_{oq}^+ + v_{gd}^- i_{od}^- + v_{gq}^- i_{oq}^- \right) \\ Q = \frac{3}{2} \left(v_{gq}^+ i_{od}^+ - v_{gd}^+ i_{oq}^+ + v_{gq}^- i_{od}^- - v_{gd}^- i_{oq}^- \right) \\ \tilde{p}_{dc} = P_{c2} \cos(2\omega t) + P_{s2} \sin(2\omega t) \square 0 \Leftrightarrow P_{c2} = 0 \text{ and } P_{s2} = 0 \end{cases} \quad (106)$$

From (84), (85), and (106), the power vector is given with the following matrix:

$$\begin{bmatrix} P \\ Q \\ P_{c2} \\ P_{s2} \end{bmatrix} = \frac{3}{2} \begin{bmatrix} v_{gd}^+ & v_{gq}^+ & v_{gd}^- & v_{gq}^- \\ v_{gq}^+ & -v_{gd}^+ & v_{gq}^- & -v_{gd}^- \\ \alpha v_d^- & \alpha v_q^- & \alpha v_d^+ & \alpha v_q^+ \\ \alpha v_q^- & -\alpha v_d^- & -\alpha v_q^+ & \alpha v_d^+ \end{bmatrix} \begin{bmatrix} i_{od}^+ \\ i_{oq}^+ \\ i_{od}^- \\ i_{oq}^- \end{bmatrix} - \frac{3}{2} Y_C \begin{bmatrix} 0 \\ 0 \\ v_{gq}^+ v_d^- - v_{gd}^+ v_q^- - v_{gq}^- v_d^+ + v_{gd}^- v_q^+ \\ v_{gq}^+ v_q^- + v_{gd}^+ v_d^- + v_{gq}^- v_q^+ + v_{gd}^- v_d^+ \end{bmatrix} \quad (107)$$

where $\alpha_g = 1 - \omega^2 L_g C_f$, $Y_C = \omega C_f$.

By inverting the voltage matrix in (107), *new current reference vector* is given as follows:

$$\begin{bmatrix} i_{od}^{+*} \\ i_{oq}^{+*} \\ i_{od}^{-*} \\ i_{oq}^{-*} \end{bmatrix} = \frac{2}{3} \begin{bmatrix} v_{gd}^+ & v_{gq}^+ & v_{gd}^- & v_{gq}^- \\ v_{gq}^+ & -v_{gd}^+ & v_{gq}^- & -v_{gd}^- \\ \alpha v_d^- & \alpha v_q^- & \alpha v_d^+ & \alpha v_q^+ \\ \alpha v_q^- & -\alpha v_d^- & -\alpha v_q^+ & \alpha v_d^+ \end{bmatrix}^{-1} \begin{bmatrix} P^* \\ Q^* \\ P_{c2}^{ff} \\ Q_{s2}^{ff} \end{bmatrix} \quad (108)$$

In order to cancel both dc current and dc voltage oscillations, oscillating power compensation terms are given as

$$P_{c2}^{ff} = \frac{3}{2} \omega C_f \left(v_{gq}^+ v_d^- - v_{gd}^+ v_q^- - v_{gq}^- v_d^+ + v_{gd}^- v_q^+ \right) \quad (109)$$

$$P_{s2}^{ff} = \frac{3}{2} \omega C_f \left(v_{gq}^+ v_q^- + v_{gd}^+ v_d^- + v_{gq}^- v_q^+ + v_{gd}^- v_d^+ \right) \quad (110)$$

5.3.2 State Vector under Unbalance Operating Conditions

DG inverters are usually connected to the grid using a three-wire connection without zero-sequence component. Therefore the zero-sequence component of the voltage vector can be ignored in the equations presented in this chapter [98].

The state vector in the α - β axis consists of the positive-sequence state vector in the d - q axis and the negative-sequence state vector in the d - q axis as follows:

$$\begin{bmatrix} x_\alpha \\ x_\beta \end{bmatrix} = R_{dq}^{-1}(\theta) \begin{bmatrix} x_d^+ \\ x_q^+ \end{bmatrix} + R_{dq}(\theta) \begin{bmatrix} x_d^- \\ x_q^- \end{bmatrix} \quad (111)$$

where x_d^+, x_q^+ : positive-sequence components in the d - q axis, and x_d^-, x_q^- : negative-sequence components in the d - q axis.

The d - q transformation with respect to $e^{-j\theta}$ is defined as

$$R_{dq}(\theta) = \begin{bmatrix} \cos \theta & \sin \theta \\ -\sin \theta & \cos \theta \end{bmatrix} \quad (112)$$

Fig. 65 shows the positive- and negative-sequence *synchronous reference frames* (or d - q frame) in the α - β axis. The positive-sequence d - q frame is rotated anticlockwise. The negative-sequence d - q frame is rotated clockwise (Appendix B).

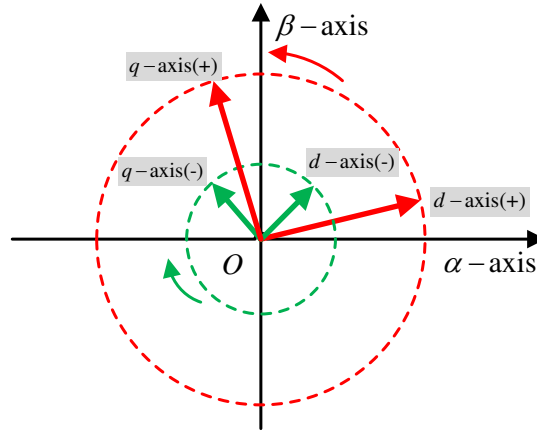


Fig. 65. Positive- and negative-sequence synchronous reference frames

From (111) and (112), the state vector in the α - β axis can be organized as

$$\begin{bmatrix} x_\alpha \\ x_\beta \end{bmatrix} = \begin{bmatrix} x_d^+ + x_d^- & -x_q^+ + x_q^- \\ x_q^+ + x_q^- & x_d^+ - x_d^- \end{bmatrix} \begin{bmatrix} \cos \theta \\ \sin \theta \end{bmatrix} \quad (113)$$

By inverting the matrix in (113), the cosine and sine terms are expressed as

$$\begin{bmatrix} \cos \theta \\ \sin \theta \end{bmatrix} = \frac{1}{D} \begin{bmatrix} a_{11} & a_{12} \\ a_{21} & a_{22} \end{bmatrix} \begin{bmatrix} x_\alpha \\ x_\beta \end{bmatrix} \quad (114)$$

where $D = (x_d^+)^2 + (x_q^+)^2 - (x_d^-)^2 - (x_q^-)^2$, $a_{11} = x_d^+ - x_d^-$, $a_{12} = x_q^+ - x_q^-$, $a_{21} = -x_q^+ - x_q^-$, and

$$a_{22} = x_d^+ + x_d^-.$$

By using the property of the trigonometric function, the trajectory of the state vector in the α - β axis becomes a *general ellipse equation* by the following:

$$Ax_\alpha^2 + Bx_\alpha x_\beta + Cx_\beta^2 = D \quad (115)$$

$$\text{where } A = \frac{(a_{11}^2 + a_{21}^2)}{D}, B = 2 \frac{(a_{11}a_{12} + a_{21}a_{22})}{D}, C = \frac{(a_{12}^2 + a_{22}^2)}{D}.$$

Fig. 66 shows the loci of positive- and negative-sequence state vectors and unbalanced state vector in the α - β axis. The ellipse is a trajectory by a circle of the negative-sequence vector with clockwise rotation, traveling along the line of a circle of the positive-sequence vector with anticlockwise rotation.

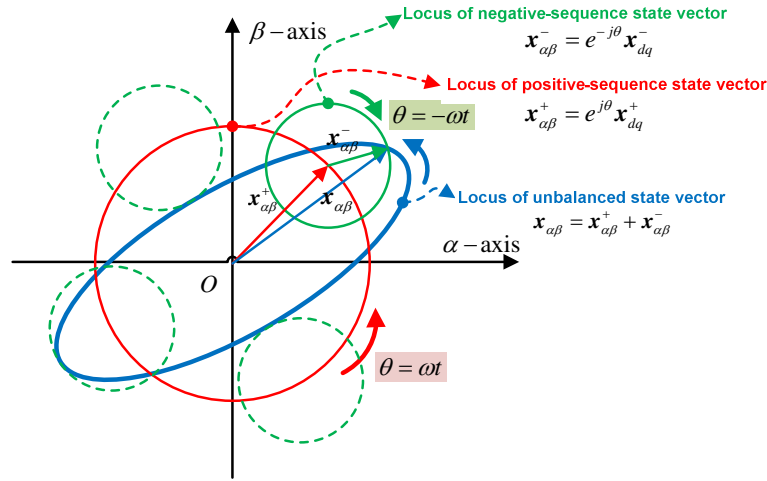


Fig. 66. Loci of positive- and negative-sequence state vectors and unbalanced state vector in the α - β axis.

From (115), the $Bx_\alpha x_\beta$ term can be eliminated by using the *rotation of axes* (Appendix D) as follows formulas:

$$x'_\alpha = \cos \phi x_\alpha - \sin \phi x_\beta, \text{ and } x'_\beta = \sin \phi x_\alpha + \cos \phi x_\beta \quad (116)$$

$$\text{where } \phi = -\frac{1}{2} \tan^{-1} \left(\frac{x_d^+ x_q^- + x_d^- x_q^+}{x_d^+ x_d^- - x_q^+ x_q^-} \right).$$

Then a *standard ellipse equation* is transformed as

$$A'x_\alpha'^2 + C'x_\beta'^2 = D \quad (117)$$

$$\text{where } A' = A \cos^2 \phi + B \cos \phi \sin \phi + C \sin^2 \phi, C' = A \sin^2 \phi - B \cos \phi \sin \phi + C \cos^2 \phi.$$

Fig. 67 shows the rotation of axes between the general ellipse and the standard ellipse.

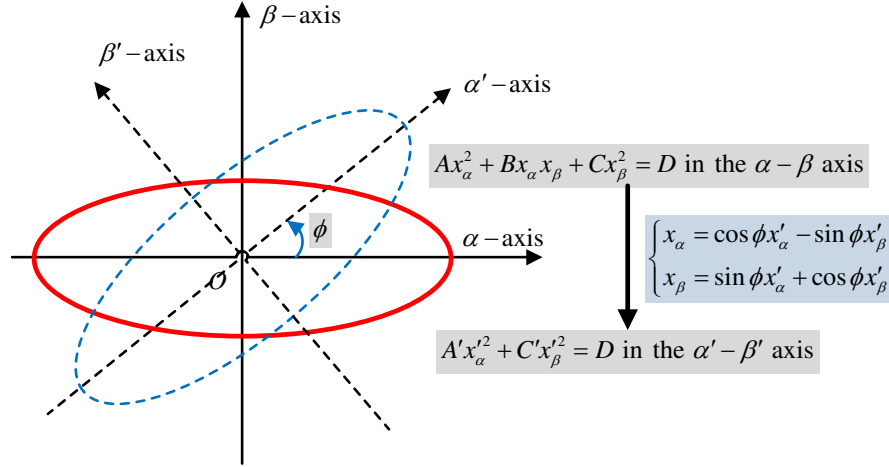


Fig. 67. Rotation of axes between general ellipse and standard ellipse.

Moreover, a circle can be obtained by scaling the standard ellipse as follows formulas:

$$x'_\alpha = \frac{1}{\sqrt{A'}} x''_\alpha, x'_\beta = \frac{1}{\sqrt{A'}} x''_\beta \quad (118)$$

Then the circle equation is expressed as

$$x''_\alpha^2 + x''_\beta^2 = D \quad (119)$$

Fig. 68 shows the scaling between the canonical ellipse and the circle.

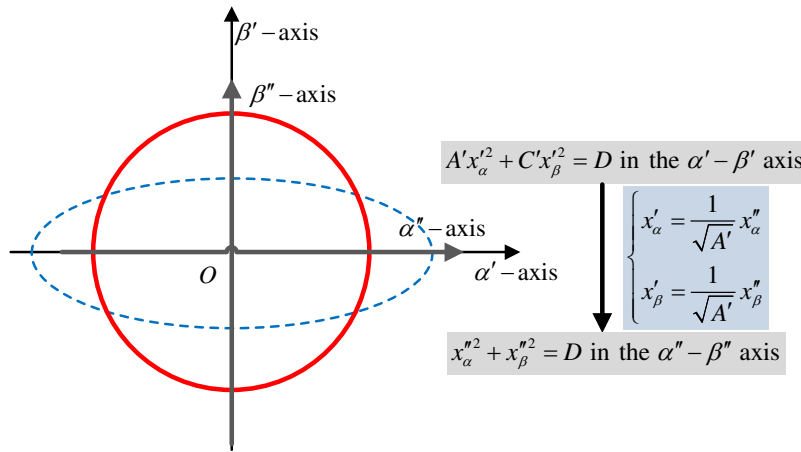


Fig. 68. Scaling between canonical ellipse and circle.

Therefore, any general ellipse equation in the α - β axis is able to map the circle equation in the new axis. It means that the unbalanced state vector is able to be considered as a constant vector on the unbalanced rotating frame.

5.3.2 Modified transformation on the unbalanced rotation frame

From (116), the rotation transformation matrix from the general ellipse to the standard ellipse is defined as

$$\begin{bmatrix} x'_\alpha \\ x'_\beta \end{bmatrix} = \begin{bmatrix} \cos \phi & \sin \phi \\ -\sin \phi & \cos \phi \end{bmatrix} \begin{bmatrix} x_\alpha \\ x_\beta \end{bmatrix} \quad (120)$$

$$\text{where } \phi = -\frac{1}{2} \tan^{-1} \left(\frac{x_d^+ x_q^- + x_d^- x_q^+}{x_d^+ x_d^- - x_q^+ x_q^-} \right).$$

From (117), the scaling transformation matrix from the standard ellipse to the circle is defined as

$$\begin{bmatrix} x''_\alpha \\ x''_\beta \end{bmatrix} = \begin{bmatrix} \sqrt{A'} & 0 \\ 0 & \sqrt{B'} \end{bmatrix} \begin{bmatrix} x'_\alpha \\ x'_\beta \end{bmatrix} \quad (121)$$

where $a_{11} = x_d^+ - x_d^-$, $a_{12} = x_q^+ - x_q^-$, $a_{21} = -x_q^+ - x_q^-$, and $a_{22} = x_d^+ + x_d^-$,

$$A = \frac{(a_{11}^2 + a_{21}^2)}{D}, B = 2 \frac{(a_{11}a_{12} + a_{21}a_{22})}{D}, C = \frac{(a_{12}^2 + a_{22}^2)}{D}, D = (x_d^+)^2 + (x_q^+)^2 - (x_d^-)^2 - (x_q^-)^2$$

$$A' = A \cos^2 \phi + B \cos \phi \sin \phi + C \sin^2 \phi, C' = A \sin^2 \phi - B \cos \phi \sin \phi + C \cos^2 \phi.$$

With the rotation transformation matrix in (120) and the scaling transformation matrix in (121), they can be combined as

$$\underbrace{\begin{bmatrix} x'_d \\ x'_q \end{bmatrix}}_{\text{Constant sate vector}} = \underbrace{\begin{bmatrix} \cos \theta & \sin \theta \\ -\sin \theta & \cos \theta \end{bmatrix}}_{d-q \text{ Transformation}} \underbrace{\begin{bmatrix} \sqrt{A'} & 0 \\ 0 & \sqrt{B'} \end{bmatrix}}_{\text{Scaling}} \underbrace{\begin{bmatrix} \cos \phi & \sin \phi \\ -\sin \phi & \cos \phi \end{bmatrix}}_{\text{Rotation of axes}} \underbrace{\begin{bmatrix} x_\alpha \\ x_\beta \end{bmatrix}}_{\text{Unbalanced sate vector}} \quad (122)$$

By using the d - q transformation matrix, the combined transformation is computed as

$$\begin{aligned}
T'_{dq}(\theta) &= R_{dq}(\theta) \begin{bmatrix} \sqrt{A'} & 0 \\ 0 & \sqrt{C'} \end{bmatrix} R_{dq}(\phi) \\
&= \sqrt{A} \begin{bmatrix} \cos(\theta + \phi_2) & \sqrt{\frac{C}{A}} \sin(\theta + \phi_1) \\ -\sin(\theta + \phi_2) & \sqrt{\frac{C}{A}} \cos(\theta + \phi_1) \end{bmatrix}
\end{aligned} \tag{123}$$

From (123), we define a *new δ - γ transformation matrix* as follows:

$$U_{\delta\gamma}(k, \phi_1, \theta) = \begin{bmatrix} \cos(\theta + \phi_2) & k \sin(\theta + \phi_1) \\ -\sin(\theta + \phi_2) & k \cos(\theta + \phi_1) \end{bmatrix} \tag{124}$$

The inverse transform matrix is expressed as

$$U_{\delta\gamma}^{-1}(k, \phi_1, \theta) = \frac{1}{\cos(\phi_1 - \phi_2)} \begin{bmatrix} \cos(\theta + \phi_1) & -\sin(\theta + \phi_1) \\ -\frac{1}{k} \sin(\theta + \phi_2) & \frac{1}{k} \cos(\theta + \phi_2) \end{bmatrix} \tag{125}$$

The unbalance factors, k , ϕ_1 , and ϕ_2 , are defined as follows:

$$k = \sqrt{\frac{(x_d^+ + x_d^-)^2 + (x_q^+ - x_q^-)^2}{(x_q^+ + x_q^-)^2 + (x_d^+ - x_d^-)^2}} \tag{126}$$

$$\phi_1 = \tan^{-1} \left(\frac{x_q^+ - x_q^-}{x_d^+ + x_d^-} \right), \text{ and } \phi_2 = \tan^{-1} \left(\frac{x_q^+ + x_q^-}{x_d^+ - x_d^-} \right) \tag{127}$$

From (113), the state vector in the α - β axis can be organized as

$$\begin{bmatrix} x_\alpha \\ x_\beta \end{bmatrix} = \begin{bmatrix} (x_d^+ + x_d^-) \cos \theta + (x_q^- - x_q^+) \sin \theta \\ (x_q^+ + x_q^-) \cos \theta + (x_d^+ - x_d^-) \sin \theta \end{bmatrix} \tag{128}$$

Then, it can be rewritten as

$$\begin{bmatrix} x_\alpha \\ x_\beta \end{bmatrix} = \begin{bmatrix} X \cos(\theta + \phi_1) \\ \frac{X}{k} \sin(\theta + \phi_2) \end{bmatrix} \tag{129}$$

In (129), the constant state vector in the δ - γ axis is expressed by the positive- and negative-sequence state vectors in the d - q axis as follows:

$$\begin{bmatrix} x_\delta \\ x_\gamma \end{bmatrix} = U_{\delta\gamma}(k, \phi_1, \theta) \begin{bmatrix} x_\alpha \\ x_\beta \end{bmatrix} = \begin{bmatrix} \sqrt{(x_d^+ + x_d^-)^2 + (x_q^+ - x_q^-)^2} \cos(\phi_1 - \phi_2) \\ 0 \end{bmatrix} \quad (130)$$

The δ - γ axis is the modified d - q axis on the unbalanced rotating frame. Then the unbalanced state vector in the α - β axis is transformed to constant state vector in the δ - γ axis.

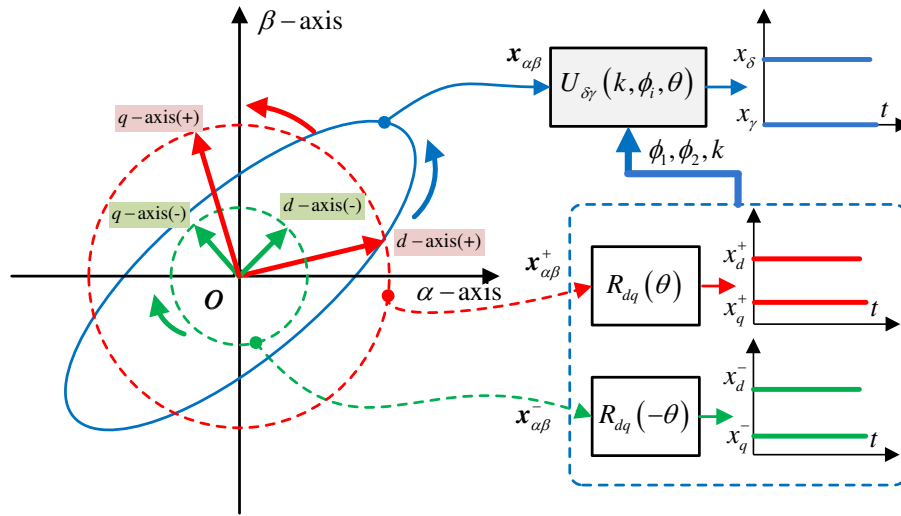


Fig. 69. Comparison between the δ - γ transformation and the d - q transformation under unbalanced operating conditions

Fig 69 shows the comparison between the δ - γ transformation and the d - q transformation under unbalanced condition. The locus of unbalanced state makes the ellipse in the α - β axis in (115). The positive- and negative-sequence state vectors draw circles in (117). Unbalance factors (k , ϕ_1 , and ϕ_2) are derived by the positive- and negative-sequence components in (126) and (127). With unbalanced factors, the δ - γ transformation makes a constant state vector in the δ - γ axis. This means that unbalanced state vector in the α - β axis is able to make constant state vector in (130). It includes positive- and negative-sequence components in the d - q axis without $\theta = \omega t$.

5.3.3 Dynamic voltage equation on the unbalanced rotating frame

The voltage equation with the active damping controller in the α - β axis can be approximated as

$$\mathbf{v}_{c\alpha\beta} = L_T \frac{d\mathbf{i}_{o\alpha\beta}}{dt} + \mathbf{v}_{g\alpha\beta} \quad (131)$$

To apply the voltage equation in the α - β axis, the δ - γ transformation is defined as

$$U_{\delta\gamma}(k^*, \phi_i^*, \theta) = \begin{bmatrix} \cos(\theta + \phi_2^*) & k^* \sin(\theta + \phi_1^*) \\ -\sin(\theta + \phi_2^*) & k^* \cos(\theta + \phi_1^*) \end{bmatrix} \quad (132)$$

where $k^* = \sqrt{\frac{(i_{od}^{+*} + i_{od}^{-*})^2 + (i_{oq}^{+*} - i_{oq}^{-*})^2}{(i_{oq}^{+*} + i_{oq}^{-*})^2 + (i_{od}^{+*} - i_{od}^{-*})^2}}$, $\phi_1^* = \tan^{-1}\left(\frac{i_{oq}^{+*} - i_{oq}^{-*}}{i_{od}^{+*} + i_{od}^{-*}}\right)$, $\phi_2^* = \tan^{-1}\left(\frac{i_{oq}^{+*} + i_{oq}^{-*}}{i_{od}^{+*} - i_{od}^{-*}}\right)$, and the $i_{od}^{+*}, i_{oq}^{+*}, i_{od}^{-*}$,

and i_{oq}^{-*} are the current references computed by (108)-(110) to minimize the dc voltage and dc current oscillations.

By applying the δ - γ transformation in (131), the voltage equation is expressed as

$$U_{\delta\gamma}(k^*, \phi_i^*, \theta) \begin{bmatrix} v_{c\alpha} \\ v_{c\beta} \end{bmatrix} = L_T U_{\delta\gamma}(k^*, \phi_i^*, \theta) \frac{d}{dt} \begin{bmatrix} i_{o\alpha} \\ i_{o\beta} \end{bmatrix} + U_{\delta\gamma}(k^*, \phi_i^*, \theta) \begin{bmatrix} v_{g\alpha} \\ v_{g\beta} \end{bmatrix} \quad (133)$$

From (133), the voltage equation in the δ - γ axis is given as

$$\begin{aligned} \begin{bmatrix} v_{c\delta} \\ v_{c\gamma} \end{bmatrix} &= L_T U_{\delta\gamma}(k^*, \phi_i^*, \theta) \frac{d}{dt} \left(U_{\delta\gamma}^{-1}(k^*, \phi_i^*, \theta) U_{\delta\gamma}(k^*, \phi_i^*, \theta) \begin{bmatrix} i_{o\alpha} \\ i_{o\beta} \end{bmatrix} \right) + \begin{bmatrix} v_{g\delta} \\ v_{g\gamma} \end{bmatrix} \\ &= L_T \frac{d}{dt} \begin{bmatrix} i_{o\delta} \\ i_{o\gamma} \end{bmatrix} + \underbrace{L_T U_{\delta\gamma}(k^*, \phi_i^*, \theta) \frac{d}{dt} U_{\delta\gamma}^{-1}(k^*, \phi_i^*, \theta)}_{\text{Decoupling term}} \begin{bmatrix} i_{o\delta} \\ i_{o\gamma} \end{bmatrix} + \begin{bmatrix} v_{g\delta} \\ v_{g\gamma} \end{bmatrix} \end{aligned} \quad (134)$$

Since unbalance factors, k^* and ϕ_i^* , are computed by the current references, they are independent to the feedback current in terms of dynamic state vector. Hence, the derivative of the unbalance factors can be ignored, then

$$\frac{dk^*}{dt} = 0, \text{ and } \frac{d\phi_i^*}{dt} = 0 \quad (135)$$

By computing the derivative of the δ - γ transformation, the decoupling term in (134) becomes as

$$U_{\delta\gamma}(k^*, \phi_i^*, \theta) \frac{d}{dt} U_{\delta\gamma}^{-1}(k^*, \phi_i^*, \theta) = \omega \begin{bmatrix} \tan(\phi_1^* - \phi_2^*) & -1 \\ 1 & -\tan(\phi_1^* - \phi_2^*) \end{bmatrix} \quad (136)$$

From (134) and (136), a new voltage equation in the δ - γ axis is written as

$$\begin{bmatrix} v_{c\delta}^* \\ v_{c\gamma}^* \end{bmatrix} = L_T \frac{d}{dt} \begin{bmatrix} i_{o\delta} \\ i_{o\gamma} \end{bmatrix} + \omega L_T \begin{bmatrix} \tan(\phi_1^* - \phi_2^*) & -1 \\ 1 & -\tan(\phi_1^* - \phi_2^*) \end{bmatrix} \begin{bmatrix} i_{o\delta} \\ i_{o\gamma} \end{bmatrix} + \begin{bmatrix} v_{g\delta} \\ v_{g\gamma} \end{bmatrix} \quad (137)$$

Based on this voltage equation, the δ - γ frame current control is designed with decoupling and feedforward compensations. However, the grid voltage does not become a constant state vector in the δ - γ axis because the δ - γ transformation is oriented by the current reference vector. The grid voltage in the α - β axis can be express as

$$\begin{bmatrix} v_{g\alpha} \\ v_{g\beta} \end{bmatrix} = \begin{bmatrix} V_m \cos(\theta + \phi_1) \\ \frac{V_m}{k} \sin(\theta + \phi_2) \end{bmatrix} \quad (138)$$

$$\text{where } k = \sqrt{\frac{(v_{gd}^+ + v_{gd}^-)^2 + (v_{gq}^+ - v_{gq}^-)^2}{(v_{gq}^+ + v_{gq}^-)^2 + (v_{gd}^+ - v_{gd}^-)^2}}, \phi_1 = \tan^{-1} \left(\frac{v_{gq}^+ - v_{gq}^-}{v_{gd}^+ + v_{gd}^-} \right), \phi_2 = \tan^{-1} \left(\frac{v_{gq}^+ + v_{gq}^-}{v_{gd}^+ - v_{gd}^-} \right).$$

The unbalance factors, k^* and ϕ_i^* , in the output current are not equal to the unbalance factors, k and ϕ_i , in the grid voltage as follows:

$$k^* \neq k, \phi_1^* \neq \phi_1, \text{ and } \phi_2^* \neq \phi_2 \quad (139)$$

Therefore, the grid voltage in the δ - γ axis becomes a function of $2\omega t$, i.e.

$$\begin{aligned} \begin{bmatrix} v_{g\delta} \\ v_{g\gamma} \end{bmatrix} &= U_{\delta\gamma}(k^*, \phi_i^*, \theta) \begin{bmatrix} V_m \cos(\theta + \phi_1) \\ \frac{V_m}{k} \sin(\theta + \phi_2) \end{bmatrix} \\ &= \frac{V_m}{2} \begin{bmatrix} \left(1 + \frac{k^*}{k}\right) \cos(\phi_1 - \phi_2^*) + \cos(2\theta + \phi_1 + \phi_2^*) - \frac{k^*}{k} \cos(2\theta + \phi_1^* + \phi_2) \\ \left(1 - \frac{k^*}{k}\right) \sin(\phi_1 - \phi_2^*) - \sin(2\theta + \phi_1 + \phi_2^*) + \frac{k^*}{k} \sin(2\theta + \phi_1^* + \phi_2) \end{bmatrix} \end{aligned} \quad (140)$$

Fig. 70 shows the loci of unbalanced current and voltage state vectors in the α - β axis. They are orthogonal but asymmetrical. In the view of the δ - γ transformation with the output current vector, the result of the δ - γ transformation with the grid voltage vector is oscillated with 2ω .

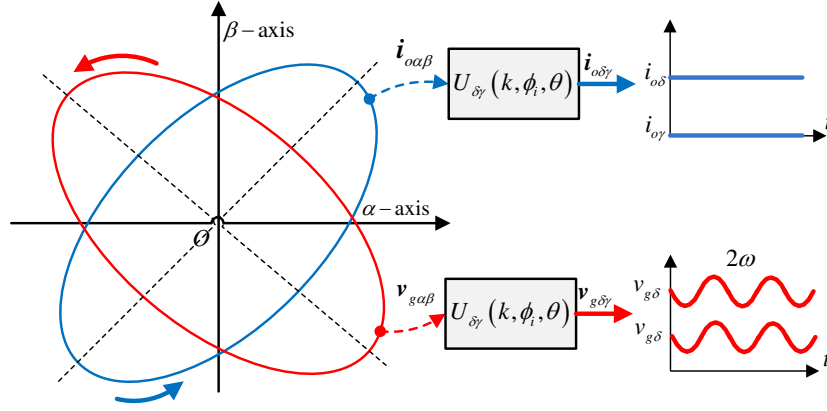


Fig. 70. Loci of unbalanced current and voltage vectors in the α - β axis.

5.3.4 Unbalanced grid voltage compensation on the unbalanced rotating frame

Fig. 71 shows the block diagram of current control loop in the δ - γ axis. Based on the δ - γ transformation, the feedback current becomes a constant state. The equivalent plant in the δ - γ axis has the δ - γ axis grid voltage oscillation in (140). To cancel this disturbance, the feedforward term is compensated. However, the feedforward term is difficult to cancel the δ - γ axis grid voltage exactly because there is the LCL filter with active damping. The oscillation term is delayed because of the second order system that is equivalent to the transfer function of the LCL filter with active damping.

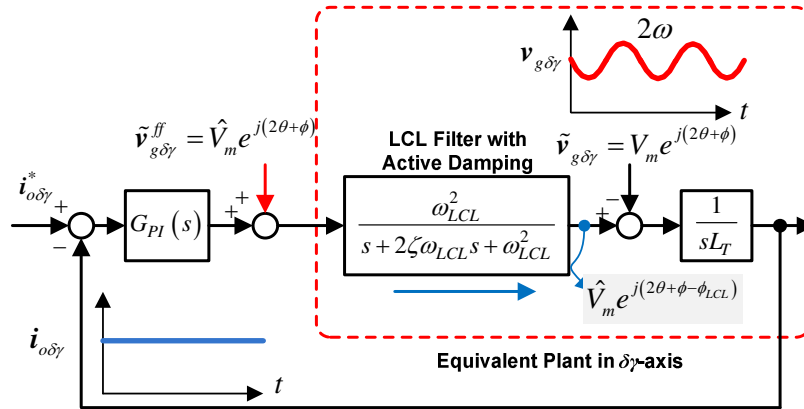


Fig. 71. Block diagram of current control loop in the δ - γ axis.

Fig. 72 shows the Bode plot of the *LCL* filter with active damping. Based on the frequency response, the phase response, ϕ_{LCL} , is 7.82° at 2ω (120Hz). This means that the δ - γ axis grid voltage in (140) is delayed with 7.82° phase response if the feedforward compensation is applied in the controller. The value of delayed phase is able to be computed from the frequency analysis of the second order system of the *LCL* filter with active damping.

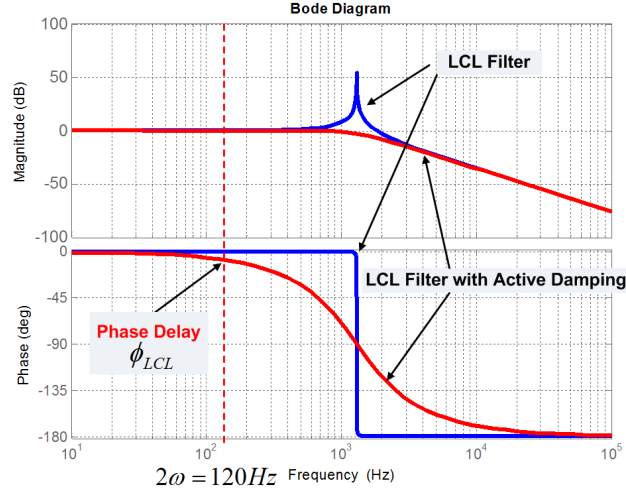


Fig. 72. Bode plot of *LCL* filter with active damping.

The frequency response of *LCL* filter with active damping is given as

$$G_{LCL}(s)\Big|_{s=j2\omega} = \frac{\omega_{LCL}^2}{s^2 + 2\zeta\omega_{LCL}s + \omega_{LCL}^2}\Big|_{s=j2\omega} \quad (141)$$

where $\omega_{LCL} = \sqrt{\frac{L_f + L_g}{L_f L_g C_f}}$, $\zeta \approx 0.707$.

Then the phase response of *LCL* filter with active damping at 2ω (120Hz) is computed as

$$\phi_{LCL} = \tan^{-1} \left(\frac{4\zeta\omega_{LCL}^3\omega}{4\omega_{LCL}^2\omega^2 - \omega_{LCL}^4} \right) \quad (142)$$

From (128), the modified feedforward vector with the phase compensation is given as

$$\begin{bmatrix} v_{g\delta}^{ff} \\ v_{g\gamma}^{ff} \end{bmatrix} = U_{\delta\gamma} \left(k^*, \phi_i^*, \theta + \phi_{LCL} \right) \begin{bmatrix} v_{g\alpha} \\ v_{g\beta} \end{bmatrix} \quad (143)$$

5.3.5 Proposed control scheme

Fig. 73 shows the proposed control block diagram for the dc power oscillation suppression. The proposed d - q current reference matrix in (108)-(110) computes the positive- and negative-sequence current references in the d - q axis. By using the d - q current reference, the δ - γ axis current reference is given as

$$\begin{bmatrix} i_{o\delta}^* \\ i_{o\gamma}^* \end{bmatrix} = \begin{bmatrix} \sqrt{(i_{od}^{*+} + i_{od}^{*-})^2 + (i_{oq}^{*+} - i_{oq}^{*-})^2} \cos(\phi_1^* - \phi_2^*) \\ 0 \end{bmatrix} \quad (144)$$

The unbalance factors and transformation are given in (132). The δ - γ frame current controller regulates the δ - γ axis current with respect to the unbalanced current in the α - β axis with the decoupling and feedforward compensations. In addition, the feedforward term in (143) compensates the δ - γ axis grid voltage with the phase delay.

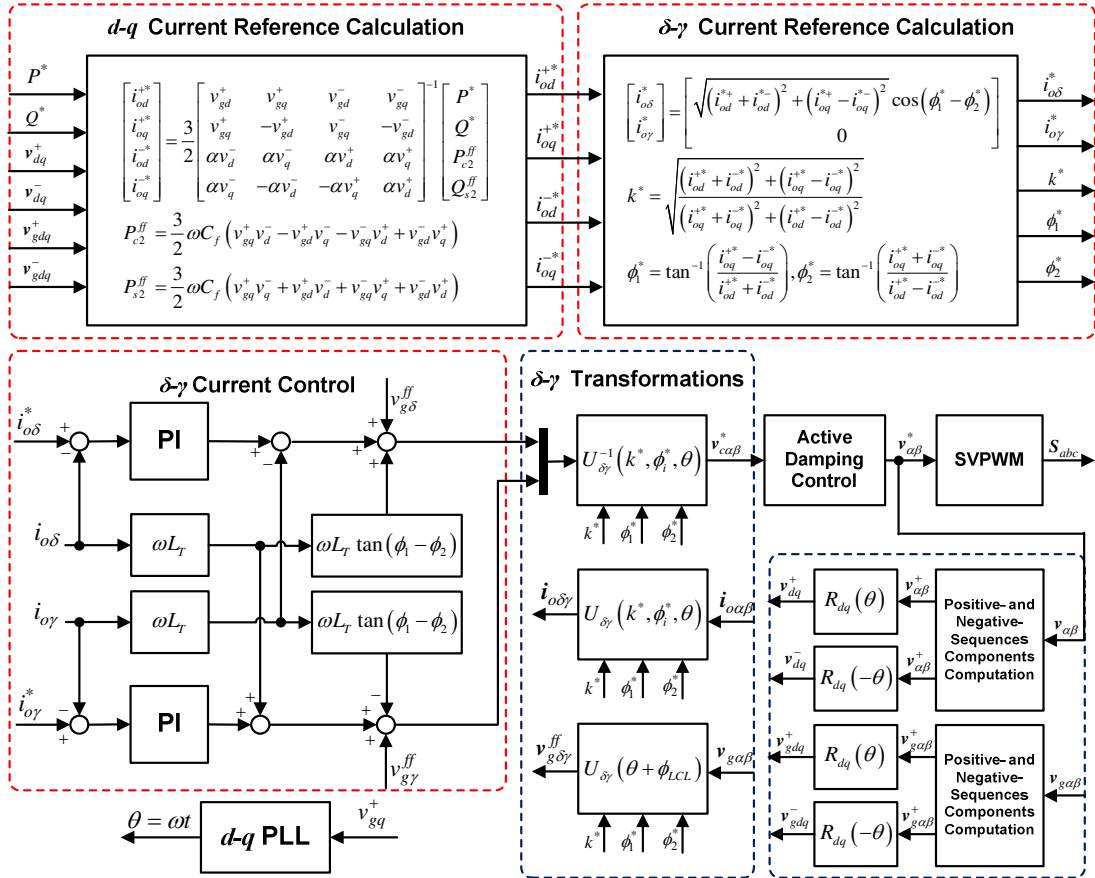


Fig. 73. Proposed control block diagram for dc power oscillation suppression.

5.4 Simulation Results

In order to validate the proposed control scheme, simulation is performed in Matlab. The unbalanced grid voltage occurs from 0.15s to 0.25s.

Fig. 74 shows simulation waveforms of d - q axis output current, dc voltage, and dc current with conventional and proposed control schemes. With conventional control approach, the dc voltage and dc current in terms of dc power are not regulated under unbalanced grid voltage, although the double d - q frame current loops are operated. On the other hand, in the proposed control approach, the dc voltage and dc current are regulated with constant values under grid voltage unbalance. Compared with the transient response time of the d - q axis output currents, the proposed control approach is faster than the conventional control approach.

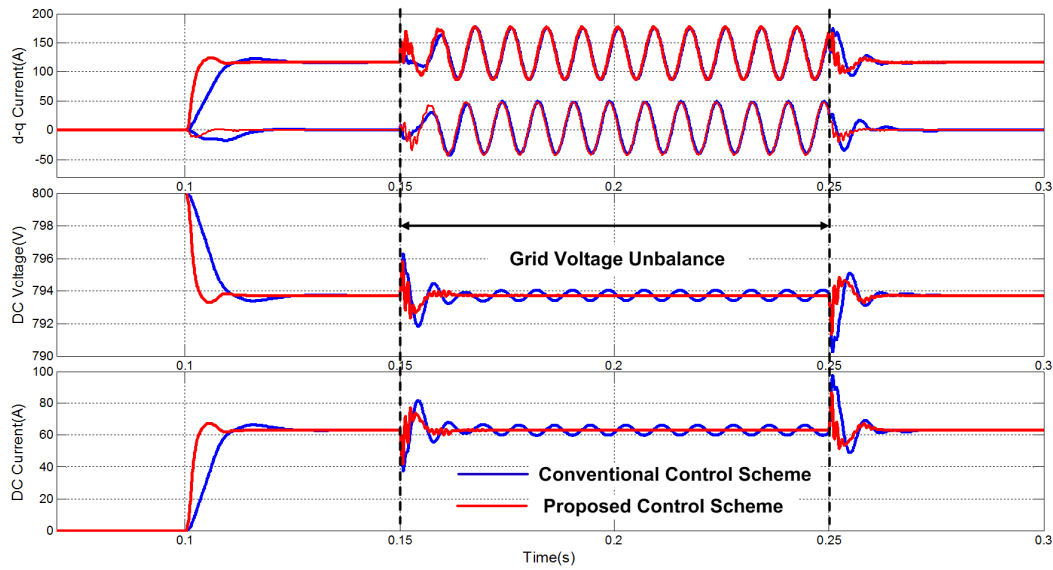


Fig. 74. Simulation waveforms of d - q axis output current, dc voltage, and dc current with conventional and proposed control schemes.

Fig. 75 shows simulation waveforms of the α - β axis current and the δ - γ axis current of proposed control scheme. The output current in the α - β axis is balanced from 0.1s to 0.15s and from 0.25s to 0.3s. The unbalanced current is generated from 0.15s to 0.25s because the controller is regulating to provide constant active power of the inverter under grid voltage unbalance. The loci of the α - β axis current is changed from a circle under balanced operating condition to an ellipse under unbalanced operating

condition. However the δ - γ axis current is always constant without oscillation because the δ - γ transformation makes constant state on unbalanced operating frame.

Fig. 76 shows simulation waveforms of three phase voltage, current, and dc power after applying the proposed controller under grid voltage unbalance. By using the proposed current reference, there is no dc power oscillation during unbalanced grid voltage.

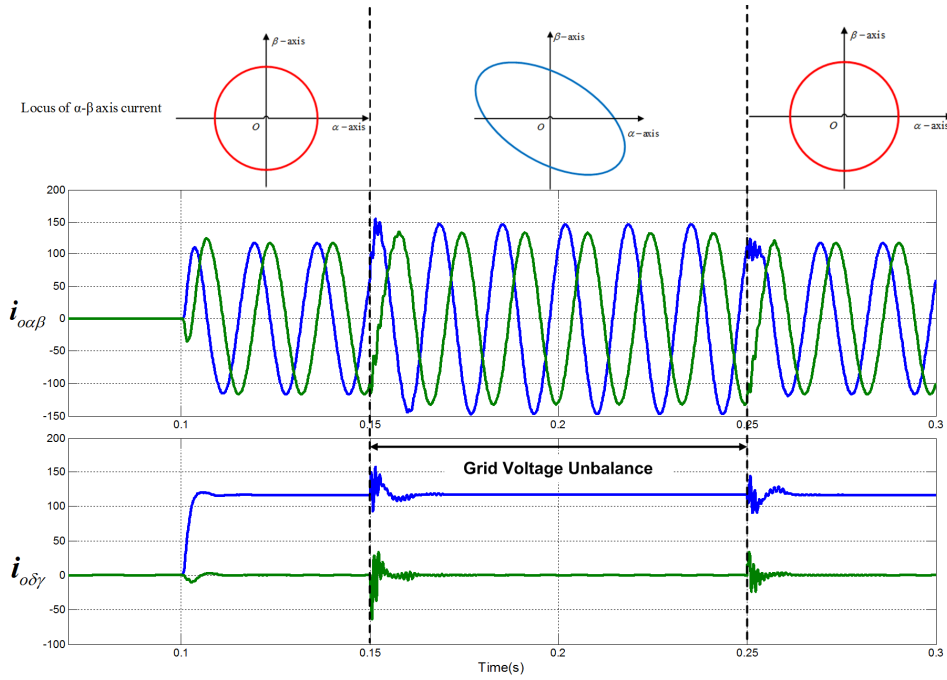


Fig. 75. Simulation waveforms of the α - β axis current and the δ - γ axis current of proposed control scheme.

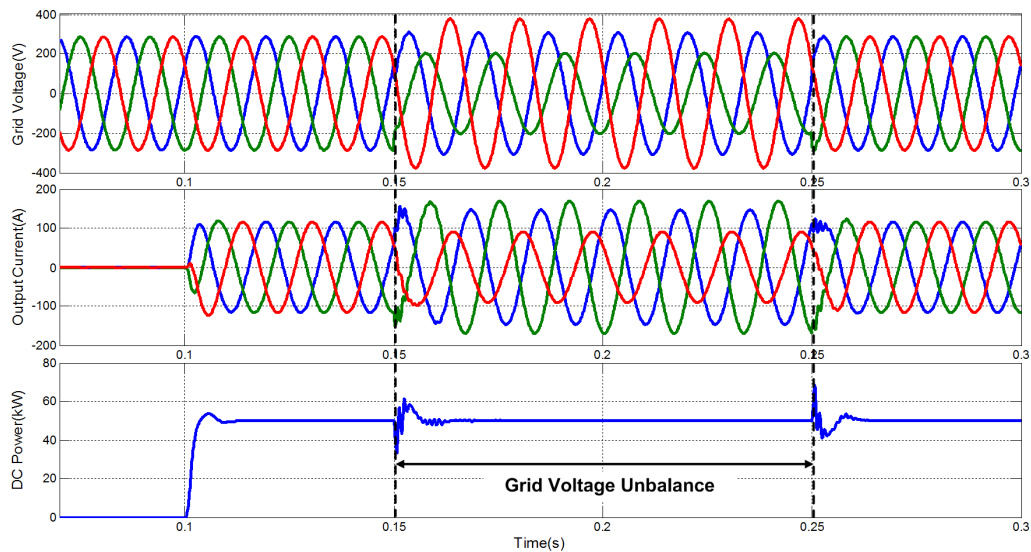


Fig. 76. Simulation waveforms of three phase voltage, current, and dc power of proposed control scheme.

5.5 Experimental Results

Fig. 77 shows the experimental setup of hardware in the loop using RTDS and dSPACE. Power switch circuits including the DG inverter, *LCL* filter, step-down transformer connecting to the main power grid, and other power components are built in RSCAD. They are emulated in the RTDS. The proposed current control algorithm was implemented by the digital controller using the DSP control board (TMS320F28335). All PWM signals are transmitted RTDS through GTDI card. All voltage and current signals are measured from the output of GTAO card. The dSPACE generates the current reference based on (108).

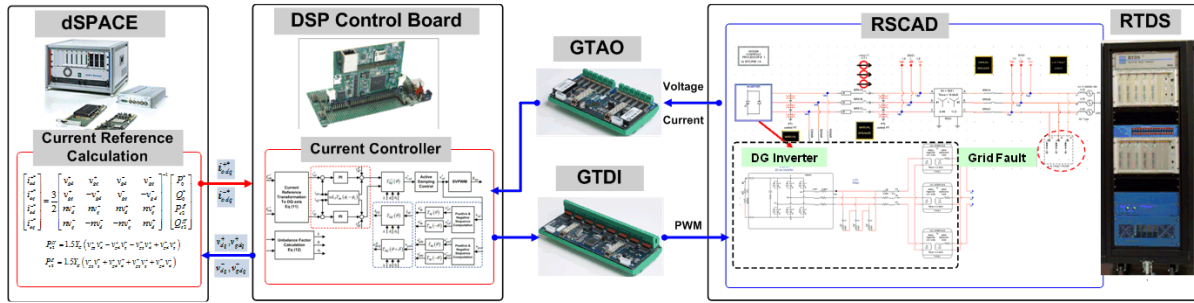


Fig. 77. Experimental setup of hardware in the loop using RTDS and dSPACE.

Fig. 78 shows experimental waveforms of conventional current control under balanced grid voltage. Fig. 79 shows experimental waveforms of conventional current control under unbalanced grid voltage. The conventional dual current control with current reference in (90) cannot remove the dc current and dc voltage's ripples under unbalanced grid voltage conditions. Fig. 80 shows experimental waveforms of proposed current control under unbalanced grid voltage. The proposed current control shows that the dc current and dc voltage's ripples are minimized under unbalanced grid voltage condition. Therefore, simulation and experimental results verified that the proposed control method can minimize the dc power ripple under unbalanced operating conditions.

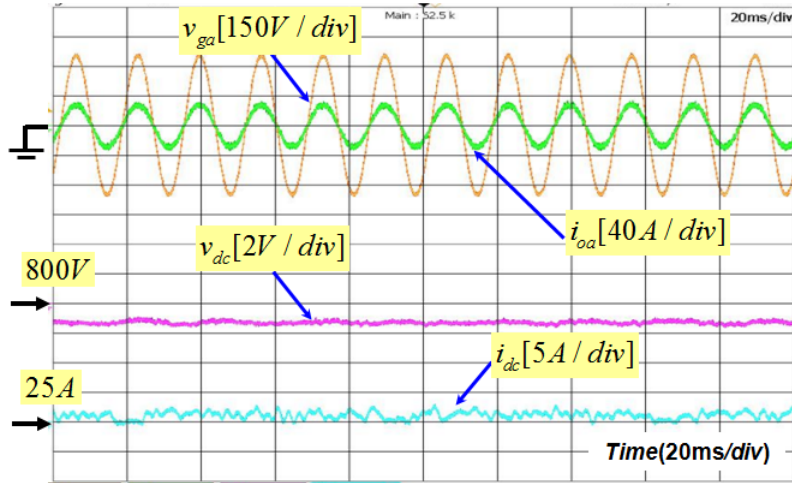


Fig. 78. Experimental waveforms of conventional control under balanced grid voltage.

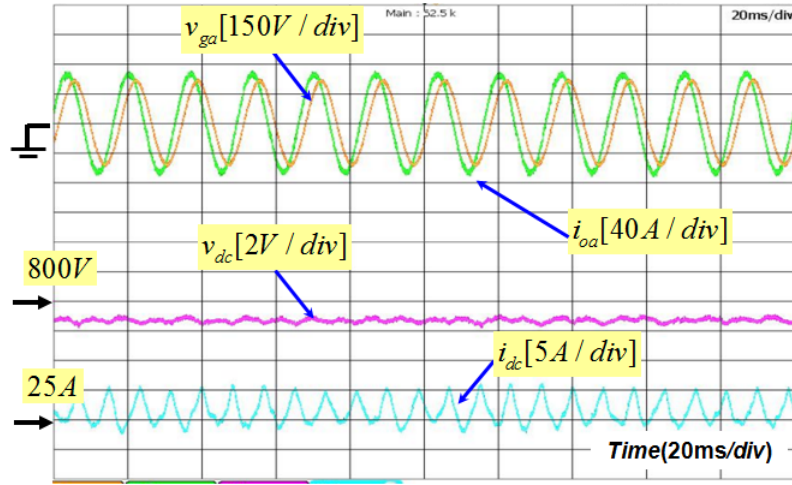


Fig. 79. Experimental waveforms of conventional control under unbalanced grid voltage.

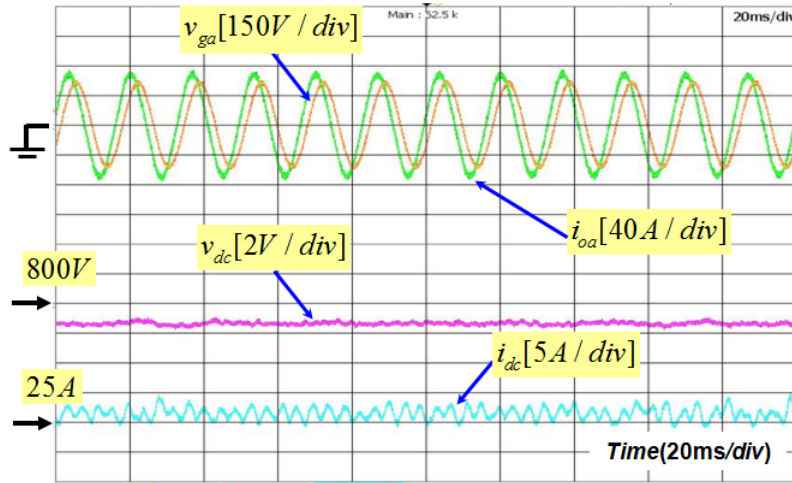


Fig. 80. Experimental waveforms of proposed control under unbalanced grid voltage.

5.6 Conclusion

This chapter proposed an enhanced control scheme of the *LCL* filter based DG inverter under grid voltage unbalance. The unbalanced grid voltage is reflected by a dc power oscillation to the dc source side. To minimize this oscillation, the double *d-q* frame current control schemes have been proposed. However, the conventional *d-q* frame current control was limited only in the case of the *L* filter based inverter. Therefore, the enhanced reference calculation was derived. By using new $\delta\text{-}\gamma$ transformation, the $\delta\text{-}\gamma$ frame current controller enables regulation of a constant current in the $\delta\text{-}\gamma$ axis as well as improvement of the bandwidth of the controller. With $\delta\text{-}\gamma$ axis current loops, the dc power oscillation was suppressed effectively. The proposed control strategy could reduce the impact of the renewable energy under grid voltage unbalance. As a result, constant dc power generation will also enhance the stability, and reliability of renewable energy sources. Simulation and experimental results verified that the proposed control method is able to minimize the dc power oscillation effectively under unbalanced operating conditions.

CHAPTER 6. SUMMARY AND FUTURE WORK

This dissertation proposed diverse control strategies for power electronic converters in order to improve the control performance of a dc-dc converter under different operation modes and a DG inverter under different operation modes and unbalanced operating conditions. It is summarized as follows:

1) A seamless control scheme for the dc-dc converter application with different operation modes is proposed to make mode transitions between DCM and CCM seamlessly by adding a mode tracker, and then the boost converter can smoothly operate by mixing the voltage and current control loop in both operation modes.

2) A seamless control scheme for the DG inverter application with different operation modes is proposed to make fast and stable mode transition technologies. The proposed approach is based on a current controller and a feedforward voltage controller to minimize the grid overvoltage and to improve the response time.

3) A modified reference frame based current control with improved current reference for the DG inverter application under grid voltage unbalance is proposed to minimize the dc voltage and dc current oscillations. With the proposed approach, the dc power oscillation is reduced effectively.

On the other hand, additional control approaches with proposed methods will be needed to improve the performance of proposed control strategies under other conditions. Future work is suggested as follows:

1) Proposed seamless control strategy of dc-dc converters is applied in the boost converter. This control scheme is able to be applied in other dc-dc converters such as buck converters. The dynamics analysis of CCM and DCM of the buck converter is necessary to apply to the buck converter.

2) Proposed seamless control strategy for DG inverters is considered with overvoltage condition. In order to extend the proposed control approach, the analysis of under voltage conditions will be needed to guarantee the control stability of the proposed seamless control.

3) The current reference calculation and unbalanced current control method of the *LCL* filter based DG inverter is considered under grid voltage unbalance without harmonics. However, the performance of the proposed unbalanced current controller is limited to reduce the current distortion under grid voltage

unbalance and harmonics. As future work, a multiple synchronous reference frame based current control scheme will be considered to enhance the performance of the unbalanced current control scheme.

PUBLICATIONS

1) Journal

- [1] Tai-Sik Hwang; Sung-Yeul Park; "Seamless Boost Converter Control Under the Critical Boundary Condition for a Fuel Cell Power Conditioning System," *IEEE Transactions on Power Electronics*, vol.27, no.8, pp.3616-3626, Aug. 2012
- [2] Tai-Sik Hwang; Tarca, M.J.; Sung-Yeul Park; "Dynamic Response Analysis of DC–DC Converter With Supercapacitor for Direct Borohydride Fuel Cell Power Conditioning System," *IEEE Transactions on Power Electronics*, vol.27, no.8, pp.3605-3615, Aug. 2012
- [3] Tai-Sik Hwang; Sung-Yeul Park, "A Seamless Control Strategy of a Distributed Generation Inverter for the Critical Load Safety Under Strict Grid Disturbances," *Power Electronics, IEEE Transactions on*, vol.28, no.10, pp.4780,4790, Oct. 2013

2) Conference

- [4] Tai-Sik Hwang; Sung-Yeul Park; , "Seamless boost converter control in critical boundary condition for fuel cell power conditioning system," *Energy Conversion Congress and Exposition (ECCE)*, 2011 IEEE , vol., no., pp.3641-3648, 17-22 Sept. 2011
- [5] Tai-Sik Hwang, Matthew J. Tarca and Sung-Yeul Park, "Dynamic Response Analysis of DC-DC Converter with Supercapacitor for Direct Borohydride Fuel Cell Power Conditioning System", 8th *International Conference on Power Electronics - ECCE Asia*, May 30-June 3, 2011, The Shilla Jeju, Korea
- [6] Matthew J. Tarca, Tai-Sik Hwang, and Sung-Yeul Park, "Design and Operation of an Autonomous Fuel Cell-Supercapacitor Power System for Portable Applications", 8th *International Conference on Power Electronics - ECCE Asia*, May 30-June 3, 2011, The Shilla Jeju, Korea
- [7] Tai-Sik Hwang; Sung-Yeul Park; , "A seamless control strategy of distributed generation inverter for critical load safety under strict grid disturbance," *Applied Power Electronics Conference and Exposition (APEC)*, 2012 Twenty-Seventh Annual IEEE , pp.254-261, 5-9 Feb. 2012
- [8] Tai-Sik Hwang; Sung-Yeul Park; "DC Power Ripple Minimization of LCL filter based Distributed Generation Inverter under Unbalanced Voltage Conditions," *Applied Power Electronics Conference and Exposition (APEC)*, 2013

APPENDIX A. MODELING OF THEREE PHASE *LCL* FILTER BASED DC-AC INVERTER

A.1 Dc-ac inverter modeling in the *abc* axis

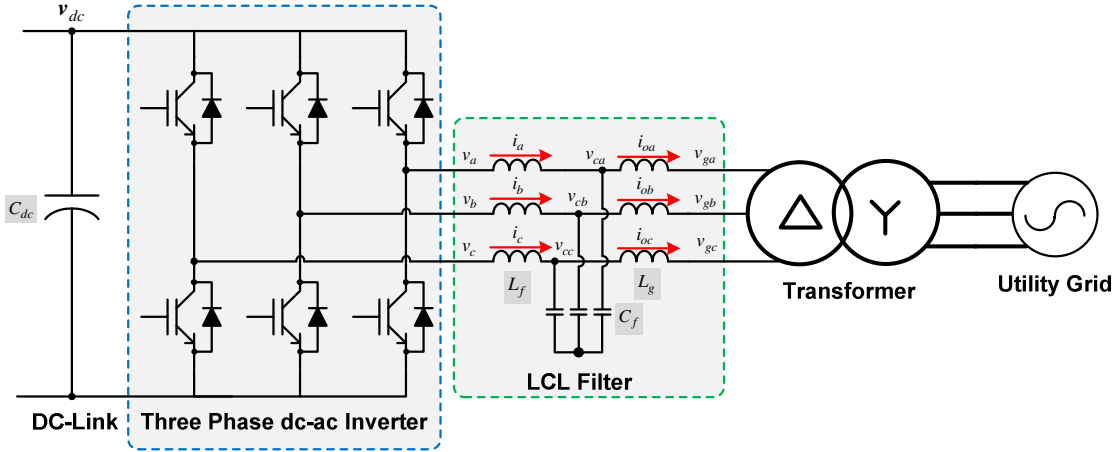


Fig. 81. Circuit diagram of three phase *LCL* filter based dc-ac inverter

Voltage and current equation in the *abc* axis are expressed as

$$\begin{cases} \mathbf{v}_{abc} = L_f \frac{d\mathbf{i}_{abc}}{dt} + \mathbf{v}_{cabc} \\ \mathbf{i}_{abc} = C_f \frac{d\mathbf{v}_{cabc}}{dt} + \mathbf{i}_{oabc} \\ \mathbf{v}_{cabc} = L_g \frac{d\mathbf{i}_{oabc}}{dt} + \mathbf{v}_{oabc} \end{cases} \quad (\text{A-1})$$

where L_f : the filter inductor, C_f : the filter capacitor, L_g : the grid inductor, $\mathbf{v}_{abc} = [v_a \ v_b \ v_c]^T$: the inverter voltage, $\mathbf{v}_{cabc} = [v_{ca} \ v_{cb} \ v_{cc}]^T$: the capacitor voltage, $\mathbf{v}_{gabc} = [v_{ga} \ v_{gb} \ v_{gc}]^T$: the grid voltage, $\mathbf{i}_{abc} = [i_a \ i_b \ i_c]^T$: the inverter current, and $\mathbf{i}_{oabc} = [i_{oa} \ i_{ob} \ i_{oc}]^T$: the output current.

A.2 α - β / d - q dc-ac inverter modeling using a vector notation

To transform the *abc* axis variables to the α - β axis variables, the α - β transformation matrix is given as

$$\bar{\mathbf{x}}_{\alpha\beta} = \frac{2}{3} \begin{bmatrix} 1 & -\frac{1}{2} & -\frac{1}{2} \\ 0 & \frac{\sqrt{3}}{2} & -\frac{\sqrt{3}}{2} \end{bmatrix} \bar{\mathbf{x}}_{abc} \quad (\text{A-2})$$

where $\bar{\mathbf{x}}_{\alpha\beta} = [x_\alpha \ x_\beta]^T$, and $\bar{\mathbf{x}}_{abc} = [x_a \ x_b \ x_c]^T$.

The α - β transformation matrix is invariant to time. By applying (A-2) in (A-1), the voltage and current equations in the α - β axis are expressed as

$$\begin{cases} \bar{\mathbf{v}}_{\alpha\beta} = L_f \frac{d\bar{\mathbf{i}}_{\alpha\beta}}{dt} + \bar{\mathbf{v}}_{c\alpha\beta} \\ \bar{\mathbf{i}}_{\alpha\beta} = C_f \frac{d\bar{\mathbf{v}}_{c\alpha\beta}}{dt} + \bar{\mathbf{i}}_{o\alpha\beta} \\ \bar{\mathbf{v}}_{c\alpha\beta} = L_g \frac{d\bar{\mathbf{i}}_{o\alpha\beta}}{dt} + \bar{\mathbf{v}}_{o\alpha\beta} \end{cases} \quad (\text{A-3})$$

where $\bar{\mathbf{v}}_{\alpha\beta} = [v_\alpha \ v_\beta]^T$: the α - β axis inverter voltage, $\bar{\mathbf{v}}_{c\alpha\beta} = [v_{c\alpha} \ v_{c\beta}]^T$: the α - β axis capacitor voltage, $\bar{\mathbf{v}}_{g\alpha\beta} = [v_{g\alpha} \ v_{g\beta}]^T$: the α - β axis grid voltage, $\bar{\mathbf{i}}_{\alpha\beta} = [i_\alpha \ i_\beta]^T$: the α - β axis inverter current, and $\bar{\mathbf{i}}_{o\alpha\beta} = [i_{o\alpha} \ i_{o\beta}]^T$: the α - β axis output current.

To transform the α - β axis variables to the d - q axis variables, the d - q transformation matrix is given as follows:

$$R_{dq}(\theta) = \begin{bmatrix} \cos \theta & \sin \theta \\ -\sin \theta & \cos \theta \end{bmatrix} \quad (\text{A-4})$$

$$\bar{\mathbf{x}}_{dq} = \begin{bmatrix} \cos \theta & \sin \theta \\ -\sin \theta & \cos \theta \end{bmatrix} \bar{\mathbf{x}}_{\alpha\beta} \quad (\text{A-5})$$

where $\bar{\mathbf{x}}_{dq} = [x_d \ x_q]^T$, and $\bar{\mathbf{x}}_{\alpha\beta} = [x_\alpha \ x_\beta]^T$.

The derivative of the α - β axis state vector with the d - q transformation matrix become as

$$R_{dq}(\theta) \frac{d\bar{\mathbf{x}}_{\alpha\beta}}{dt} = R_{dq}(\theta) \frac{d}{dt} \left(\underbrace{R_{dq}^{-1}(\theta) R_{dq}(\theta)}_{d-q \text{ vector}} \bar{\mathbf{x}}_{\alpha\beta} \right) = R_{dq}(\theta) \frac{d}{dt} \left(R_{dq}^{-1}(\theta) \bar{\mathbf{x}}_{dq} \right) \quad (\text{A-6})$$

$$R_{dq}(\theta) \frac{d}{dt} (R_{dq}^{-1}(\theta) \vec{x}_{dq}) = R_{dq}(\theta) \frac{d}{dt} (R_{dq}^{-1}(\theta)) \vec{x}_{dq} + \frac{d\vec{x}_{dq}}{dt} \quad (\text{A-7})$$

The derivative of the inverse d - q transformation matrix is expressed as

$$\frac{d}{dt} (R_{dq}^{-1}(\theta)) = \omega \begin{bmatrix} -\sin \theta & -\cos \theta \\ \cos \theta & -\sin \theta \end{bmatrix} \quad (\text{A-8})$$

Then, we can obtain as follows:

$$R_{dq}(\theta) \frac{d}{dt} (R_{dq}^{-1}(\theta)) = \omega \begin{bmatrix} \cos \theta & \sin \theta \\ -\sin \theta & \cos \theta \end{bmatrix} \begin{bmatrix} -\sin \theta & -\cos \theta \\ \cos \theta & -\sin \theta \end{bmatrix} = \omega \begin{bmatrix} 0 & -1 \\ 1 & 0 \end{bmatrix} \quad (\text{A-9})$$

We can define the following matrix as

$$J = \begin{bmatrix} 0 & -1 \\ 1 & 0 \end{bmatrix} \quad (\text{A-10})$$

Therefore, (A.6) is given as

$$R_{dq}(\theta) \frac{d\vec{x}_{\alpha\beta}}{dt} = \frac{d\vec{x}_{dq}}{dt} + \omega J \vec{x}_{dq} \quad (\text{A-11})$$

From (A-11) and (A-3), the voltage and current equations in the d - q axis are expressed as

$$\begin{cases} \vec{v}_{dq} = L_f \frac{d\vec{i}_{dq}}{dt} + J \omega \vec{i}_{dq} + \vec{v}_{cdq} \\ \vec{i}_{dq} = C_f \frac{d\vec{v}_{cdq}}{dt} + J \omega \vec{v}_{cdq} + \vec{i}_{odq} \\ \vec{v}_{cdq} = L_g \frac{d\vec{i}_{odq}}{dt} + J \omega \vec{i}_{odq} + \vec{v}_{o\alpha\beta} \end{cases} \quad (\text{A-12})$$

A.3 α - β / d - q dc-ac inverter modeling using a complex space vector notation

To transform the abc axis variables to the α - β axis variables, the α - β transformation matrix is given as

$$\mathbf{x}_{\alpha\beta} = x_\alpha + jx_\beta = \frac{2}{3} (x_a + x_b e^{j2\pi/3} + x_c e^{j4\pi/3}) \quad (\text{A-13})$$

$$\begin{cases} \mathbf{v}_{\alpha\beta} = L_f \frac{d\mathbf{i}_{\alpha\beta}}{dt} + \mathbf{v}_{c\alpha\beta} \\ \mathbf{i}_{c\alpha\beta} = C_f \frac{d\mathbf{v}_{c\alpha\beta}}{dt} + \mathbf{i}_{o\alpha\beta} \\ \mathbf{v}_{c\alpha\beta} = L_g \frac{d\mathbf{i}_{o\alpha\beta}}{dt} + \mathbf{v}_{o\alpha\beta} \end{cases} \quad (\text{A.14})$$

To transform the α - β axis variables to the d - q axis variables, the d - q transformation operator is given as

$$R_{dq}(\theta) = e^{-j\theta} \quad (\text{A.15})$$

$$\mathbf{x}_{dq} = e^{-j\theta} \mathbf{x}_{\alpha\beta} \quad (\text{A.16})$$

where $\mathbf{x}_{dq} = x_d + jx_q$.

The derivative of the α - β axis state vector with the d - q transformation operator become as

$$e^{-j\theta} \frac{d\mathbf{x}_{\alpha\beta}}{dt} = e^{-j\theta} \frac{d}{dt} \left(e^{j\theta} \underbrace{e^{-j\theta} \mathbf{x}_{\alpha\beta}}_{d-q \text{ vector}} \right) = e^{-j\theta} \frac{d}{dt} (e^{j\theta} \mathbf{x}_{dq}) \quad (\text{A.17})$$

$$e^{-j\theta} \frac{d}{dt} (e^{j\theta} \mathbf{x}_{dq}) = e^{-j\theta} \frac{d}{dt} (e^{j\theta}) \mathbf{x}_{dq} + \frac{d\mathbf{x}_{dq}}{dt} \quad (\text{A.18})$$

Then, we can obtain as follows:

$$e^{-j\theta} \frac{d}{dt} (e^{j\theta}) = j\omega \quad (\text{A.19})$$

Therefore, (A.14) is given as

$$e^{-j\theta} \frac{d\mathbf{x}_{\alpha\beta}}{dt} = \frac{d\mathbf{x}_{dq}}{dt} + j\omega \mathbf{x}_{dq} \quad (\text{A.20})$$

From (A-20) and (A-14), the voltage and current equations in the d - q axis are expressed as

$$\begin{cases} \mathbf{v}_{dq} = L_f \frac{d\mathbf{i}_{dq}}{dt} + j\omega \mathbf{i}_{dq} + \mathbf{v}_{cdq} \\ \mathbf{i}_{dq} = C_f \frac{d\mathbf{v}_{cdq}}{dt} + j\omega \mathbf{v}_{cdq} + \mathbf{i}_{odq} \\ \mathbf{v}_{cdq} = L_g \frac{d\mathbf{i}_{odq}}{dt} + j\omega \mathbf{i}_{odq} + \mathbf{v}_{o\alpha\beta} \end{cases} \quad (\text{A.21})$$

From either (A.12) or (A.21), the stat space equation in the d - q axis for the LCL filter based dc-ac inverter is given as

$$\frac{d\mathbf{x}}{dt} = A\mathbf{x} + B\mathbf{u} + E\mathbf{w} \quad (\text{A.21})$$

where $\mathbf{x} = [i_d \quad i_q \quad v_{cd} \quad v_{cq} \quad i_{od} \quad i_{oq}]^T$: the state variables, $\mathbf{u} = [v_d \quad v_q]^T$: the control input,

$\mathbf{w} = [v_{gd} \quad v_{gq}]^T$: the disturbance,

$$A = \begin{bmatrix} 0 & -\omega/L_f & 1 & 0 & 0 & 0 \\ \omega/L_f & 0 & 0 & 1 & 0 & 0 \\ 0 & 0 & 0 & -\omega/C_f & 1 & 0 \\ 0 & 0 & \omega/C_f & 0 & 0 & 1 \\ 0 & 0 & 0 & 0 & 0 & -\omega/L_g \\ 0 & 0 & 0 & 0 & \omega/L_g & 0 \end{bmatrix},$$

$$B = \begin{bmatrix} 1/L_f & 0 \\ 0 & 1/L_f \\ 0 & 0 \\ 0 & 0 \\ 0 & 0 \\ 0 & 0 \end{bmatrix}, \text{ and } E = \begin{bmatrix} 1/L_g & 0 \\ 0 & 1/L_g \\ 0 & 0 \\ 0 & 0 \\ 0 & 0 \\ 0 & 0 \end{bmatrix}.$$

APPENDIX B. GENERAL COMPLEX SPACE VECTOR

A general space vector, $\mathbf{x}_{\alpha\beta}$, in the α - β axis is express with a summation of the n th order positive-sequence space vectors, $\mathbf{x}_{\alpha\beta}^{+n}$, in the α - β axis and the n th order negative-sequence space vectors, $\mathbf{x}_{\alpha\beta}^{-n}$, in the α - β axis. And it is expressed by a summation of the n th order positive-sequence d - q axis space vectors, \mathbf{x}_{dq}^{+n} , with $e^{jn\theta}$ and the n th order negative-sequence d - q space vectors, \mathbf{x}_{dq}^{-n} , with respect to $e^{-jn\theta}$. The general space vector is written as

$$\begin{aligned}\mathbf{x}_{\alpha\beta} &= \sum_{n=1,2,3,\dots} (\mathbf{x}_{\alpha\beta}^{+n} + \mathbf{x}_{\alpha\beta}^{-n}) \\ &= \sum_{n=1,2,3,\dots} (e^{jn\theta} \mathbf{x}_{dq}^{+n} + e^{-jn\theta} \mathbf{x}_{dq}^{-n})\end{aligned}\tag{B-1}$$

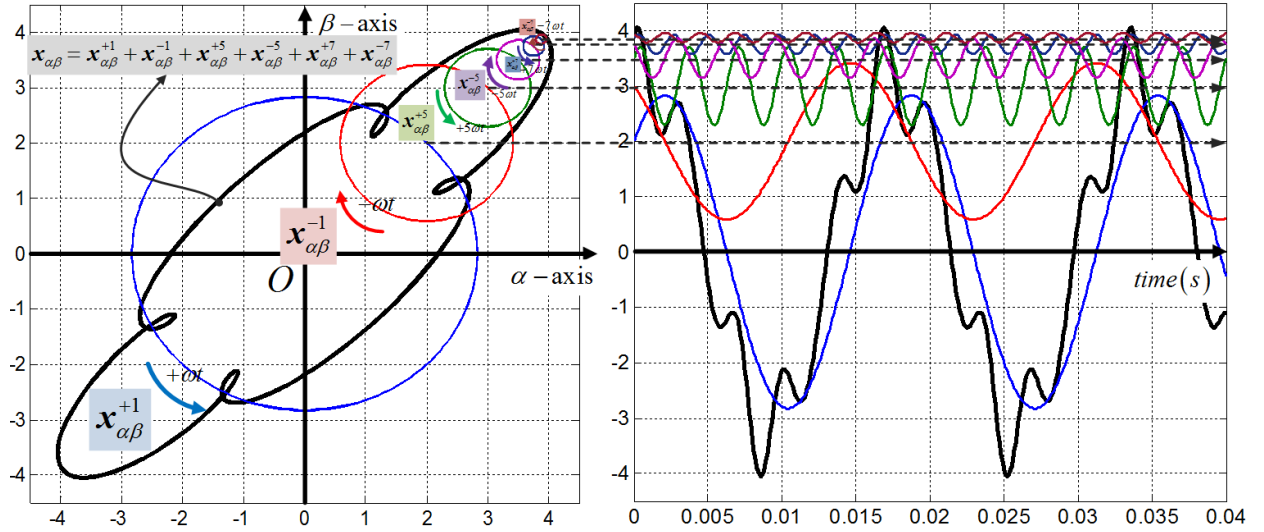


Fig. 82. Loci of space vectors in the α - β axis and their waveforms in time domain.

Fig. 82 shows the loci of the n th order space vectors in the α - β axis and their waveforms in time domain.

APPENDIX C. SYMMETRICAL COORDINATE ANALYSIS

Based on the conventional symmetrical coordinate method [98], there are *skew-symmetric* transformation matrices to extract the positive-sequence components and the negative-sequence components in the α - β axis, i.e.

$$\begin{bmatrix} T_{\alpha\beta}^+ \end{bmatrix} = \frac{1}{2} \begin{bmatrix} 1 & -\hat{q} \\ \hat{q} & 1 \end{bmatrix}, \text{ and } \begin{bmatrix} T_{\alpha\beta}^- \end{bmatrix} = \frac{1}{2} \begin{bmatrix} 1 & \hat{q} \\ -\hat{q} & 1 \end{bmatrix} \quad (\text{C-1})$$

where $\hat{q} = e^{-j\frac{\pi}{2}}$ is a 90° -*lagging phase-shifting operator* applied on the time domain to obtain an in-quadrature version of the input waveforms [98].

The phase-shifting operator, \hat{q} , is a mathematical operator to make the phase shifting of the input waveform as follows:

$$\hat{q}x_n = x_n \left(n\omega t - \frac{\pi}{2} \right), \quad n = 1, 2, 3, \dots \quad (\text{C-2})$$

From (C-1), skew-symmetric operators with the phase-shifting operator are defined as

$$T_{\alpha\beta}^+ = \frac{1}{2}(1 + j\hat{q}), \text{ and } T_{\alpha\beta}^- = \frac{1}{2}(1 - j\hat{q}) \quad (\text{C-3})$$

By applying the skew-symmetric operators, a summation of the positive-sequence space vectors and a summation of the negative-sequence space vectors are extracted as

$$\begin{cases} T_{\alpha\beta}^+ x_{\alpha\beta} = \sum_{n=1,2,3,\dots} x_{dq}^{+n} e^{+jn\theta} \\ T_{\alpha\beta}^- x_{\alpha\beta} = \sum_{n=1,2,3,\dots} x_{dq}^{-n} e^{-jn\theta} \end{cases} \quad (\text{C-4})$$

A band pass operator is defined as follows:

$$\mathbf{G}^n \mathbf{x}^k = \begin{cases} \mathbf{x}^n, & \text{if } n = k \\ 0, & \text{if } n \neq k \end{cases} \quad (\text{C-5})$$

Using the band pass operator, the n th-order positive- and negative- sequence space vectors in the α - β axis are expressed as

$$\begin{cases} \mathbf{G}^n [\mathbf{T}_{\alpha\beta}^+ \mathbf{x}_{\alpha\beta}] = \mathbf{x}_{dq}^{+n} e^{jn\theta} \\ \mathbf{G}^n [\mathbf{T}_{\alpha\beta}^- \mathbf{x}_{\alpha\beta}] = \mathbf{x}_{dq}^{-n} e^{-jn\theta} \end{cases} \quad (\text{C-6})$$

where $n = 1, 2, 3, \dots$.

Using the d - q transformation, the n th-order positive- and negative- sequence space vectors in the d - q axis can be extracted as follows:

$$\begin{cases} \mathbf{x}_{dq}^{+n} = e^{-jn\theta} \hat{\mathbf{x}}_{\alpha\beta}^{+n} \\ \mathbf{x}_{dq}^{-n} = e^{jn\theta} \hat{\mathbf{x}}_{\alpha\beta}^{-n} \end{cases} \quad (\text{C-7})$$

These results are the representation of the complex space vector to compute *the positive- and negative-sequence components based on multiple d - q frames.*

APPENDIX D. ROTATION OF AXES [135]

A general equation of the conic is given as

$$Ax^2 + Bxy + Cy^2 + Dx + Ey + F = 0 \quad (\text{D-1})$$

To eliminate the xy -term in (D-1), a procedure called *rotation of axes* is used as follows.

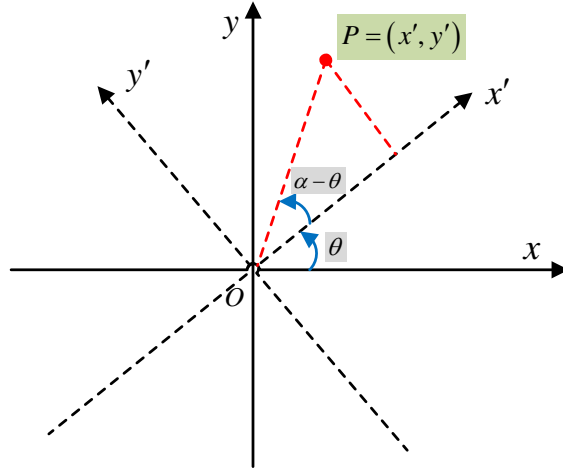


Fig. 83. Rotation of axes

From Fig. 83, using the formulas for the sine and cosine of the difference of two angles, we can obtain as

$$\begin{cases} x' = r \cos(\alpha - \theta) = r \cos \alpha \cos \theta + r \sin \alpha \sin \theta = x \cos \theta + y \sin \theta \\ y' = r \sin(\alpha - \theta) = r \sin \alpha \cos \theta - r \cos \alpha \sin \theta = y \cos \theta - x \sin \theta \end{cases} \quad (\text{D-2})$$

where , $x = r \cos \alpha$, and $y = r \sin \alpha$.

Solving (D-2), the coefficients of the new equation are obtained by making the substitutions

$$\begin{cases} x = x' \cos \theta - y' \sin \theta \\ y = x' \sin \theta + y' \cos \theta \end{cases} \quad (\text{D-3})$$

By substituting (D-3) into (D-1), we can obtain as follows:

$$\begin{cases} A' = A \cos^2 \theta + B \cos \theta \sin \theta + C \sin^2 \theta \\ C' = A \sin^2 \theta - B \cos \theta \sin \theta + C \cos^2 \theta \\ D' = D \cos \theta + E \sin \theta \\ E' = -D \sin \theta + E \cos \theta \\ F' = F \end{cases} \quad (\text{D-4})$$

In order to eliminate the x' and y' terms, we need to choose θ such that $B' = 0$, as follows:

$$\begin{aligned} B' &= 2(C - A) \sin \theta \cos \theta + B(\cos^2 \theta - \sin^2 \theta) \\ &= (C - A) \sin 2\theta + B \cos 2\theta \\ &= B(\sin 2\theta) \left(\frac{C - A}{B} + \cot 2\theta \right) = 0 \end{aligned} \quad (\text{D-5})$$

where $\sin 2\theta \neq 0$.

If $B = 0$, there is no rotation, because the xy -term is included in (D-1), In the case of $B \neq 0$, we have the condition to make $B' = 0$ as follows:

$$\cot 2\theta = \frac{A - C}{B}, \quad B \neq 0 \quad (\text{D-6})$$

By rotating the coordinate axes in (D-3) through the angle, θ , in (D-6), a *standard equation* of the conic is given as

$$A'x^2 + C'y^2 + D'x + E'y + F' = 0 \quad (\text{D-7})$$

REFERENCES

- [1] X. Zhou, S. -Y. Park, "Design and analysis of a direct borohydride fuel cell dc-dc converter for portable applications," *Proc. of ASME 2010 8th international fuel cell science 7 technology conference*, 14-16 Jun. 2010, Brooklyn NY.
- [2] Itoh, J.-i.; Hayashi, F.; , "Ripple Current Reduction of a Fuel Cell for a Single-Phase Isolated Converter Using a DC Active Filter With a Center Tap," *Power Electronics, IEEE Transactions on* , vol.25, no.3, pp.550-556, March 2010
- [3] Changrong Liu; Jih-Sheng Lai; , "Low Frequency Current Ripple Reduction Technique With Active Control in a Fuel Cell Power System With Inverter Load," *Power Electronics, IEEE Transactions on* , vol.22, no.4, pp.1429-1436, July 2007
- [4] Kyung-Won Suh; Stefanopoulou, A.G.; , "Coordination of Converter and Fuel Cell Controllers," *Intelligent Control*, 2005. Proceedings of the 2005 IEEE International Symposium on, Mediterrean Conference on Control and Automation, pp.563-568, 27-29 June 2005.
- [5] Qian, Z.; Abdel-Rahman, O.; Batarseh, I.; , "An Integrated Four-Port DC/DC Converter for Renewable Energy Applications," *Power Electronics, IEEE Transactions on* , vol.25, no.7, pp.1877-1887, July 2010.
- [6] Samosir, A.S.; Yatim, A.H.M.; , "Implementation of Dynamic Evolution Control of Bidirectional DC-DC Converter for Interfacing Ultracapacitor Energy Storage to Fuel-Cell System," *Industrial Electronics, IEEE Transactions on* , vol.57, no.10, pp.3468-3473, Oct. 2010
- [7] Liu, W.; Chen, J.; Liang, T.; Lin, R.; Liu, C.; , "Analysis, Design, and Control of Bidirectional Cascaded Configuration for a Fuel Cell Hybrid Power System," *Power Electronics, IEEE Transactions on* , vol.25, no.6, pp.1565-1575, June 2010
- [8] Ke Jin; Xinbo Ruan; Mengxiong Yang; Min Xu; , "A Hybrid Fuel Cell Power System," *Industrial Electronics, IEEE Transactions on* , vol.56, no.4, pp.1212-1222, April 2009
- [9] Wei-Shih Liu; Jiann-Fuh Chen; Tsorng-Juu Liang; Ray-Lee Lin; , "Multicascoded Sources for a High-Efficiency Fuel-Cell Hybrid Power System in High-Voltage Application," *Power Electronics, IEEE Transactions on* , vol.26, no.3, pp.931-942, March 2011
- [10] Harfman-Todorovic, M.; Chellappan, M.; Palma, L.; Enjeti, P.; , "The role of supercapacitors in designing fuel cell powered portable applications," *Power Electronics Specialists Conference, 2008. PESC 2008. IEEE*, pp.2465-2472, 15-19 June 2008
- [11] Itoh, J.-i.; Hayashi, F.; , "Ripple Current Reduction of a Fuel Cell for a Single-Phase Isolated Converter Using a DC Active Filter With a Center Tap," *Power Electronics, IEEE Transactions on* , vol.25, no.3, pp.550-556, March 2010

- [12] Todorovic, M.H.; Palma, L.; Enjeti, P.; , "Design of a wide input range DC-DC converter with a robust power control scheme suitable for fuel cell power conversion," *Applied Power Electronics Conference and Exposition, 2004. APEC '04. Nineteenth Annual IEEE* , vol.1, no., pp. 374- 379 Vol.1, 2004
- [13] Jonq-Chin Hwang; Li-Hsiu Chen; Sheng-Nian Yeh; , "A three-leg fuel-cell boost converter with novel digital-signal-processor based pulse-width modulation," *TENCON 2007 - 2007 IEEE Region 10 Conference*, pp.1-4, Oct. 30 2007-Nov. 2 2007
- [14] Palma, L.; Harfman-Todorovic, M.; Enjeti, P.; Sewan Choi; , "Analysis of DC-DC Converter Stability in Fuel Cell Powered Portable Electronic Systems," *Power Electronics Specialists Conference, 2006. PESC '06. 37th IEEE* , pp.1-6, 18-22 June 2006
- [15] Kenarangui, Y.; Wang, S.; Fahimi, B.; , "On the impact of fuel cell system response on power electronics converter design," *Vehicle Power and Propulsion Conference, 2006. VPPC '06. IEEE*, pp. 6-8 Sept. 2006
- [16] Van de Sype, D.M.; Koen De Gusseme; Van den Bossche, A.P.M.; Melkebeek, J.A.; , "Duty-ratio feedforward for digitally controlled boost PFC converters," *Industrial Electronics, IEEE Transactions on* , vol.52, no.1, pp. 108- 115, Feb. 2005
- [17] Van de Sype, D.M.V.; De Gusseme, K.; Van den Bossche, A.P.; Melkebeek, J.A.; , "Duty-ratio feedforward for digitally controlled boost PFC converters," *Applied Power Electronics Conference and Exposition, 2003. APEC '03. Eighteenth Annual IEEE* , vol.1, no., pp. 396- 402 vol.1, 9-13 Feb. 2003,
- [18] Jinbo Liu; Wenlong Ming; Fanghong Gao; , "A new control strategy for improving performance of boost DC/DC converter based on input-output feedback linearization," *Intelligent Control and Automation (WCICA), 2010 8th World Congress on* , pp.2439-2444, 7-9 July 2010
- [19] Chen, Z.; Gao, W.; Hu, J.; Ye, X.; , "Closed-Loop Analysis and Cascade Control of a Nonminimum Phase Boost Converter," *Power Electronics, IEEE Transactions on* , vol.26, no.4, pp.1237-1252, April 2011
- [20] Wenlong Ming; Jinbo Liu; , "A new experimental study of input-output feedback linearization based control of Boost type DC/DC converter," *Industrial Technology (ICIT), 2010 IEEE International Conference on* , pp.685-689, 14-17 March 2010
- [21] Dingxin Shuai; Yunxiang Xie; Xiaogang Wang; , "The research of input-output linearization and stabilization analysis of internal dynamics on the CCM Boost converter," *Electrical Machines and Systems, 2008. ICEMS 2008. International Conference on* , pp.1860-1864, 17-20, Oct. 2008

- [22] Morroni, J.; Corradini, L.; Zane, R.; Maksimovic, D.; , "Adaptive Tuning of Switched-Mode Power Supplies Operating in Discontinuous and Continuous Conduction Modes," *Power Electronics, IEEE Transactions on* , vol.24, no.11, pp.2603-2611, Nov. 2009
- [23] Jian Sun; Mitchell, D.M.; Greuel, M.F.; Krein, P.T.; Bass, R.M.; , "Averaged modeling of PWM converters operating in discontinuous conduction mode," *Power Electronics, IEEE Transactions on* , vol.16, no.4, pp.482-492, Jul 2001
- [24] S. Cuk and R. D. Middlebrook, "A general unified approach to modeling switching DC-to-DC converters in discontinuous conduction mode," in *Proc. IEEE PESC'77*, 1977, pp. 36–57.
- [25] R. Tymerski and V. Vorperian, "Generation, classification and analysis of switched-mode DC-to-DC converters by the use of converter cells," in *Proc. INTELEC'86*, Oct. 1986, pp. 181–195.
- [26] Maksimovic, D.; Cuk, S.; , "A unified analysis of PWM converters in discontinuous modes," *Power Electronics, IEEE Transactions on* , vol.6, no.3, pp.476-490, Jul 1991
- [27] Vorperian, V.; , "Simplified analysis of PWM converters using model of PWM switch. II. Discontinuous conduction mode," *Aerospace and Electronic Systems, IEEE Transactions on* , vol.26, no.3, pp.497-505, May 1990
- [28] Maksimovic, D.; Zane, R.; , "Small-Signal Discrete-Time Modeling of Digitally Controlled PWM Converters," *Power Electronics, IEEE Transactions on* , vol.22, no.6, pp.2552-2556, Nov. 2007
- [29] Bryant, B.; Kazimierczuk, M.K.; , "Open-loop power-stage transfer functions relevant to current-mode control of boost PWM converter operating in CCM," *Circuits and Systems I: Regular Papers, IEEE Transactions on* , vol.52, no.10, pp. 2158- 2164, Oct. 2005
- [30] Davoudi, A.; Jatskevich, J.; De Rybel, T.; , "Numerical state-space average-value modeling of PWM DC-DC converters operating in DCM and CCM," *Power Electronics, IEEE Transactions on* , vol.21, no.4, pp.
- [31] Sreekumar, C.; Agarwal, V.; , "A Hybrid Control Algorithm for Voltage Regulation in DC–DC Boost Converter," *Industrial Electronics, IEEE Transactions on* , vol.55, no.6, pp.2530-2538, June 2008
- [32] Tripathi, R.K.; Das, S.P.; Dubey, G.K.; , "Mixed-mode operation of boost switch-mode rectifier for wide range of load variations," *Power Electronics, IEEE Transactions on* , vol.17, no.6, pp. 999-1009, Nov 2002
- [33] Lim, L. S.; Khambadkone, A. M.; , "A Simple Digital DCM Control Scheme for Boost PFC Operating in Both CCM and DCM," *Industry Applications, IEEE Transactions on* , vol.47, no.4, pp.1802-1812, July-Aug. 2011

- [34] Abu Qahouq, J.A.; , "Control Scheme for Sensorless Operation and Detection of CCM and DCM Operation Modes in Synchronous Switching Power Converters," *Power Electronics, IEEE Transactions on* , vol.25, no.10, pp.2489-2495, Oct. 2010
- [35] Zhonghui Bing; Xiong Du; Jian Sun; , "Generalization of a nonlinear average current control method for CCM and DCM operation," *Applied Power Electronics Conference and Exposition, 2008. APEC 2008. Twenty-Third Annual IEEE* , vol., no., pp.51-57, 24-28 Feb. 2008
- [36] Kancherla, S.; Tripathi, R.K.; , "Nonlinear average current mode control for a DC-DC buck converter in continuous and discontinuous conduction modes," *TENCON 2008 - 2008 IEEE Region 10 Conference* , vol., no., pp.1-6, 19-21 Nov. 2008
- [37] Cheung, V.S.; Chung, H.S.; Lo, A.W.L.; , "Derivation of a nonlinear output capacitor current programming technique applicable for a buck converter operating in CCM and DCM," *Energy Conversion Congress and Exposition (ECCE), 2010 IEEE* , vol., no., pp.1979-1986, 12-16 Sept. 2010
- [38] Ting-Ting Song; Chung, H.S.-h.; , "Boundary Control of Boost Converters Using State-Energy Plane," *Power Electronics, IEEE Transactions on* , vol.23, no.2, pp.551-563, March 2008
- [39] Huber, L.; Irving, B.T.; Jovanovic, M.M.; , "Closed-Loop Control Methods for Interleaved DCM/CCM Boundary Boost PFC Converters," *Applied Power Electronics Conference and Exposition, 2009. APEC 2009. Twenty-Fourth Annual IEEE* , vol., no., pp.991-997, 15-19 Feb. 2009
- [40] Huber, L.; Irving, B.T.; Jovanovic, M.M.; , "Open-Loop Control Methods for Interleaved DCM/CCM Boundary Boost PFC Converters," *Power Electronics, IEEE Transactions on* , vol.23, no.4, pp.1649-1657, July 2008
- [41] Huber, L.; Irving, B.T.; Jovanovic, M.M.; , "Review and Stability Analysis of PLL-Based Interleaving Control of DCM/CCM Boundary Boost PFC Converters," *Power Electronics, IEEE Transactions on* , vol.24, no.8, pp.1992-1999, Aug. 2009
- [42] Jian-Min Wang; Sen-Tung Wu; Yanfeng Jiang; Huang-Jen Chiu; , "A Dual-Mode Controller for the Boost PFC Converter," *Industrial Electronics, IEEE Transactions on* , vol.58, no.1, pp.369-372, Jan. 2011
- [43] Annual Energy Outlook 2011: With Projections to 2035, DOE/EIA-0383(2011), April 2011.
- [44] M. Kazmierkowski, R. Krishnan, and F. Blaabjerg, *Control in Power Electronics—Selected Problems*. New York: Academic, 2002.
- [45] R. Teodorescu, F. Iov, and F. Blaabjerg, "Flexible development and test system for 11 kW wind turbine," in *Proc. IEEE PESC*, 2003, vol. 1, pp. 67–72.
- [46] E. Twining and D. G. Holmes, "Grid current regulation of a three-phase voltage source inverter with an LCL input filter," *IEEE Trans. Power Electron.*, vol. 18, no. 3, pp. 888–895, May 2003.

- [47] S. Fukuda and T. Yoda, "A novel current-tracking method for active filters based on a sinusoidal internal model," *IEEE Trans. Ind. Electron.*, vol. 37, no. 3, pp. 888–895, 2001.
- [48] X. Yuan, W. Merk, H. Stemmler, and J. Allmeling, "Stationary-frame generalized integrators for current control of active power filters with zero steady-state error for current harmonics of concern under unbalanced and distorted operating conditions," *IEEE Trans. Ind. Appl.*, vol. 38, no. 2, pp. 523–532, Mar./Apr. 2002.
- [49] R. Teodorescu and F. Blaabjerg, "Proportional-resonant controllers. A new breed of controllers suitable for grid-connected voltage-source converters," in *Proc. OPTIM*, 2004, vol. 3, pp. 9–14.
- [50] D. Zmood and D. G. Holmes, "Stationary frame current regulation of PWM inverters with zero steady-state error," *IEEE Trans. Power Electron.*, vol. 18, no. 3, pp. 814–822, May 2003.
- [51] M. Ciobotaru, R. Teodorescu, and F. Blaabjerg, "Control of single-stage single-phase PV inverter," in *Proc. PELINCEC*, 2005, CDROM.
- [52] José M. Espí Huerta, Jaime Castelló-Moreno, Jonatan Roberto Fischer, and Rafael García-Gil, "Synchronous Reference Frame Robust Predictive Current Control for Three-Phase Grid-Connected Inverters", *IEEE TRANSACTIONS ON INDUSTRIAL ELECTRONICS*, VOL. 57, NO. 3, MARCH 2010
- [53] Jaime Castelló Moreno, José M. Espí Huerta, Rafael García Gil, and Sergio Alejandro González, "A Robust Predictive Current Control for Three-Phase Grid-Connected Inverters", *IEEE TRANSACTIONS ON INDUSTRIAL ELECTRONICS*, VOL. 56, NO. 6, JUNE 2009
- [54] Q. Zeng and L. Chang, "An advanced SVPWM-based predictive current controller for three-phase inverters in distributed generation systems," *IEEE Trans. Ind. Electron.*, vol. 55, no. 3, pp. 1235–1246, Mar. 2008.
- [55] Y.-R. Mohamed and E. El-Saadany, "An improved deadbeat current control scheme with a novel adaptive self-tuning load model for a three-phase PWM voltage-source inverter," *IEEE Trans. Ind. Electron.*, vol. 54, no. 2, pp. 747–759, Apr. 2007.
- [56] J. Rodriguez, J. Pontt, C. A. Silva, P. Correa, P. Lezana, P. Cortes, and U. Ammann, "Predictive current control of a voltage source inverter," *IEEE Trans. Ind. Electron.*, vol. 54, no. 1, pp. 495–503, Feb. 2007.
- [57] H. Abu-Rub, J. Guzinski, Z. Krzeminski, and H. Toliyat, "Predictive current control of voltage-source inverters," *IEEE Trans. Ind. Electron.*, vol. 51, no. 3, pp. 585–593, Jun. 2004.
- [58] G. Bode, P. C. Loh, M. Newman, and D. Holmes, "An improved robust predictive current regulation algorithm," *IEEE Trans. Ind. Appl.*, vol. 41, no. 6, pp. 1720–1733, Nov./Dec. 2005.
- [59] P. Mattavelli, "An improved deadbeat control for ups using disturbance observers," *IEEE Trans. Ind. Electron.*, vol. 52, no. 1, pp. 206–212, Feb. 2005.

- [60] Summers and R. Betz, "Dead-time issues in predictive current control," *IEEE Trans. Ind. Appl.*, vol. 40, no. 3, pp. 835–844, May/Jun. 2004.
- [61] Y.-R. Mohamed and E. El-Saadany, "A control scheme for PWM voltage source distributed-generation inverters for fast load-voltage regulation and effective mitigation of unbalanced voltage disturbances," *IEEE Trans. Ind. Electron.*, vol. 55, no. 5, pp. 2072–2084, May 2008.
- [62] Y.-R. Mohamed and E. El-Saadany, "An improved deadbeat current control scheme with a novel adaptive self-tuning load model for a three-phase PWM voltage-source inverter," *IEEE Trans. Ind. Electron.*, vol. 54, no. 2, pp. 747–759, Apr. 2007.
- [63] Y. Dote and R. G. Hoft, *Intelligent Control—Power Electronic Systems*. Oxford, U.K.: Oxford Univ. Press, 1998.
- [64] M. J. Tyan, W. E. Brumsickle, and R. D. Lorenz, "Control topology options for single-phase UPS inverters," *IEEE Trans. Ind. Appl.*, vol. 33, no. 2, pp. 493–500, Mar./Apr. 1997.
- [65] U. B. Jensen, P. N. Enjeti, and F. Blaabjerg, "A new space vector based control method for UPS systems powering nonlinear and unbalanced loads," in *Proc. IEEE Applied Power Electronics Conf. (APEC'00)*, New Orleans, LA, Feb. 2000, pp. 895–901.
- [66] T. Ito and S. Kawauchi, "Microprocessor-based robust digital control for UPS with three-phase PWM inverter," *IEEE Trans. Power Electron.*, vol. 10, no. 2, pp. 196–203, Mar. 1995.
- [67] Y. Y. Tzou, R. S. Ou, S. L. Jung, and M. Y. Chang, "High-performance programmable AC power source with low harmonic distortion using DSP-based repetitive control technique," *IEEE Trans. Power Electron.*, vol. 12, no. 4, pp. 715–725, Jul. 1997.
- [68] T. Haneyoshi, A. Kawamura, and R. G. Hoft, "Waveform compensation of PWM inverter with cyclic fluctuating loads," *IEEE Trans. Ind. Appl.*, vol. 24, no. 4, pp. 582–589, Jul./Aug. 1988.
- [69] A. Kawamura, T. Haneyoshi, and R. G. Hoft, "Deadbeat controlled PWM inverter with parameter estimation using only voltage sensor," *IEEE Trans. Power Electron.*, vol. 3, no. 2, pp. 118–124, Apr. 1988.
- [70] T. Kawabata, T. Miyashita, and Y. Yamamoto, "Dead beat control of three phase PWM inverter," *IEEE Trans. Power Electron.*, vol. 5, no. 1, pp. 21–28, Jan. 1990.
- [71] T. Yokoyama and A. Kawamura, "Disturbance observer based fully digital controlled PWM inverter for CVCF operation," *IEEE Trans. Power Electron.*, vol. 9, no. 5, pp. 473–480, Sep. 1994.
- [72] J. S. Cho, S.-Y. Lee, H. S. Mok, and G. H. Choe, "Modified deadbeat digital controller for UPS with 3-phase PWM inverter," in *Conf. Rec. IEEE-IAS Annu. Meeting*, Phoenix, AZ, Oct. 1999, pp. 2208–2215.
- [73] O. Kükrer, "Deadbeat control of a three-phase inverter with an output LC filter," *IEEE Trans. Power Electron.*, vol. 11, no. 1, pp. 16–23, Jan. 1996.

- [74] O. Kükrer and H. Komurcugil, "Deadbeat control method for singlephase UPS inverters with compensation of computational delay," *Proc. IEE—Elect. Power Applicat.*, vol. 146, no. 1, pp. 123–128, Jan. 1999.
- [75] O.C. Montero-Hernandez and P.N. Enjeti, "Ride-through for critical loads. Exploring a low-cost approach to maintaining continuous connections between buildings and/or industrial systems," *IEEE Industry Applications Magazine*, vol.8, no.6, pp. 45- 53, Nov/Dec 2002.
- [76] M. V. Aware and D. Sutanto, "SMES for protection of distributed critical loads," *IEEE Trans. Power Delivery*, vol. 19, no. 3, pp. 1267–1275, Jul. 2004.
- [77] S.W. Mohod and M.V. Aware, "Micro Wind Power Generator With Battery Energy Storage for Critical Load," *IEEE Systems Journal* , vol.6, no.1, pp.118-125, March 2012.
- [78] Junbum Kwon, Sunjae Yoon, Hyungjin Kim and Sewan Choi, "Fault ride through control with voltage compensation capability for utility interactive inverter with critical load," *2011 IEEE 8th International Conference on Power Electronics and ECCE Asia*, 2011, pp.3041-3047.
- [79] Tai-Sik Hwang, Kwang-Seob Kim and Byung-Ki Kwon, "Control strategy of 600kW E-BOP for molten carbonate fuel cell generation system," *International Conference on Electrical Machines and Systems*, 2008, pp.2366-2371.
- [80] Kwang-Seob Kim, Chang-Jin Lim, Tai-Sik Hwang, Byung-Ki Kwon, Jae-Sik Kim, Chang-Ho Choi and Sung-Gap Choi, "A 600KW electrical balance of plant with LCL filter for molten carbonate fuel cell," *EPE '09. 13th European Conference on Power Electronics and Applications*, 2009, pp.1-7.
- [81] Tai-Sik Hwang, Hye-Seong Heo and Kwang-Seob Kim, "High performance synchronization algorithm for 600kW EBOP of fuel cell generation system," *2010 IEEE International Conference on Industrial Technology (ICIT)*, 2010, pp.1195-1200.
- [82] E.C. Aeloiza, P.N. Enjeti, L.A. Moran, O.C. Montero-Hernandez and Sangsun Kim, "Analysis and design of a new voltage sag compensator for critical loads in electrical power distribution systems," *IEEE Trans. Ind. Electron* , vol.39, no.4, pp. 1143- 1150, July-Aug. 2003.
- [83] I.J. Balaguer, Qin Lei, Shuitao Yang, U. Supatti and Fang Zheng Peng, "Control for Grid-Connected and Intentional Islanding Operations of Distributed Power Generation," *IEEE Trans. Ind. Electron*, vol.58, no.1, pp.147-157, Jan. 2011.
- [84] B. Mirafzal, M. Saghaleini and A. Kaviani, "An SVPWM-Based Switching Pattern for Stand-Alone and Grid- Connected Three-Phase Single-Stage Boost Inverters," *IEEE Trans. Power Electron*, vol.26, no.4, pp.1102-1111, April 2011.
- [85] Junbum Kwon, Sunjae Yoon and Sewan Choi, "Indirect Current Control for Seamless Transfer of Three-Phase Utility Interactive Inverters," *IEEE Trans. Power Electron*, vol.27, no.2, pp.773-781, Feb. 2012.

- [86] Zhilei Yao, Zan Wang, Lan Xiao and Yangguang Yan, "A novel control strategy for grid-interactive inverter in grid-connected and stand-alone modes," 2006. *APEC '06. Twenty-First Annual IEEE Applied Power Electronics Conference and Exposition*, 2006, pp.5 pp., 19-23.
- [87] Zilong Yang, Hua Liao, Chunsheng Wu and Honghua Xu, "Analysis and Selection of Switch for Double Modes Inverter in Micro-grid System," 2008. *ICEMS 2008. International Conference on Electrical Machines and Systems*, 2009, pp 1778-1781.
- [88] Shengli Huang, Li Kong and Haiping Xu, "Control Algorithm Research on Seamless Transfer for Distributed Resource with a LCL Filter," 2008. *DRPT 2008. Third International Conference on Electric Utility Deregulation and Restructuring and Power Technologies*, 2008, pp 2810-2814.
- [89] M.N. Arafat, S. Palle, Y. Sozer and I. Husain, "Transition Control Strategy Between Standalone and Grid-Connected Operations of Voltage-Source Inverters," *IEEE Trans. Ind. Applicat.*, vol.48, no.5, pp.1516-1525, Sept.-Oct. 2012
- [90] Guoqiao Shen, Dehong Xu and Danji Xi, "Novel seamless transfer strategies for fuel cell inverters from grid-tied mode to off-grid mode," 2005. *APEC 2005. Twentieth Annual IEEE Applied Power Electronics Conference and Exposition*, 2005, pp.109-113 Vol. 1.
- [91] Zeng Liu and Jinjun Liu, "Seamless transfer strategy with outer current loop for three phase inverter in distributed generation," 2010 *IEEE Energy Conversion Congress and Exposition (ECCE)*, 2010, pp.3556-3560.
- [92] R. Tirumala, N. Mohan and C. Henze, "Seamless Transfer of Grid-Connected PWM inverters between Utility-Interactive and Stand-Alone Modes," 2002. *APEC 2002. Seventeenth Annual IEEE Applied Power Electronics Conference and Exposition*, 2002, pp1081-1086.
- [93] Junbum Kwon, Sunjae Yoon and Sewan Choi, "Indirect Current Control for Seamless Transfer of Three-Phase Utility Interactive Inverters," *IEEE Trans. Power Electron*, vol.27, no.2, pp.773-781, Feb. 2012.
- [94] Hyosung Kim, Taesik Yu and Sewan Choi, "Indirect Current Control Algorithm for Utility Interactive Inverters in Distributed Generation Systems," *IEEE Trans. Power Electron*, vol.23, no.3, pp.1342-1347, May 2008.
- [95] Zhilei Yao, Lan Xiao and Yangguang Yan, "Seamless Transfer of Single-Phase Grid-Interactive Inverters Between Grid-Connected and Stand-Alone Modes," *IEEE Trans. Power Electron*, vol.25, no.6, pp.1597-1603, June 2010.
- [96] Xiaohuan Wang, Chunjiang Zhang, Xia Li and Zhongnan Guo, "Weighted control research on seamless transfer for dual-mode three phase inverter in micro-grid," 2011 *International Conference on Electrical Machines and Systems (ICEMS)*, 2011, pp.1-5, 20-23.

- [97] R. Teodorescu and F. Blaabjerg, "Flexible control of small wind turbines with grid failure detection operating in stand-alone and grid-connected mode," *IEEE Trans. Power Electron*, vol.19, no.5, pp. 1323- 1332, Sept. 2004.
- [98] Remus Teodorescu, Marco Liserre, Pedro Rodríguez, *Grid Converters for Photovoltaic and Wind Power Systems*, 416pp, Jan 2011.
- [99] M. H. J. Bollen, *Understanding Power Quality Problems: Voltage Sags and Interruptions*. Piscataway, NJ: IEEE Press, 2002.
- [100] L. Moran, P. D. Ziogas, and G. Joos, "Design aspects of synchronous PWM rectifier-inverter systems under unbalanced input voltage conditions," *IEEE Trans. Ind. Appl.*, vol. 28, no. 6, pp. 1286–1293, Nov./Dec. 1992.
- [101] Hong-Seok Song; Kwanghee Nam; , "Dual current control scheme for PWM converter under unbalanced input voltage conditions," *Industrial Electronics, IEEE Transactions on* , vol.46, no.5, pp.953-959, Oct 1999
- [102] Yongsug Suh; Lipo, T.A.; , "Control scheme in hybrid synchronous stationary frame for PWM AC/DC converter under generalized unbalanced operating conditions," *Industry Applications, IEEE Transactions on* , vol.42, no.3, pp. 825- 835, May-June 2006
- [103] Y. Suh and T. A. Lipo, "Modeling and analysis of instantaneous active and reactive power for PWM AC/DC converter under generalized unbalanced network," *IEEE Trans. Power Del.*, vol. 21, no. 3, pp. 1530–1540, Jul. 2006
- [104] J. G. Hwang, P. W. Lehn, and M. Winkelnkemper, "Control of grid connected AC-DC converters with minimized DC link capacitance under unbalanced grid voltage condition," in *Conf. Rec. EPE*, 2007, pp. 1–10.
- [105] Roiu, D.; Bojoi, R.I.; Limongi, L.R.; Tenconi, A.; , "New Stationary Frame Control Scheme for Three-Phase PWM Rectifiers Under Unbalanced Voltage Dips Conditions," *Industry Applications, IEEE Transactions on* , vol.46, no.1, pp.268-277, Jan.-feb. 2010
- [106] Rodriguez, P.; Timbus, A.V.; Teodorescu, R.; Liserre, M.; Blaabjerg, F.; , "Flexible Active Power Control of Distributed Power Generation Systems During Grid Faults," *Industrial Electronics, IEEE Transactions on* , vol.54, no.5, pp.2583-2592, Oct. 2007
- [107] Fei Wang; Duarte, J.L.; Hendrix, M.A.M.; , "Pliant Active and Reactive Power Control for Grid-Interactive Converters Under Unbalanced Voltage Dips," *Power Electronics, IEEE Transactions on* , vol.26, no.5, pp.1511-1521, May 2011
- [108] Lie Xu; , "Enhanced Control and Operation of DFIG-Based Wind Farms During Network Unbalance," *Energy Conversion, IEEE Transactions on* , vol.23, no.4, pp.1073-1081, Dec. 2008

- [109] Zixin Li; Yaohua Li; Ping Wang; Haibin Zhu; Congwei Liu; Wei Xu; , "Control of Three-Phase Boost-Type PWM Rectifier in Stationary Frame Under Unbalanced Input Voltage," *Power Electronics, IEEE Transactions on* , vol.25, no.10, pp.2521-2530, Oct. 2010
- [110] Qingrui Tu; Zheng Xu; Yong Chang; Li Guan; , "Suppressing DC Voltage Ripples of MMC-HVDC Under Unbalanced Grid Conditions," *Power Delivery, IEEE Transactions on* , vol.27, no.3, pp.1332-1338, July 2012
- [111] W. Choi, P. N. Enjeti, and J. W. Howze, "Development of an equivalent circuit model of a fuel cell to evaluate the effects of inverter ripple current," in *Proc. IEEE Applied Power Electronics Conf. and Expo.*, Feb. 2004, pp. 355–361.
- [112] G. Fontes, C. Turpin, R. Saisset, T. Meynard, and S. Astier, "Interactions between fuel cells and power converters influence of current harmonics on a fuel cell stack," in *Proc. IEEE Power Electronics Specialist Conf.*, Aachen, Germany, Jun. 2004, pp. 4729–47.
- [113] Robert Warren Erickson, Dragan Maksimović, *A Fundamentals of power electronics*, Kluwer Academic (2001) - Hardback - 883 pages - ISBN 0792372700
- [114] Tai-Sik Hwang; Tarca, M.J.; Sung-Yeul Park; , "Dynamic response analysis of dc-dc converter with supercapacitor for direct borohydride fuel cell power conditioning system," *Power Electronics and ECCE Asia (ICPE & ECCE), 2011 IEEE 8th International Conference on* , vol., no., pp.2304-2311, May 30 2011-June 3 2011
- [115] IEEE Standard for Interconnecting Distributed Resources with Electric Power Systems, IEEE Standard 1547, 2003.
- [116] A.A. Rockhill, M. Liserre, R. Teodorescu and P. Rodriguez, "Grid-Filter Design for a Multimegawatt Medium-Voltage Voltage-Source Inverter," *IEEE Trans. Ind. Electron*, vol.58, no.4, pp.1205-1217, April 2011
- [117] K. Jalili and S. Bernet, "Design of Filters of Active-Front-End Two-Level Voltage-Source Converters," *IEEE Trans. Ind. Electron*, vol.56, no.5, pp.1674-1689, May 2009.
- [118] J. Dannehl, F.W. Fuchs, S. Hansen and P.B. Thøgersen, "Investigation of Active Damping Approaches for PI-Based Current Control of Grid-Connected Pulse Width Modulation Converters With LCL Filters," *IEEE Trans. Ind. Applicat.*, vol.46, no.4, pp.1509-1517, July-Aug. 2010.
- [119] Xuehua Wang, Xinbo Ruan, Shangwei Liu, C.K. Tse, "Full Feedforward of Grid Voltage for Grid-Connected Inverter With LCL Filter to Suppress Current Distortion Due to Grid Voltage Harmonics," *IEEE Trans. Power Electron*, vol.25, no.12, pp.3119-3127, Dec. 2010
- [120] Kwang-Seob Kim, Byung-Ki Kwon and Chang-Ho Choi, "A novel control algorithm of a three-phase PWM inverter with output LC filter," *2007 European Conference on Power Electronics and Applications*, 2007, pp.1-6.

- [121] S. Buso, L. Malesani, and P. Mattavelli, "Comparison of current control techniques for active filters applications," *IEEE Trans. Ind. Electron.*, vol. 45, no. 5, pp. 722–729, Oct. 1998.
- [122] S. Buso, S. Fasolo, L. Malesani, and P. Mattavelli, "A dead-beat adaptive hysteresis current control," *IEEE Trans. Ind. Appl.*, vol. 36, no. 4, pp. 1174–1180, Jul./Aug. 2000.
- [123] L. Malesani, P. Mattavelli, and S. Buso, "Robust dead-beat current control for PWM rectifiers and active filters," *IEEE Trans. Ind. Appl.*, vol. 35, no. 3, pp. 613–620, May/Jun. 1999.
- [124] V. Cárdenas, N. Vázquez, C. Hernández, and S. Horta, "Analysis and design of a three phase sliding mode controller for a shunt active power filter," in *Proc. IEEE PESC'99*, Aug. 1999, vol. 1, pp. 219–223.
- [125] Xiaoming Yuan; Merk, W.; Stemmler, H.; Allmeling, J., "Stationary-frame generalized integrators for current control of active power filters with zero steady-state error for current harmonics of concern under unbalanced and distorted operating conditions," *Industry Applications, IEEE Transactions on* , vol.38, no.2, pp.523,532, Mar/Apr 2002
- [126] Gabe, I.J.; Massing, J.R.; Montagner, V.F.; Pinheiro, H.; , "Stability analysis of grid-connected voltage source inverters with LCL-filters using partial state feedback," *Power Electronics and Applications, 2007 European Conference on* , vol., no., pp.1-10, 2-5 Sept. 2007
- [127] Liserre, M.; Teodorescu, R.; Blaabjerg, F.; , "Stability of photovoltaic and wind turbine grid-connected inverters for a large set of grid impedance values," *Power Electronics, IEEE Transactions on* , vol.21, no.1, pp. 263- 272, Jan. 2006
- [128] Blasko, V.; Kaura, V.; , "A novel control to actively damp resonance in input LC filter of a three-phase voltage source converter," *Industry Applications, IEEE Transactions on* , vol.33, no.2, pp.542-550, Mar/Apr 1997
- [129] Malinowski, M.; Bernet, S.; , "A Simple Voltage Sensorless Active Damping Scheme for Three-Phase PWM Converters With an Filter," *Industrial Electronics, IEEE Transactions on* , vol.55, no.4, pp.1876-1880, April 2008
- [130] Hea-Gwang Jeong; Kyo-Beum Lee; Sewan Choi; Woojin Choi; , "Performance Improvement of LCL-Filter-Based Grid-Connected Inverters Using PQR Power Transformation," *Power Electronics, IEEE Transactions on* , vol.25, no.5, pp.1320-1330, May 2010
- [131] Dick, C.P.; Richter, S.; Rosekeit, M.; Rolink, J.; De Doncker, R.W.; , "Active damping of LCL resonance with minimum sensor effort by means of a digital infinite impulse response filter," *Power Electronics and Applications, 2007 European Conference on* , vol., no., pp.1-8, 2-5 Sept. 2007
- [132] Gullvik, W.; Norum, L.; Nilsen, R.; , "Active damping of resonance oscillations in LCL-filters based on virtual flux and virtual resistor," *Power Electronics and Applications, 2007 European Conference on* , vol., no., pp.1-10, 2-5 Sept. 2007

- [133] Papavasiliou, A.; Papathanassiou, S.A.; Manias, S.N.; Demetriadis, G.; , "Current Control of a Voltage Source Inverter Connected to the Grid via LCL Filter," *Power Electronics Specialists Conference*, 2007. PESC 2007. IEEE , vol., no., pp.2379-2384, 17-21 June 2007
- [134] Liserre, M.; Dell'Aquila, A.; Blaabjerg, F.; , "Genetic algorithm-based design of the active damping for an LCL-filter three-phase active rectifier," *Power Electronics, IEEE Transactions on* , vol.19, no.1, pp. 76- 86, Jan. 2004
- [135] Calculus: Early Transcendental Functions– January 1, 2014 by Ron Larson, Bruce H. Edwards
- [136] Tai-Sik Hwang; Sung-Yeul Park; "Seamless Boost Converter Control Under the Critical Boundary Condition for a Fuel Cell Power Conditioning System," *IEEE Transactions on Power Electronics*, vol.27, no.8, pp.3616-3626, Aug. 2012
- [137] Tai-Sik Hwang; Sung-Yeul Park; , "Seamless boost converter control in critical boundary condition for fuel cell power conditioning system," *Energy Conversion Congress and Exposition (ECCE)*, 2011 IEEE , vol., no., pp.3641-3648, 17-22 Sept. 2011
- [138] Tai-Sik Hwang; Sung-Yeul Park, "A Seamless Control Strategy of a Distributed Generation Inverter for the Critical Load Safety Under Strict Grid Disturbances," *Power Electronics, IEEE Transactions on* , vol.28, no.10, pp.4780,4790, Oct. 2013
- [139] Tai-Sik Hwang; Sung-Yeul Park; , "A seamless control strategy of distributed generation inverter for critical load safety under strict grid disturbance," *Applied Power Electronics Conference and Exposition (APEC)*, 2012 Twenty-Seventh Annual IEEE , pp.254-261, 5-9 Feb. 2012
- [140] Tai-Sik Hwang; Sung-Yeul Park; "DC Power Ripple Minimization of LCL filter based Distributed Generation Inverter under Unbalanced Voltage Conditions," *Applied Power Electronics Conference and Exposition (APEC)*, 2013